SEARCH FOR HEAVY RESONANCES
DECAYING INTO $t\bar{t}$ PAIRS

By

VALENTIN NECULA

A DISSERTATION PRESENTED TO THE GRADUATE SCHOOL
OF THE UNIVERSITY OF FLORIDA IN PARTIAL FULFILLMENT
OF THE REQUIREMENTS FOR THE DEGREE OF
DOCTOR OF PHILOSOPHY

UNIVERSITY OF FLORIDA

2006

I dedicate this work to my parents, Maria-Doina and Eugen Necula.

company of Gheorghe Lungu and Dr. Gavril A. Giurgiu were very useful as well and I would like to thank them both.

TABLE OF CONTENTS

xi

Abstract of Dissertation Presented to the Graduate School
of the University of Florida in Partial Fulfillment of the
Requirements for the Degree of Doctor of Philosophy

SEARCH FOR HEAVY RESONANCES
DECAYING INTO $t\bar{t}$ PAIRS

By

Valentin Necula

August 2006

Chair: Guenakh Mitselmakher
Cochair: Jacobo Konigsberg
Major Department: Physics

We performed a search for narrow-width vector particles decaying into top-antitop pairs using 680 pb^{-1} of data collected by the CDF experiment during 2002-2005 Run 2 of the Tevatron. The center of mass energy of the $p\bar{p}$ collisions was 1.96 TeV. Model independent upper limits on the production cross-section times branching ratio are derived, at 95% confidence level. We exclude the existence of a leptophobic Z' boson in a topcolor-assisted technicolor model with a mass $M_{Z'} < 725 GeV/c^2$, and our results can be used to constrain any other relevant theoretical model.

CHAPTER 1
INTRODUCTION

1.1 Historical Perspective

The science of Physics investigates the laws governing the behavior of matter, from the smallest subnuclear scales to the largest astronomical space-time regions and even the nature of the universe as a whole, as in cosmology.

In High Energy Physics we are concerned with understanding the so-called fundamental "bricks" of matter or elementary particles and their interactions. It is not easy to ascertain elementariness, in fact it is quite impossible, and history shows us that more often than not what was considered elementary at one point was found later to be a composed system: molecules, which are the smallest units of substance possessing specific physical and *chemical* properties, were found to be made up of smaller units, atoms. A huge variety of organic matter with quite different physicochemical properties is composed of just three atoms, hydrogen, carbon and oxygen. For some time atoms were considered to live up to their ancient meaning of indivisible units of matter, until the end of the 19th century when the mysterious cathode rays puzzled physicists with their properties. As J.J. Thomson correctly predicted, the cathode rays were actually streams of *subatomic* particles known today as electrons. It wasn't long until Rutherford proved in his famous scattering experiments that the positive charge inside atoms is confined to a pointlike core, or nucleus, a discovery which led to the classic planetary model of the atom. The elementariness of the atom vanished, and the focus moved to the structure of the nucleus. At first it was thought that the nucleus contained electrons and protons, but eventually the neutron (postulated by Rutherford) was discovered and the picture of matter had been simplified even more: just three

particles, the proton, the neutron and the electron, were enough to build all known atoms. They were the new elementary particles, however soon they were joined by a large number of new particles with strange names like pions, kaons, eta and rho particles. The simple and maybe beautiful picture of three elementary particles at the basis of all matter had to be abandoned. Both experimental and theoretical breakthroughs lead to the understanding that protons, neutrons and the vast majority other particles are composed of smaller and stranger units, called quarks.

Two different developments took place during this time though. First, one of the most brilliant physicists of all times, P.A.M. Dirac, predicted in 1928, solely on theoretical grounds, the existence of a new particle which was later called the positron. It was supposed to be just like the electron, but positively charged, an *antielectron*. Amazingly, positrons were in fact observed only four years later and then it was found that other particles had antiparticles. It was an universal phenomenon.

Secondly, searching for a particle postulated in the Yukawa theory of nuclear forces, experimentalists found something else, as it is often the case: a new negatively charged particle which behaved just like an elecron except it had much higher mass and it was unstable. It was called a muon. This phenomenon was found to have its own kind of universality and lead to the classification of elementary particles in three generations, as it will be detailed later.

Particle physics also investigates the interactions or forces between the elementary constituents of matter. By mid 20th century physicists counted four distinct forces: the gravitational force, the electromagnetic force, the strong nuclear force responsible for holding quarks together inside a proton or neutron for instance, and the weak nuclear force responsible for β decays and other phenomena. The early picture of classical "force" fields mediating the interactions was abandoned after Dirac quantized the Maxwell's equations successfully, laying

the foundation for quantum field theory and introducing the idea that interactions are mediated by exchanges of virtual particles. Later it was discovered that indeed the strong and weak nuclear forces *are* mediated by virtual particles, the gluon and the massive W^+, W^- and Z bosons respectively. However, even though we have a classical set of equations describing gravitation and powerful formalisms for quantizing fields, all attempts at quantum gravity failed. Delving into that mystery is not the purpose of this dissertation though, and now we will proceed to a more formal presentation of the theoretical framework underlying our current understanding of elementary particles and their interactions.

<p align="center">1.2   The Standard Model of Elementary Particles</p>

The Standard Model is a quantum field theory which is based on the gauge symmetry $SU(3)_C \times SU(2)_L \times U(1)_Y$ [1]. This gauge group includes the symmetry group of the strong interaction, $SU(3)_C$ and the symmetry group of the unified electroweak interaction, $SU(2)_L \times U(1)_Y$. As pointed out earlier, gravitation didn't fit the scheme and it is not part of the Standard Model.

All the variety of phenomena is the result of the interactions of a small number of elementary particles, classified as leptons, quarks and force carriers or mediators. They are also classified in three generations with similar properties.

1.2.1   Leptons

All leptons and hadrons have spin 1/2, and all force mediators have spin 1. There are three six charged leptons, the electron (e^-), the muon (μ^-), the tauon (τ^-) and their positively charged antiparticles. For each charged lepton there corresponds a neutral lepton, called a neutrino (ν). Even though neutrinos do not carry electric charge, they have distinct antiparticles due to the fact that they possess a property called lepton number. There are three lepton numbers, the electronic lepton number, the muonic lepton number and the tauonic lepton number. An electron carries a +1 electronic lepton number and an electronic

neutrino (ν_e) also carries a +1 electronic lepton number. Similarly a muon and a muon neutrino (ν_μ) carry a +1 muonic lepton number, a tauon and a tau neutrino (ν_τ) carry a +1 tauonic lepton number. The antiparticles of these particles carry -1 leptonic numbers and in the Standard Model each lepton number is conserved such that in any reaction the total lepton numbers of the initial state particles should be equal to the total lepton numbers of the final state particles. It should be noted that significant evidence has been gathered during the last decade indicating that neutrinos oscillate, thus violating the leptonic number conservation.

Table 1–1: Properties of leptons. Antiparticles are not listed.

	Particle	Spin	Charge	Mass
1st generation	e^-	1/2	-1	0.51099892 ± 0.00000004 MeV/c^2
	ν_e	1/2	0	< 3 eV/c^2
2nd generation	μ^-	1/2	-1	105.658369 ± 0.000009 MeV/c^2
	ν_μ	1/2	0	< 0.19 MeV/c^2
3rd generation	τ^-	1/2	-1	$1776.99^{+0.29}_{-0.26}$ MeV/c^2
	ν_τ	1/2	0	< 18.2 MeV/c^2

The interactions of leptons are described by the electroweak theory which unifies electromagnetism and the weak force. In this gauge theory there are three massive force carriers, the W^+, W^- and Z bosons and one massless force carrier, the photon(γ). In fact a pure gauge theory of leptons and gauge bosons would lead to massless particles, so in order for the particles to "acquire" mass the spontaneous symmetry breaking mechanism was proposed. This adds an extra spin 0 boson to the picture, the Higgs boson, by which all gauge bosons except one (γ) acquire mass, and leptons can acquire mass simply by coupling to the scalar Higgs field. Even though the massive bosons [2, 3, 4, 5] have been discovered at CERN more than 20 years ago, the Higgs boson has not been discovered. It is also possible that the mass problem is solved by some other mechanism.

<u>1.2.2   Quarks</u>

There are six types of quarks and their antiparticles, commonly referred to as the up (u), down (d), strange (s), charm (c), bottom(b) and top(t) quarks. They carry fractional electrical charges and a new property called color, which is responsible for the strong interactions of quarks. Each quark can carry one of three colors, red, blue and green. The antiquarks carry anticolors, antired, antiblue and antigreen. Quarks' properties are summarized in Table 1–2.

Quarks also take part in electroweak processes and that led to some remarkable predictions. It was found that in order to be able to renormalize the electroweak theory an equal number of generations of quarks and leptons was needed, but when these ideas appeared only three quarks were known, the u, d and s. Few years later in 1974 the c quark was discovered, thus completing the second quark generation as expected. Another three years later a third generation charged lepton was discovered, τ, and in the same year a third generation quark was discovered, the b. The interesting part is that the massive bosons themselves were not discovered until 1983 ! The quest for the last missing pieces in the generation picture ended with the top quark discovery in 1994 at Fermilab and the ν_τ discovery in 2000, also at Fermilab.

Table 1–2: Properties of quarks. Additionally, each quark can also carry one of three color charges.

	Particle	Spin	Charge	Mass
1st generation	u	1/2	+2/3	1.5-4 MeV/c^2
	d	1/2	-1/3	4-8 MeV/c^2
2nd generation	c	1/2	+2/3	1.15-1.35 GeV/c^2
	s	1/2	-1/3	80-130 MeV/c^2
3rd generation	t	1/2	+2/3	178.0±4.3 GeV/c^2
	b	1/2	-1/3	4.1-4.4 GeV/c^2

The strong interactions of quarks are mediated by eight massless gluons (g) which carry double color charge, thus being able to interact among themselves. The

theory of strong interactions is known as Quantum Chromodynamics (QCD) and it is a gauge theory based on the SU(3) Lie group. It has two characteristics not found in the electroweak theory, called color confinement and asymptotic freedom. The interaction between colored particles is found to increase in strength with the distance between them, therefore quarks do not appear as free particles. Instead they form color singlet states either by combining three quarks with different colors (barions) or combining a quark and an antiquark (mesons). This is "color confinement". Conversely, at smaller and smaller distances the interaction strength decreases and the coupling constant α_s becomes small enough for perturbative methods to work. This feature is known as "asymptotic freedom."

1.3   Beyond the Standard Model

The Standard Model has managed to explain very well a vast amount of experimental data, however there are reasons to believe it is an incomplete theory :

- As mentioned earlier, gravity is left out altogether
- Possibly connected to the previous point, the observed masses of particles are completely unexplained. The Higgs mechanism is just a way by which particles would "acquire" mass, both bosons and fermions, but it does not predict their values.
- The gauge anomaly of the electroweak theory is canceled only if we have an equal number of quark and lepton generations, and the charges of the particles within one generation obey a certain constraint equation. This implies that there is some deeper connection between quark and leptons which might also explain why we have only three generations.
- Besides particles' masses, there are still quite many arbitrary parameters in the Standard Model, like the relative strengths of the interactions, the Weinberg angle $\sin\theta_W$, the elements of the Cabibbo-Kobayashi-Maskawa

matrix which desctibe the strength of cross-generation direct coupling of quarks via charged currents.

- There are significant indications that neutrinos oscillate.

- The amount of known matter in the Universe is less than what would be necessary to produce a flat geometry as observed, and it is believed that there must exist other types of matter, dark matter, besides a non-zero cosmological constant or dark energy, which would explain the discrepancy. But these conclusions rely on the validity of General Relativity in describing the Universe as a whole, which is not quite obvious.

Many theories beyond the Standard Model have been proposed, like Supersymmetry, String theories, Grand Unified Theories (GUTs), extra dimensions theories, Technicolor, quark compositeness theories and others. Some are basically impossible to test at current available energies, but most have a large parameter space and it is difficult to rule them out completely. In this work we decided to adopt a model independent approach to our search for Physics beyond the Standard Model, at least as much as it is possible.

CHAPTER 2
NEW PHYSICS AND THE TOP QUARK

The top quark is so much heavier than the other quarks, including its 3rd generation sibling the b quark, that it is natural to ask whether this fact is related to its possible coupling to New Physics. This idea was explored in a theory called "topcolor-assisted technicolor" [6, 7] which introduces new strong dynamics coupling preferentially to the third generation, thus making the $t\bar{t}$ and $b\bar{b}$ final states of particular interest. This theory introduces a topcolor heavy Z' and "topgluons", both decaying into $t\bar{t}$ and $b\bar{b}$ pairs.

There are other theoretical avenues for producing heavy resonances, like Universal Extra Dimension models [8, 9, 10]. The simpler versions [8, 9] assume only one extra dimension of size R, and lead to new particles via the Kaluza-Klein(KK) mechanism. In the minimal UED model [9] only one more parameter is needed in the theory, the cutoff scaleΛ. An interesting feature is the conservation of the KK number at tree level, and in general the conservation of the KK parity defined as $(-1)^n$ where n is the KK number. As a consequence the lightest KK partner at level 1 has negative KK parity and it is stable, therefore possible candidates for our search are level 2 KK partners. These can couple to Standard Model particles only through loop diagrams, given the need to conserve KK parity.

Another UED model [10] assumes that all known particles propagate in two small extra dimensions, also leading to new states viathe Kaluza-Klein mechanism. Resonance states below $1\ TeV$ are predicted in this model, and they have significant couplings to $t\bar{t}$ pairs.

From a purely experimental point of view the $t\bar{t}$ production mechanism is an interesting process in which to search for New Physics since the full compatibility

of $t\bar{t}$ candidate events with the Standard Model is not known with great precision due to quite limited statistics. There is room to explore for possible non-Standard Model sources within such an event sample.

In this dissertation we focus on the search for a heavy resonance produced in $p\bar{p}$ collisions at $\sqrt{s} = 1.96\ TeV$ which decays into $t\bar{t}$ pairs. The basic idea is to compute the $t\bar{t}$ invariant mass spectrum and search for indications of unexpected resonance peaks. We will implement the tools needed to set lower and upper limits for the resonance production cross-section times branching ratio at any given confidence level. A discovery would amount to a non-zero lower limit at a significant confidence level.

A similar search was carried out at the Tevatron by the CDF [11] and D0 [12] collaborations on the data gathered in "Run 1", the period of operation between 1992-1995.

The $t\bar{t}$ invariant mass as reconstructed by the CDF analysis in the "lepton plus jets" channel is shown in Figure 2–1. There are *only* 63 events for the entire Run 1 dataset, which corresponds to an integrated luminosity of 110 pb^{-1}. About half of them were $t\bar{t}$ events.

Based on this distribution the 95% confidence level upper limits on $t\bar{t}$ resonant production cross-section times branching ratio were computed, as a function of resonance mass (Figure 2–2).

The main challenge of this analysis is the reconstruction of the $t\bar{t}$ invariant mass spectrum. In this analysis we use an innovative approach which includes matrix element information to help with the reconstruction, as it will be explained in later chapters.
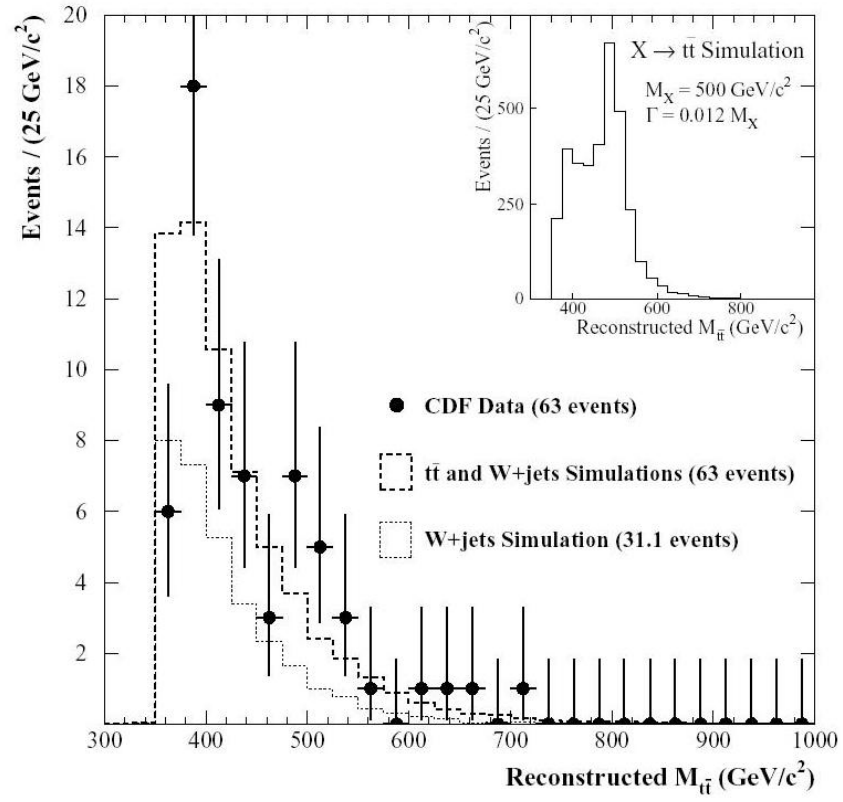
Figure 2–1: The CDF Run 1 $t\bar{t}$ invariant mass spectrum.
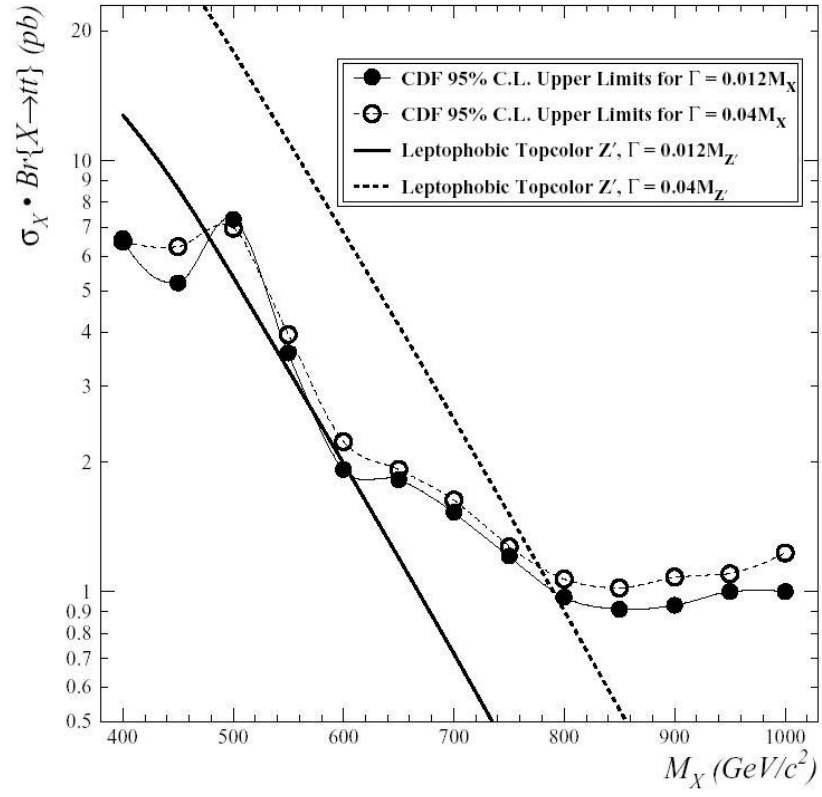
Figure 2–2: The CDF Run 1 upper limits for resonance production cross-section times branching ratio.

CHAPTER 3
EXPERIMENTAL APPARATUS

The Fermi National Accelerator Laboratory (FNAL, Fermilab) has been
a leading facility in experimental particle physics for the last 30 years. The
hadron collider, called the Tevatron, is the world's most powerful accelerator
where proton-antiproton collisions are investigated. While many measurements
and searches have been carried out, probably the most famous results out of the
Tevatron program are the discovery of the bottom quark in 1977 and the discovery
of the top quark in 1994, during the 1992-1995 Tevatron operation period known as
"Run 1".

At the moment of this writing we are in the middle of Run 2, the second
Tevatron operation period which started in the spring of 2001. Record instantaneous
luminosities ($\sim 1.7 \cdot 10^{32}$ $cm^{-2}s^{-1}$) have been achieved recently, which makes the
search for new particles including the last missing block of the Standard Model, the
Higgs boson, a lot more interesting.

The Collider Detector at Fermilab (CDF) and D0 are two general purpose
detectors built at almost opposite collision points along the accelerator. In
this analysis we use data collected by the CDF collaboration during the period
2002-2005. The center of mass energy in Run 2 is $\sqrt{s} = 1.96$ TeV, the highest
collision energy ever achieved.

3.1   Tevatron Overview

The Fermilab accelerator complex is shown on a schematic drawing in Fig.
3–1. In order to produce such high energy $p\bar{p}$ collisions a sequence of five individual
accelerators is needed.
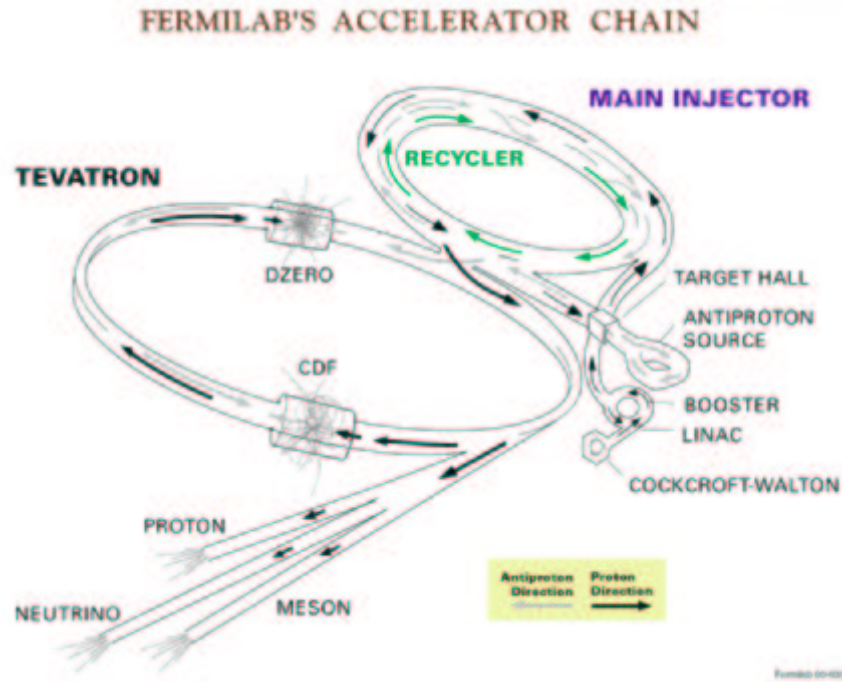
Figure 3–1: Overview of the Fermilab accelerator complex. The $p\bar{p}$ collisions at the center-of-mass energy of 1.96 TeV are produced by a sequence of five individual accelerators: the Cockroft-Walton, Linac, Booster, Main Injector, and Tevatron.

First, the Cockroft-Walton accelerator boosts negative hydrogen ions to 750 KeV energy. Then, the ions are directed to the second stage of the process provided by the 145 m long linear accelerator (Linac) which further increases the energy of ions up to about 400 MeV.

Before the next stage the ions are stripped of their electrons when they pass through a carbon foil, leaving a pure proton beam. These protons move to the next stage, the Booster, which is a synchrotron accelerator of about 150 m in diameter. At the end of this stage the protons reach an energy of 8 GeV. Next, protons are injected into another circular accelerator called the Main Injector. The Main Injector serves two functions. It provides a source of 120 GeV protons needed to produce anti-protons. It also boosts protons and anti-protons from 8 GeV up to 150 GeV before injecting them into the Tevatron.

In order to produce anti-protons, 120 GeV protons are transported from the Main Injector to a nickel target. From the interaction sprays of secondary particles are produced, including anti-protons. Those anti-protons are selected and stored into the Debuncher ring where they are stochastically cooled to reduce the momentum spread. At the end of this process, the anti-protons are stored in the Accumulator, until they are needed in the Tevatron.

The Tevatron is a proton-antiproton synchrotron collider situated in a 1 km radius tunnel. It accelerates 150 GeV protons and anti-protons up to 980 GeV, leading to a $p\bar{p}$ collision center-of-mass energy of 1.96 TeV.

Inside the Tevatron the beams are split into 36 "bunches" which are organized in three groups of 12. Within each group the bunches are separated in time by 396 ns. Collisions take place bunch by bunch, when a proton bunch meets an antiproton bunch at the interaction point. Just for clarity we should add that the beams are *injected* bunch by bunch.

The collisions do not take place at the exact same location each time but are spread in space, according to a Gaussian distribution with a sigma of about 28 cm along the beam direction and also extending in the transverse plane with a circular cross-section defined by a radius of about 25 μm

The instantaneous luminosity of the Tevatron is given by

$$\mathcal{L}_{inst} = \frac{N_p N_{\bar{p}} f}{\mathcal{A}} \tag{3-1}$$

where N_p and $N_{\bar{p}}$ are the numbers of protons and anti-protons per bunch, f is the frequency of bunch crossings and $\mathcal{A}$ is the effective area of the crossing beams.

A compact period of time during which collisions take place in the Tevatron is called a "store" and it can last from few hours to over 24 hours. During a store the instantaneous luminosity is decreasing exponentially due to collisions and transverse spreading of the beams which leads to losses of protons and anti-protons.

The instantaneous luminosity can drop one order of magnitude during one store. Run 2 initial instantaneous luminosity ranged from about $5 \cdot 10^{30}$ $cm^{-2}s^{-1}$ in 2002 to the record $1.7 \cdot 10^{32}$ $cm^{-2}s^{-1}$ in 2006 and there are hopes for even higher values in the future.

3.2   CDF Overview and Design

The Collider Detector at Fermilab (CDF) is a general purpose detector located at one of the two beam collision points along the Tevatron known as "B0".

The idea of a general purpose detector is to allow the study of a wide range of processes occurring in $p\bar{p}$ collisions. For that purpose CDF is designed such that it can identify electrons, muons, photons and jets. It is indirectly sensitive to particles which escape detection, like the neutrinos.

A schematic drawing of the CDF detector is shown in Fig. 3–2. It is cylindrically symmetric about the beam direction with a radius of about 5 m and a length of 27 m from end to end, and weighs over 5000 metric tons. The CDF collaboration uses a right-handed Cartesian coordinate system with its origin in the center of the detector, the positive z-axis along the proton beam direction, the positive x-axis towards the center of the Tevatron ring and the positive y-axis pointing upward. The azimuthal angle ϕ is defined counterclockwise around the beam axis starting from the positive x-axis. The polar angle θ is defined with respect to the positive z-axis. However, another quantity is widely used instead of the polar angle. It is called pseudo-rapidity and it is defined by the formula $\eta = -\ln(\tan(\theta/2))$. The reason is that in the massless approximation, which is a very good one at these energies, relativistic boosts along the z-axis are additive in the pseudo-rapidity variable and this property is important, for instance in the consistent definition of jet cones.

The pseudo-rapidity can also be defined with respect to the actual position of the interaction vertex, in which case it is called event pseudo-rapidity.
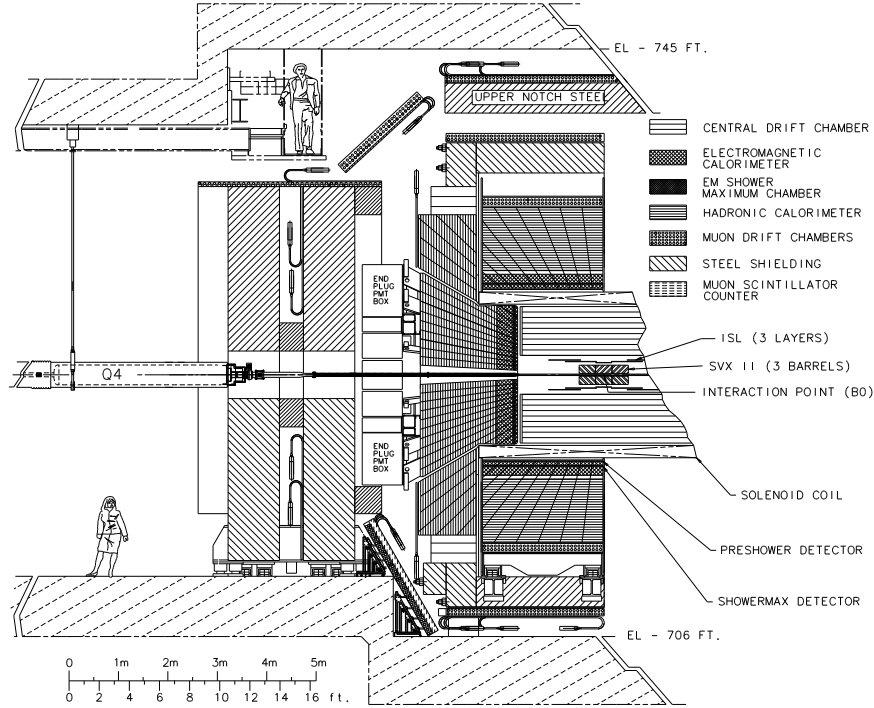
Figure 3–2: Drawing of the CDF detector. One quarter view.

The detector is composed by a series of subdetectors. Closest to the beam is the silicon vertex detectors which are surrounded by charged particle tracking chambers. The silicon vertex detectors are used to reconstruct the position of the collision vertex and particle momenta. Next are the electromagnetic and hadronic calorimeters used for energy measurements and at last the muon chambers. There is also a time-of-flight system used for charged hadrons identification and the Cherenkov Luminosity Counters (CLC) which measure luminosity.

For this analysis we use all major parts of the detector. The calorimetry is necessary for jet reconstruction, energy measurements for electrons, muon identification and also for the calculation of missing transverse energy. The tracking system plays a major role in electron and muon identification and in momentum measurement, and the muon chambers are important for muon identification.

In this section we will provide a general description of the major components of the detector, mainly emphasizing the parts used for this analysis. A more comprehensive description can be found in the published literature [13]

3.2.1   Calorimetry

The purpose of the calorimeters is to measure the energy depositions of particles passing through them. However not all particles interact in the same way. Neutrinos escape without any interaction at all, and high energy muons also escape the calorimeters without losing much energy. Apart from that, the rest of the particles leave their entire energy in the calorimeter with some exceptions in the case on pions for instance which can travel, rarely, beyond the calorimeter.

Even though neutrinos do not interact with the calorimeter, by applying the conservation of momentum in the transverse plane one can calculate the total transverse momentum of the neutrinos. Since the calorimeter measures energy this inferred quantity is known as missing transverse *energy*. In case the event contained high energy muons it needs further corrections before it can be identified as neutrino transverse momentum since, as mentioned before, the muons also do not leave much energy in the calorimeter.

The electromagnetic calorimeter is designed such that it can measure well the energy of photons and electrons (positrons). Electrons above 100 MeV lose their energy mostly through bremsstrahlung or photon radiation. High energy photons produce electron-positron pairs in the nuclear electromagnetic fields of the material, thus restarting the cycle and leading to the development of an electromagnetic shower of electrons, positrons and photons. At the last stage, low energy photons unable to create electron-positron pairs lose their energy by Compton scattering and photoelectric processes, while low energy electrons lose their energy by ionization.

For simplicity we will assume that the initial particle moves perpendicular to the detector. Then as the shower develops in the calorimeter more and more energy is deposited, but at different depths or in different layers of the detector. However at some point the number of new shower particles starts to decrease and then later no new particles will be created. After this point the energy deposited per layer starts to decrease, exponentially. The depth of the maximum energy deposition layer is called the shower maximum and can be used for particle identification.

Other charged particles like muons behave differently because the energy loss via radiation starts to dominate energy loss via ionization at much higher energies, higher by a factor of $(m/m_e)^2$, approximately. Given the energy scale at the Tevatron, a typical muon leaves roughly 10% of its energy in the electromagnetic calorimeter and thus it is not possible to identify and measure muon momenta using the calorimeter.

Table 3–1: Summary of CDF calorimeters. X_0 and λ_0 refer to the radiation length for the electromagnetic calorimeter and interaction length for the hadronic calorimeter, respectively. Energy resolutions correspond to a single incident particle.

Calorimeter subsystem	η coverage	Depth	Energy resolution $\sigma(E)/E$
CEM	$|\eta| < 1.1$	18 X_0	$13.5\%/\sqrt{E_T} \; \oplus \; 2\%$
PEM	$1.1 < |\eta| < 3.6$	21 X_0	$16\%/\sqrt{E_T} \; \oplus \; 1\%$
CHA	$|\eta| < 0.9$	4.5 λ_0	$75\%/\sqrt{E_T} \; \oplus \; 3\%$
WHA	$0.7 < |\eta| < 1.3$	4.5 λ_0	$75\%/\sqrt{E_T} \; \oplus \; 3\%$
PHA	$1.2 < |\eta| < 3.6$	7 λ_0	$80\%/\sqrt{E_T} \; \oplus \; 5\%$

The hadronic calorimeter functions on similar principles, it is designed to interact strongly with hadrons, thus making it possible to measure their energy by measuring the deposited energy. In this case the incoming particle interacts with the nuclei of the material in the detector leading to a similar shower development.

The CDF calorimeter system covers the full azimuthal range and extends up to 5.2 in $|\eta|$. Its components are the Central Electromagnetic Calorimeter (CEM) and the Central Hadronic Calorimeter (CHA) which cover the central region as

the name suggests; the Plug Electromagnetic Calorimeter (PEM) and the Plug Hadronic Calorimeter (PHA), which extend the $|\eta|$ coverage more; the Endwall Hadronic Calorimeter (WHA), which is located in between the central and plug regions; and finally the Miniplug (MNP), which is a forward electromagnetic calorimeter which is not used in this analysis. Some technical details are listed in Table 3–1.

Each calorimeter subsystem is divided in smaller units called towers and has a projective geometry, which means that all towers point to the center of the detector.

Central Calorimeter. Each tower of the central calorimeters covers $15°$ in $\Delta\phi$ and 0.11 in $\Delta\eta$ and it is composed of alternating layers of absorber and active material. When a particle passes through the dense absorber material it produces a shower of secondary particles which interact with the active material and produce light. The light is collected and converted in a measurement of energy deposition.

The CEM is made of 0.5 cm thick polystyrene scintillator active layers which are separated by 0.32 cm thick lead absorber layers.

The CEM extends from the radius of 173 cm up to 208 cm from the beam line and the total thickness of the CEM material is about 18 radiation lengths. It is divided into two identical pieces at $\eta = 0$ and both have an one inch thick iron plate at $\eta = 0$. This kind of uninstrumented region is commonly referred to as a "crack".

An important parameter is the energy resolution. The CEM resolution for electrons or photons between 10 and 100 GeV is given by

$$\frac{\sigma(E)}{E} = \frac{13.5\%}{\sqrt{E_T}} \oplus 2\% \ \ (CEM), \tag{3-2}$$

where E_T (in GeV) is the transverse energy of the electron or photon and the symbol $\oplus$ indicates that two independent terms are added in quadrature.

Inside the CEM, at a depth of about six radiation lengths or 184 cm away from the beam line, there is the Central Electromagnetic Shower Maximum detector (CES). Its position corresponds to the location of the maximum development of the electromagnetic shower which was described earlier. The CES determines the shower position and its transverse development using a set of orthogonal strips and wires. Cathode strips are aligned in the azimuthal direction providing z-view information and anode wires are arranged along the z direction providing the $r - \phi$ view information. The position measurement using this detector has a resolution of 0.2 cm for 50 GeV electrons.

The CHA is located right after the CEM and its pseudorapidity coverage is $|\eta| < 0.9$ while WHA calorimeter extends this coverage up to $|\eta| < 1.3$. It has a depth of about 4.5 interaction lengths and consists of 1 cm thick acrylic scintillator layers interleaved with steel layers 2.5 cm thick. The end wall calorimeter uses 5 cm thick absorber layers.

The electromagnetic and hadronic calorimeters were calibrated using electron and respectively pion test beams of 50 GeV. Their performance is described by the energy resolution. For charged pions between 10 and 150 GeV it is given by

$$\frac{\sigma(E)}{E} = \frac{75\%}{\sqrt{E_T}} \oplus 3\% \quad (CHA, WHA), \tag{3-3}$$

Plug Calorimeter. The PEM and PHA calorimeters cover an $|\eta|$ range between 1.1 and 3.6 and employ the same principles.The PEM is a lead/scintillator calorimeter with 0.4 cm thick active layers and 0.45 cm thick lead layers. It also includes a shower maximum detector at a depth of about 6 radiation lengths, the PES, but it is not used in this analysis. The PHA contains 0.6 cm thick scintillator layers and 5 cm think iron layers. An $r - z$ cross section view of the
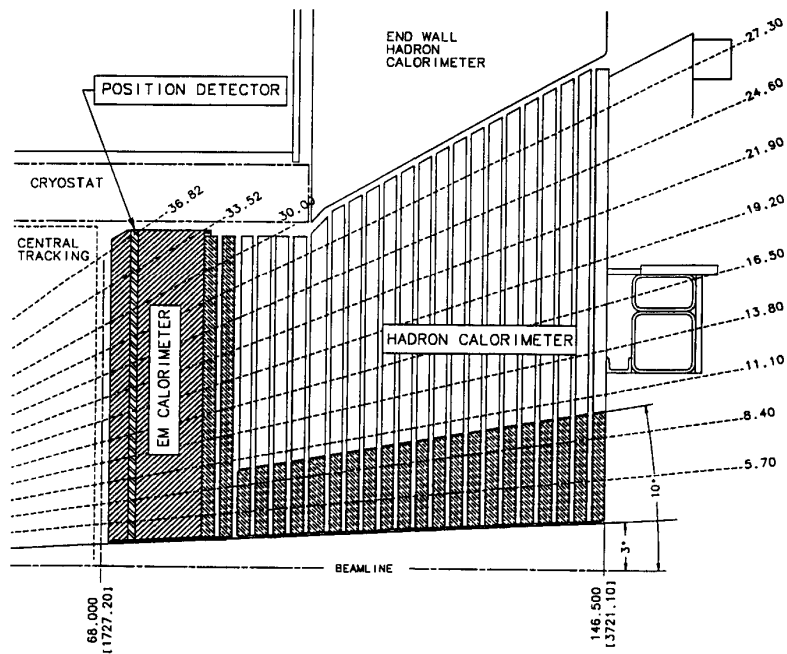
Figure 3–3: The $r - z$ view of the new Run II end plug calorimeter

CDF plug calorimeters is shown in 3–3. In this analysis the calorimeters were used to determine the momentum and direction of electrons and jets.

3.2.2   Tracking System

The purpose of the tracking system is to reconstruct trajectories and momenta of charged particles and find the location of the primary and secondary vertices. A primary vertex is the location where a $p\bar{p}$ interaction occurred. A secondary vertex is the location where a decay took place. For instance charm and bottom hadrons have a longer lifetime than light quarks hadrons, long enough that they can travel and decay at a location experimentally discernible from the primary vertex location. Such distances are of the order of hundreds of microns and this feature is exploited in heavy flavor tagging algorithms.

The components of the tracking system are the following: superconducting solenoid, silicon detectors and a large open-cell drift chamber known as Central Outer Tracker (COT). A diagram is shown in Figure 3–4. As it can be seen, the

CDF Tracking Volume
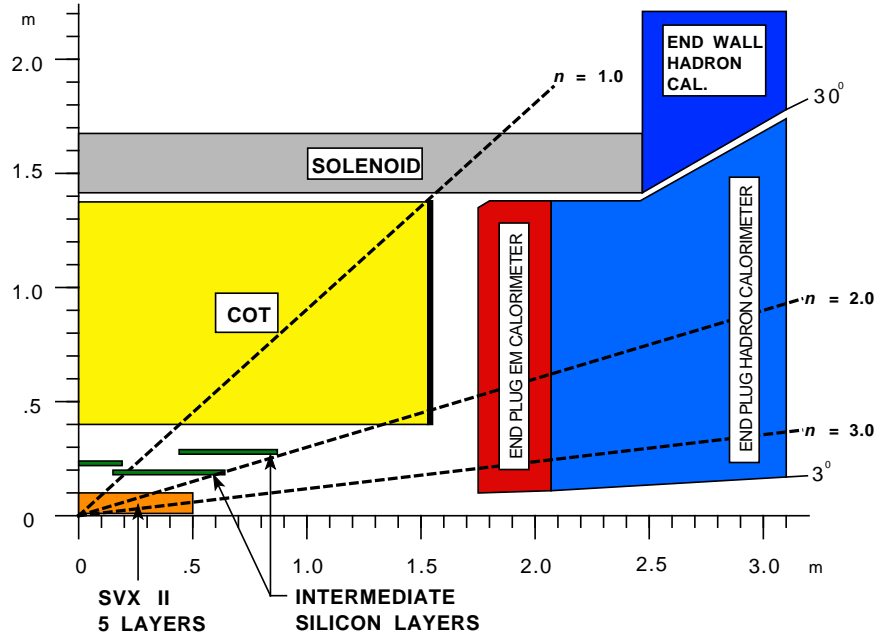
Figure 3–4: Longitudinal view of the CDF II Tracking System.

COT isn't very useful for $|\eta| > 1$ so CDF can rely only on the silicon detectors for that region. But for the $|\eta| < 1$ range both silicon and COT information is used and a full 3D track reconstruction is possible.

The Solenoid. This is a superconducting magnet which produces a $1.4\ T$ uniform magnetic field oriented along the z-axis. It is $5\ m$ long and $3\ m$ in diameter and it allows for the determination of the momentum and sign of charged particles.

Silicon Detectors. It is composed of three separate parts: Layer 00 (L00), the Silicon Vertex Detector (SVX) and the Intermediate Silicon Layers (ISL).

Layer 00. This is the innermost part of the silicon detectors and is made up by a single layer of radiation hard silicon attached to the beam pipe [14]. Its purpose is to improve the impact parameter resolution for low momentum particles which suffer multiple scattering in the materials and readout electronics found prior to other tracking system components. Also it can help extend the lifetime of the

tracking system in general, given that the inner layers of the SVX will degrade due to radiation damage.

Silicon Vertex Detector. The SVX is segmented into three barrels along the z-axis and has a total length of 96 cm. Each barrel is divided into 12 wedges in ϕ, which contain five layers of silicon microstrip detectors. All layers are double-sided (Figure 3–5).
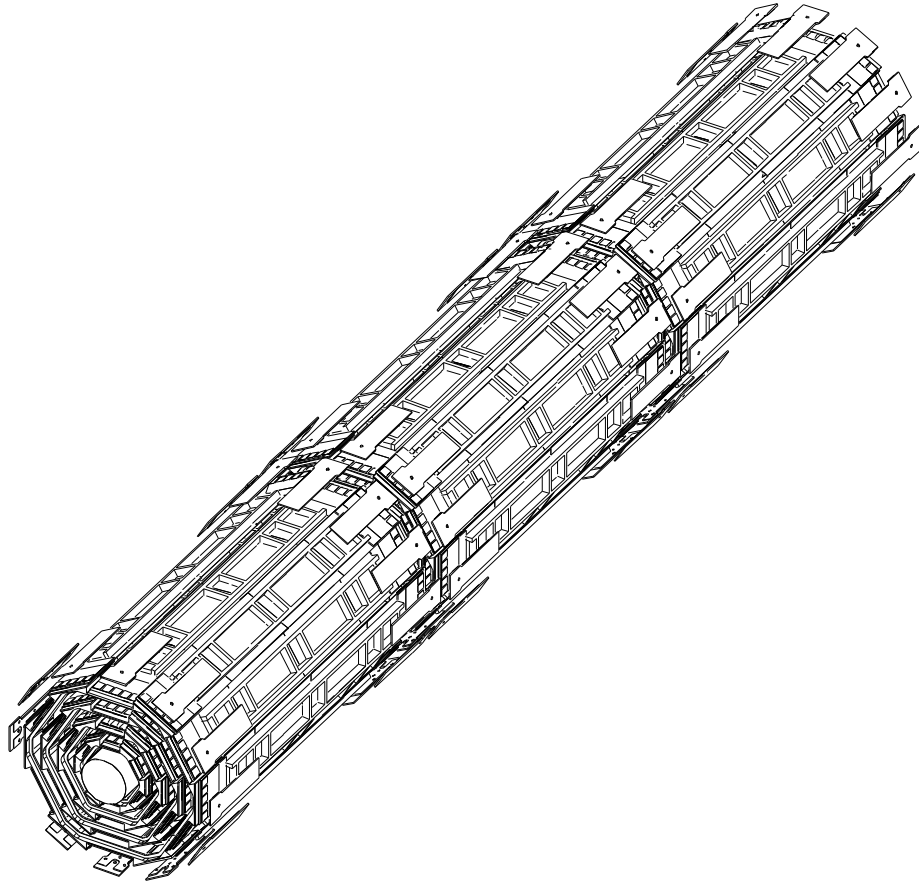
Figure 3–5: Isometric view of the three barrel structure of the CDF Silicon Vertex Detector.

It is located outside the L00 from 2.4 cm to 10.7 cm in radial coordinate. Both $r - z$ and $r - \phi$ coordinates are determined. This subsystem is used to trigger on displaced vertices which are an indication of heavy flavor content and helps with the track reconstruction. It is a complex system involving a total of 405,504

channels and unfortunately it is impossible to present it in any detail without going into too many technicalities.

Intermediate Silicon Layers. The ISL is composed of three layers of double-sided silicon with axial and small-angle stereo sides and it is placed just outside the SVX. The geometry is less intuitive but it can be seen in Figure 3–4: there is one layer in the central region ($|\eta| < 1$), at a radius of 22 cm. In the plug region ($1 < |\eta| < 2$) two layers of silicon are placed at radii of 20 and 28 cm, respectively.

The SVX and ISL are a single functional system which provides stand-alone silicon tracking and heavy flavor tagging over the full region $|\eta| < 2.0$.

Central Outer Tracker. It is a large open-cell drift chamber which provides tracking at relatively large radii, between 44 cm and 132 cm and it covers the region $|\eta| < 1.0$. It consists of four axial and four small angle ($\pm 3°$) stereo super-layers. The superlayers are divided in small cells ϕ and each cell contains 12 sense wires. The end-view of the COT detector is shown in Figure 3–6.

The cells are filled with a gas mixture of Ar-Et-CF$_4$ in proportions 50:35:15. The charged particles passing through the chamber ionize the gas and the produced electrons are attracted to the sense wires. When they arrive in the vicinity of the wire a process of avalanche ionization occurs and more electrons are produced and then collected by the wire. The location of the initial electron can be calculated based on the the sense wire which was hit and the drift velocity. This only describes how one 'point' of the trajectory is determined, but the process repeats in other cells and based on the location of many such hits a track trajectory is reconstructed. The important parameter to be reconstructed is the track curvature from which particle momentum is obtained. The COT has a resolution of about $0.7 \cdot 10^{-4} cm^{-1}$, which leads to a momentum resolution of $\delta p_T / p_T^2 \sim 0.3\% (GeV/c)^{-1}$. The typical drift velocity is about $100 \mu m/ns$.
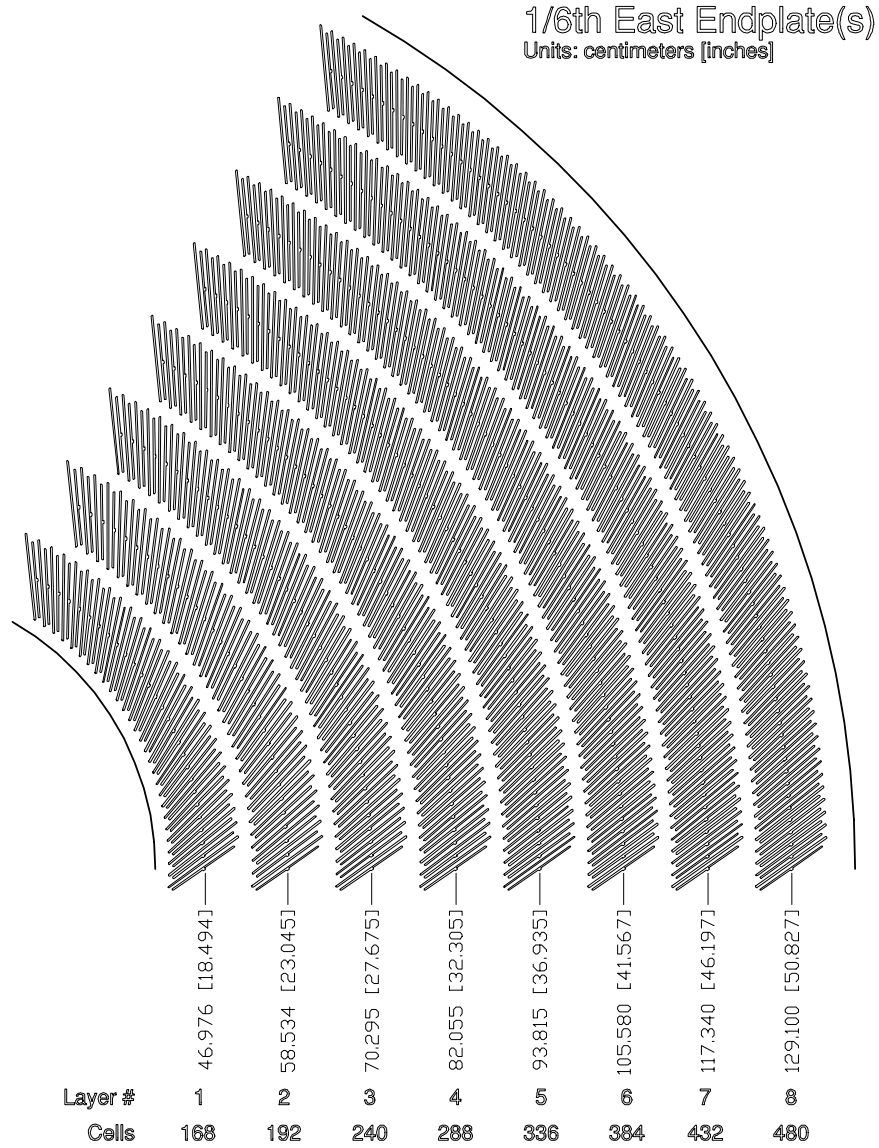
Figure 3–6: One sixth of the COT in end-view; odd superlayers are small-angle stereo layers and even superlayers are axial.

The COT allows for the reconstruction of tracks of charged particles in the $r - \phi$ and $r - z$ planes.

3.2.3   The Muon System

The Muon System is positioned farthest from the beam line and it is composed of four systems of scintillators and proportional chambers. They cover the region up to $|\eta| < 2$. In this analysis we only muons detected by the three central muon detectors known as the Central Muon Detector (CMU), Central Muon Upgrade

(CMP) and Central Muon Extension (CMX). Since these systems are placed behind the calorimeter and behind the return yoke of the magnet most other particles are absorbed by them. However, an extra layer of 60 cm of steel is added in front of the CMP for the same purpose of absorbing other particles. These three systems cover the region $|\eta| < 1.0$. The $1.0 < |\eta| < 2.0$ range is covered by the Intermediate Muon System (IMU), but we don't use it in this analysis.

3.2.4   The Trigger System

As mentioned earlier in Run II bunches of protons and antiprotons collide every 396 ns. The average number of $p\bar{p}$ collisions per bunch crossing depends on the instantaneous luminosity but for typical luminosities in Run II we expect one $p\bar{p}$ collision or more per bunch crossing therefore if we were to record all events we would need to save 1.7 million events per second. The typical event size is about 250 kB so at such a rate we would need to save 435 GB of data per second. However most $p\bar{p}$ collisions are diffractive inelastic collisions in which the proton or antiproton is broken into hadrons before the two are close enough such that a "hard core" interaction between partons can occur. These type of collisions are not of much interest and therefore there is no need to record them.

The purpose of the trigger system is to filter out these less interesting events, categorize and save the remaining ones. This is achieved through a 3-tier architecture shown in Fig. 3–7.

Level-1 (L1) and Level-2 (L2) trigger systems use only part of the entire event to make a decision regarding the event. They use dedicated hardware to perform a partial event reconstruction. At Level-1 all events are considered. They are stored in a pipeline since the L1 logic needs 4 μs to reach a decision, much longer than the 396 ns between two consecutive events. So while the decision making algorithm is executed by the L1 hardware the event is pushed down the pipeline, which serves the purpose of temporary memory. When the event reaches the end of

Dataflow of CDF "Deadtimeless" Trigger and DAQ

Detector

7.6 MHz Crossing rate
132 ns clock cycle

L1 Storage Pipeline:
42 Clock Cycles Deep

L1 trigger

Level1:
7.6 MHz Synchronous pipeline
5544ns latency
<50 kHz Accept rate

L1 Accept

L2 Buffers:
4 Events

L2 trigger

Level 2:
Asynchronous 2 stage pipeline
~20μs latency
300 Hz Accept Rate

L2 Accept

L1+L2 rejection: 20,000:1

DAQ Buffers

L3 Farm

Mass Storage

PJW 10/28/96

Figure 3–7: CDF II Data flow.

the pipeline the decision is made and the event is either ignored or allowed to move on to Level-2. It is important to bear in mind that the L1 trigger is a synchronous pipeline, with decision making pipelined such that many events are present in the L1 trigger logic simultaneously yet at different stages. Even though it takes 4 μs to reach a decision and even though events come every 396 ns the trigger analyzes them all, just not one at a time. The L1 trigger reduces the initial rate of about 1.7 MHz to below 20 kHz.

The Level-2 trigger is an asynchronous system with an average decision time of 20 μs. The events passing L1 are stored in one of the four L2 buffers waiting for a L2 decision. If an event arrives from L1 and all the L2 buffers are full the system incurs dead time and it is recorded during the run. The L2 trigger has a an acceptance rate of about 300 Hz, another significant reduction.

An event that passed L2 is transferred to the data acquisition (DAQ) buffers and then via a network switch to a Level-3 CPU node. L3 uses full event reconstruction to make a decision whether to write the event on tape or not. It consists of a "farm" of commercial CPUs, each processing one event at a time. If the event passes this level as well it is sent for writing on tape. The maximum output rate at L3 is 75 Hz, the main limitation being the data-logging rate with a typical value of 18 MB/s.

Events are classified according to their characteristics and separated into different trigger paths. Some of these classes of events are produced copiously and in order to leave enough bandwidth for less abundant event types a prescale mechanism is put in place. For example a prescale of 1:20 keeps only one event out of 20 that passed the trigger requirements.

CHAPTER 4
EVENT RECONSTRUCTION

The raw data out of the many subdetectors contains a wealth of information which is not always relevant from a physics analysis point of view. For instance, in this analysis we need to know the momenta of electrons, among other things. But what we do have in terms of raw data is a series of hits in the tracking system and energy depositions in the electromagnetic and hadronic calorimeters, and these readings could be caused by other particles, or may not be compatible with the trajectory of an electron in the magnetic field of the detector. Therefore detailed studies are necessary in order to find an efficient way of identifying raw data patterns compatible with those produced by an electron passing through the detector and at the same time reject as much fakes as possible.

In short the task of the event reconstruction is to identify the particles which were present in the event and measure their 4-momenta as well as possible. We will investigate this process in more detail for each kind of particle involved.

4.1   Quark and Gluons

Quarks and gluons produce a spray of particles via parton showering, hadronization and decay. Therefore they do not interact with the detector directly but appear as a more or less compact set of tracks and calorimeter towers in which energy has been deposited. By "compact" we mean compact in the $\eta - \phi$ plane. Such a detector pattern is called a jet and in this case the purpose of the reconstruction is to identify jets consistent with quark or gluon origins and estimate their overall energy and momentum.

4.1.1   Jet Clustering Algorithm

There are a couple of algorithms to identify these jets and estimate their energy. In this analysis we used an iterative "fixed cone" algorithm (JETCLU) for jet identification [15].

The idea is to find something like the center of the jet and then assign all towers within a given radius R in the $\eta - \phi$ plane around this center to that jet. The algorithm begins by creating a list of all seed towers, or the towers with transverse energy above some fixed threshold (1 GeV). Then, for each of the seed towers starting with the highest E_T tower, a precluster is formed by all seed towers within radius R of the seed tower. In this iterative process the seed towers already assigned to a precluster are removed from the list of available seed towers.

For each precluster a new center is found by doing an E_T weighted average of the $\eta - \phi$ positions of the towers pertaining to the precluster. This is called "centroid". Now using the centroids as origin we can recluster the the towers, this time allowing for the inclusion of towers with energy above a lower threshold (100 MeV). Again we compute the centroid and the process is repeated until it converges, when the latest centroid is very close to the previous centroid.

In the iterative procedure it is possible to have one tower belonging to two jets. But this would lead to inconsistencies because the total energy of the jets would not be equal to the total energy of the towers. Therefore after the iterative procedure is finished we have to resolve this double counting issue. One way is to merge the clusters that share towers. This happens if the overlapping towers' energy is more than 75% of the energy of the smaller cluster. But if this requirement is not satisfied each shared tower is assigned to the closest cluster.

In order to find the 4-momenta of the particles we assign a massless 4-momenta for each electromagnetic and hadronic tower based on the measured energy in the tower. The direction is given by the unit vector pointing from the event vertex to

the center of the calorimeter tower at the depth that corresponds to the shower maximum. The total jet 4-momenta is defined by summing over all towers in the cluster in the following way:

$$E \;=\; \sum_{i=1}^{N}(E_i^{em} + E_i^{had}) \tag{4-1}$$

$$p_x \;=\; \sum_{i=1}^{N}(E_i^{em}\, sin\,\theta_i^{em}\, cos\,\phi_i^{em} + E_i^{had}\, sin\,\theta_i^{had}\, cos\,\phi_i^{had}) \tag{4-2}$$

$$p_y \;=\; \sum_{i=1}^{N}(E_i^{em}\, sin\,\theta_i^{em}\, sin\,\phi_i^{em} + E_i^{had}\, sin\,\theta_i^{had}\, sin\phi_i^{had}) \tag{4-3}$$

$$p_z \;=\; \sum_{i=1}^{N}(E_i^{em}\, cos\,\theta_i^{em} + E_i^{had}\, cos\,\theta_i^{had}) \tag{4-4}$$

where $E_i^{em}, E_i^{had}, \phi_i^{em}, \phi_i^{had}, \theta_i^{em}, \theta_i^{had}$ are the electromagnetic and hadronic tower energies, azimuthal and polar angles for the ith tower in the cluster.

The jet 4-momentum depends on the choice of R. For small values towers pertaining to the original parton are not included in the cluster, while for large values we risk merging jets pertaining to separate partons. A compromise used in many CDF analysis is R = 0.4, and this is the value used here as well.

4.1.2   Jet Energy Corrections

The algorithm just presented returns an energy value that needs further corrections in order to reflect, on average, the parton energy. The reasons for the discrepancy are many, some instrumental and some due to underlying physical processes.

A few important instrumental effects are listed below:

- Jets in regions less instrumented, like in between calorimeter wedges or in the $\eta = 0$ region will naturally measure less energy.

- It is known that for low energy charged pions ($E_T < 10 GeV$) the calorimeter response is non-linear, while in the energy measurement procedure it is assumed linear.

- Charged particles with transverse momenta below 0.5 GeV/c are bent by the magnetic field and never get to the calorimeter.

- Fluctuations intrinsic to the calorimeter response.

Important physical effects are the following:

- The jet can contain muons which leave little energy in the calorimeter, and neutrinos which escape undetected. Therefore the cluster energy underestimates the parton energy.

- Choosing a radius R = 0.4 in the clustering algorithm we lose all towers rightfully pertaining to the jet but laying outside that radius.

- Extra particles can hit the same towers, coming either from other interactions present in the event or from the underlying event (the interaction of the proton and antiproton remnants, i.e. the quarks that did not take part in the hard process).

CDF developed a standard procedure [16] to correct for such effects. The user can choose to correct only for certain effects using the standard corrections and correct other effects with more analysis-specific corrections. This is also the case for this analysis, so we are using the standard corrections only for the instrumental effects. From there we use Monte Carlo simulations to map the correlation between the parton energy and the (partially) corrected measured jet energy.

<u>4.2   Electrons</u>

In this analysis we are using only electrons detected in the central calorimeter.

Most if not all of an electron's energy is deposited in the electromagnetic
calorimeter, therefore the reconstruction algorithm starts by identifying the list
of seed towers, which are towers with electromagnetic energy greater than $2\ GeV$.
Then, towers adjacent to the seed towers are added to the cluster if they have
non-zero electromagnetic or hadronic energy and are located in the same ϕ wedge
and nearest in η direction. At the end only clusters with electromagnetic E_T
greater than $2\ GeV$ and electromagnetic to hadronic energy ratio smaller than
0.125 are kept. However this last requirement regarding the ratio is ignored for
very energetic electrons with energy greater than $100\ GeV$.

What has been described above is just an "electromagnetic object" candidate.
It serves as basis for identifying both electrons and photons. Further selection
criteria [17] are necessary to identify electrons and separate them from photons or
isolated charged hadrons, π^0 mesons and jets faking leptons. These other criteria
are listed below:

- A quality COT track with a direction matching the location of the calorimeter
  cluster must be present.
- The ratio of hadronic energy to calorimeter energy (HADEM) satisfies
  $HADEM < 0.055 + 0.00045 \cdot E$, where E is the energy.
- Compatibility between the lateral shower profile of the candidate with that of
  test beam electrons.
- Compatibility between the CES shower profile and that of test beam
  electrons.
- The associated track's z position should be in the luminous region of the
  beam, which is within $60\ cm$ of the nominal interaction point.

- The ratio of additional calorimeter transverse energy found in a cone of radius R=0.4 to the transverse energy of the candidate electron is less than 0.1 (isolation requirement).

4.3   Muons

Muons leave little energy in the calorimeter but they can be identified by extrapolating the COT tracks to the muon chambers and looking for matching stubs there [18]. A stub is a collection of hits in the muon chambers that form a track segment. The muon candidates are preselected by requiring rather loose matching criteria between the COT track and the stubs. As for electrons, we apply a set of identification cuts [17] to separate muons from cosmic rays and hadrons penetrating the calorimeter:

- Energy deposition in the calorimeter consistent with a minimum ionizing particle, usually hadronic energy less than 6 GeV and electromagnetic energy less than 2 GeV. Small energy-dependent terms are added for very energetic muons with track momentum greater than 100 GeV.

- The distance between the extrapolated track and the stub is small, compatible with a muon trajectory. The actual value depends on the particular muon detector involved (CMP, CMU, CMX) but it is around 5 cm.

- The distance of closest approach between the reconstructed track to the beam line (d_0) is less than 0.2 cm for tracks containing no silicon hits and less than 0.02 cm for tracks containing silicon hits (which provide better resolution).

- As for electrons, the associated track's z position should be in the luminous region of the beam, within 60 cm of the nominal interaction point.

- The ratio of additional transverse E_T in a cone of radius R = 0.4 around the track direction is less than 0.1

<u>4.4   Neutrinos</u>

Neutrinos escape detection entirely but since the transverse momentum of the event is zero, and that includes neutrinos, we can indirectly measure their total $\vec{P}_T$ by summing all the transverse energy (momentum) measured in the detector and assigning any imbalance to neutrinos or other (undiscovered) long lived neutral particles escaping detection. This quantity is called "missing transverse energy" and it is defined

$$\not{E}_x = -\sum_{i=1}^{N}(E_i^{em}sin\,\theta_i^{em} + E_i^{had}sin\,\theta_i^{had})cos\phi_i \tag{4-5}$$

$$\not{E}_y = -\sum_{i=1}^{N}(E_i^{em}sin\,\theta_i^{em} + E_i^{had}sin\,\theta_i^{had})sin\phi_i \tag{4-6}$$

where E_i^{had}, E_i^{em} is the hadronic and respectively electromagnetic energy of the ith caloritemeter tower, θ^i is the the polar angle of the line connecting the event vertex to the center of the ith tower and ϕ_i is a weighted average defined by:

$$\phi_i = \frac{E_i^{em}sin\,\theta_i^{em}cos\phi_i^{em} + E_i^{had}sin\,\theta_i^{had}cos\phi_i^{had}}{E_i^{em}sin\,\theta_i^{em} + E_i^{had}sin\,\theta_i^{had}} \tag{4-7}$$

with $\phi_i^{em}, \phi_i^{had}$ weighted averages themselves but intratower.

In the calculation of $\vec{\not{E}}_T$ using the formulae above only towers with energy above 0.1 GeV are used. This requirement is applied individually to hadronic and electromagnetic components.

The magnitude $\not{E}_T$ is given by

$$\not{E}_T = \sqrt{\not{E}_x^2 + \not{E}_y^2} \tag{4-8}$$

Since muons do not leave much energy in the calorimeter and raw jet energy measurements are systematically low it follows that the above quantity is only a first order approximation for the neutrinos' P_T and needs further corrections.

The first correction is directly related to jet corrections. If we scale the energy of jets by some factor because that is a better match to parton energy then in computing the total measured $\vec{E}_T$ we should replace the raw jet energy measured by the calorimeter with the corrected energy as given by the jet energy corrections. These corrections are applied only to jets with E_T above $8\ GeV$, and therefore all calorimeter towers not included within such jets do not receive any correction.

The second correction is related to muons being minimum ionizing particles, leaving little energy in the calorimeter. Therefore a better estimate of the total $\vec{E}_T$ of the event is obtained by removing calorimeter towers associated with muons from the above calculations and replacing their contribution with the measured $\vec{P}_T$ of the muons.

In this analysis we use the missing E_T value only for event selection. It plays no role in the reconstruction of the invariant mass and therefore more detailed studies on missing E_T resolution are not included here.

CHAPTER 5
EVENT SELECTION AND SAMPLE COMPOSITION

The top quark decays so quickly that it does not have time to form any top hadrons and therefore a $t\bar{t}$ final state appears under different signatures based on the decay chain of the top quark:

$$t \to W^+ b \tag{5-1}$$

$$W^+ \to l^+ \nu_l \quad , \quad W^+ \to q\bar{q}' \tag{5-2}$$

where l stands for one of the charged lepton types e, μ or τ, q stands for u or c and q' for one of the "down" quarks d, s or b.

The top quark can also decay to either a d or a s quark instead of b but the combined branching ratios for these two processes are below 1% and generally ignored.

Based on these decay modes we can see that a $t\bar{t}$ pair decay can appear under three different experimental signatures:

- Six jets or sometimes more due to radiation, when both W bosons decay hadronically. This is the "hadronic" channel.
- Four jets or more, a charged lepton and missing $\vec{E}_T$ when only one W boson decays hadronically. This is the "lepton+jets" channel.
- Two jets or more, two charged leptons of opposite sign and missing $\vec{E}_T$ when both W bosons decay leptonically. This is the "dilepton" channel.

The scheme is complicated a bit because the τ lepton also decays before detection and it can either "transform" into a jet, if it decays hadronically, or

37

produce an electron or a muon and more neutrinos, if it decays leptonically. However, regardless of the τ decay mode, these events are difficult to identify and we decided to develop an algorithm which should work well with non-τ events only.

The branching ratios are defined essentially by the W branching ratios and lead to the following numbers:

Table 5–1: $t\bar{t}$ decays

Category	Branching Ratio
Dilepton (excluding τ)	5%
Dilepton (at least one τ)	6%
Lepton+Jets (excluding τ)	30%
τ+Jets	15%
Hadronic	44%

5.1   Choice of Decay Channel

The choice for the decay channel has to take into account two more factors, the intrinsic $M_{t\bar{t}}$ reconstruction resolution and the signal to background ratio (S/B). The reconstruction resolution is worse when more information is missing. Let us take a look at each channel individually:

- In the dilepton channel we measure well the lepton momenta, we have some uncertainty on the two b quark momenta due to various effects described in the previous chapter, and we don't measure at all the momenta of the two neutrinos (6 variables).

- In the lepton+jets channel we measure well the lepton momentum, we have some uncertainty on the four quark momenta and we don't measure at all the neutrino momenta (3 variables).

- In the hadronic channel we have some uncertainty on the six quark momenta.

In each case we can reduce the number of unknown variables by applying transverse momentum conservation, which yields two constraints, but since this is the same across the channels we can just compare them based on the facts stated above. If non-$t\bar{t}$ backgrounds were absent we would certainly pick the hadronic

channel since it has the highest branching ratio and least loss of information because no neutrinos escape detection. However the S/B ratio for Standard Model $t\bar{t}$ in the hadronic channel, without any tagging requirement, is about 1:20 while the S/B ratio for the lepton+jets channel is roughly 1:2 with a branching ratio (2/3) comparable to the hadronic channel. Even though the resolution analysis would also favor the hadronic channel, with such a large background it has, most probably, less potential than the lepton+jets channel.

The dilepton channel has most unknown variables leading to poorest reconstruction resolution and significantly lower branching ratio, even though it enjoys the best S/B around 3:1.

This qualitative analysis led us to pick the lepton+jets channel as best candidate for this analysis at the beginning of Run 2 when we expected less than 1 fb^{-1} of integrated luminosity available for this dissertation. The final dataset on which this analysis is performed corresponds to 680 pb^{-1} of data.

5.2   Data Samples

The data used in this analysis was collected between February 2002 and September 2005. A preselection of the data is carried out by the collaboration and bad runs in which various components of the detector malfunctioned are removed. The remaining good data corresponds to a total integrated luminosity of 680 pb^{-1}.

Two distinct datasets were used, the high P_T central electron dataset and the high P_T muon dataset. The electron dataset is selected by a trigger path that requires a Level-3 electron candidate with CEM $E_T^{em} > 18 GeV$, $E^{had}/E^{em} < 0.125$ and a COT track with $p_T > 9 GeV/c$. The muon dataset is selected by a trigger path that requires a Level-3 muon candidate with $p_T > 18 GeV/c$. We use only CMX muons or muons with stubs in $both$ CMU and CMP subdetectors.

Dilepton $e - \mu$ events can appear in both datasets and one has to be careful to not double count them.

<u>5.3   Event Selection</u>

In order to select $t\bar{t}$ events in the lepton+jet channel we have to require that each event contains at least four jets, an electron or a muon and $\displaystyle{\not}E_T$ consistent with the presence of a neutrino, that is, a $\displaystyle{\not}E_T$ value well above the fluctuations around the null measurement.

Certainly this leaves a lot of space of maneuver with respect to the η range and the minimum E_T threshold required for each object. An exhaustive study for optimizing the cuts has not been done independently, however we adopted the widely used cuts for Standard Model $t\bar{t}$ selection in the lepton+jets channel which can be found in most CDF top analyses. These cuts are the result of a great amount of work throughout Run 1 and Run 2 and are doing a fine job at separating signal (Standard Model $t\bar{t}$ in this case) from backgrounds. There could be better cuts that improve the *resonant* $t\bar{t}$ S/B but further studies would be necessary to understand the overall effect on sensitivity, and what would be an optimum for a $400\ GeV/c^2$ mass resonance may not be so for a $800\ GeV/c^2$ resonance. The task of studying in detail the impact of selection criteria on sensitivity will have to be addressed in a later version of the analysis. However we did compare the sensitivity among three versions of jet selections and chose the best, as it will be explained later.

Table 5–2: Event Selection

Object	Requirements
Electron	CEM, fiducial, not from a conversion
	$E_T > 20\ GeV$ + ID cuts
Muon	CMX or (CMU and CMP) detectors, not cosmics
	$P_T > 20\ GeV$ + ID cuts
$\vec{{\not}E}_T$	Corrected $\displaystyle{\not}E_T > 20\ GeV$
Tight Jets	Corrected $E_T > 15\ GeV$, $|\eta| < 2.0$
	at least four tight jets
Loose Jets	Corrected $E_T > 8\ GeV$, $|\eta| < 2.4$
	not used for selection per se, but counted as jets

In table 5–2 we present in a succinct form the requirements [19] for the selection of electrons, muons, jets and the $\not{E}_T$ cut used. Positrons and antimuons follow the same selections, of course. By "fiduciality" of electrons it is meant that they are located in well instrumented areas of the towers, not near tower edges for instance. Conversion removal algorithms are used to remove electrons or positrons that come from photons hitting the various materials found before the calorimeter and producing e^-e^+ pairs. We are not interested in such electrons. The removal per se is done by a standard CDF algorithm [20]. There is also an algorithm for eliminating cosmic ray muons [21] and it is used to veto on such muons in our selection. We also require one and only one lepton and that the distance between the lepton's track $Z0$ coordinate and the jets' vertex position is less than 5 cm, since consistency with $t\bar{t}$ production requires that all our objects must come from the same interaction point. The identification criteria complete the event selection rules and were discussed in the previous chapter, together with the corrections for $\vec{\not{E}}_T$ and jets.

A simple study was performed in which we compared the sensitivities of three jet selection criteria:

- exactly tight four jets
- four tight jets + extra jets (or none)
- three tight jets + extra jets (> 0).

The first option provided the best sensitivity and we adopted it for our selection.

<div align="center">5.4   Sample Composition</div>

The leading Standard Model processes that can produce events passing these selection criteria are the following:

- W production associated with jets (W+jets). The W decays leptonically producing a lepton and $\vec{\not{E}}_T$.
- $t\bar{t}$ events.

- Multijet events where one jet fakes an electron. Will will refer to these generically as QCD.

- Diboson events such as WW, WZ and ZZ.

The relative contribution of these processes can be derived if we know the theoretical cross-section and the acceptance for each of them.

Table 5–3: Cross-sections and acceptances

Process	cross-section	Acceptance
SM $t\bar{t}$	6.7 pb	4.5%
WW	12.4 pb	0.14%
WZ	3.7 pb	0.08%
ZZ	1.4 pb	0.02%
W+jets	?	0.7%
QCD	?	0.7%

However the W+jets and QCD cross-sections are not known theoretically with good precision, but in other CDF top analyses the number of events from these processes is extracted from the data.

For this analysis we decided to use only the ratio of the expected number of events as derived by these analyses and fit for the absolute normalization since in those analyses no room was left for any non-Standard Model process, and that could bias our search.

The constraint used is given below:

$$\frac{N_{QCD}}{N_W} = 0.1 \qquad \qquad (5\text{-}3)$$

where N represents the expected number of events.

Resonant $t\bar{t}$ acceptances are listed for comparison in Table 5–4.

The search algorithm finds the most likely values for N_W and signal cross-section as a function of resonance mass, and it is also able to compute the statistical

Table 5–4: Signal acceptances

M_{X^0} (GeV/c^2)	Acceptance
450	0.047
500	0.051
550	0.055
600	0.057
650	0.059
700	0.062
750	0.062
800	0.063
850	0.063
900	0.061

relevance of the most likely signal cross-section value. We will explore it in detail in the next chapters.

CHAPTER 6
GENERAL OVERVIEW OF THE METHOD AND PRELIMINARY TESTS

This analysis contains two major pieces, one is the $t\bar{t}$ invariant mass ($M_{t\bar{t}}$) reconstruction and the second is the search for a non-Standard Model component in that spectrum, in particular a resonance contribution.

The reconstruction is complicated because our parton level final state, after the top decay chain, is composed of two b-quarks, two light quarks, a neutrino and a charged lepton. Experimentally, we measure accurately only the lepton, which makes the task of reconstructing the $t\bar{t}$ invariant mass spectrum with good precision non-trivial. There are a total of seven poorly measured or unmeasured variables: four quark energies and three components of neutrino momenta. In fact the jet direction is also smeared compared to the parton direction, but this is considered a second order effect compared to the above mentioned effects. Throughout the remaining of this dissertation we will always assume that the jet direction is a good approximation for the parton direction.

In the CDF Run 1 analysis [11] a somewhat straightforward approach was used to reconstruct the invariant mass spectrum. A χ^2 fit was constructed based on jet resolutions and the knowledge of W and t masses and it was used to weight the unknown parton values. Minimizing the χ^2 with respect to the free parameters (the unknowns listed above) provided an estimate for their most probable values. Then those values were used to compute the invariant mass of the system, $M_{t\bar{t}}$.

In this dissertation we use an innovative approach using matrix element information to reconstruct the $t\bar{t}$ invariant mass spectrum. The maximum information about any given process is contained in its differential cross-section

and it is therefore natural to think that by making use of more information in the analysis one can improve resolution and therefore sensitivity.

Since we decided to pursue a model independent search we will not be able to use any resonance matrix elements. We will use Standard Model $t\bar{t}$ matrix element to help with weighting the various possible parton level configurations and extract an average value for the invariant mass, event by event. The invariant mass distribution obtained in such a way follows closely the Standard Model $t\bar{t}$ spectrum at parton level and it is also a good estimator for the resonant $t\bar{t}$ events as it will be shown later.

In order to validate the matrix element machinery we performed a series of tests by implementing a conceptually simpler matrix element analysis, which is the top mass measurement using matrix elements. Our tests include only Monte Carlo simulation studies but they played a crucial role in pushing this analysis forward since our results were very similar to those of groups actually working on the top mass measurement using matrix element information. The remainder of this chapter will present these studies which will also familiarize to reader with the technical details common to both analyses. In the next chapter we will show how to extend the algorithm in order to reconstruct the $M_{t\bar{t}}$ spectrum.

<u>6.1   Top Mass Measurement Algorithm</u>

The purpose of this algorithm is to build a top mass dependent likelihood for each event using the differential cross-section for the SM $t\bar{t}$ process. We will use the leading order (LO) term in the Standard Model $t\bar{t}$ cross-section formula. The final state is made up of the 6 decay products of the $t\bar{t}$ system. Let $\vec{p}_i$ be their 3-momenta. We have the following equation representing the conservation of the transverse momentum of the system:

$$\vec{P_6^T} = \sum_{i=1}^{6} \vec{p}_i^T = 0 \tag{6-1}$$

This is a constraint on the seven unknown variables mentioned in the previous chapter and it will be used in all the top mass tests we will show in this chapter.

In reality we have initial and final state radiation (ISR and FSR) which leads to a non-zero $\vec{P_6^T}$ value. Still, the average $\vec{P_6^T}$ is null so constraining it to 0 should not bias the result for top mass but maybe only increase the statistical error. For the resonance search analysis though we will use the $\vec{P_6^T}$ distribution from Monte Carlo simulation and integrate over it since it helps narrow the reconstructed resonance peak.

The probability of a given parton level final state configuration $\vec{p_i}$ *relative to other configurations* is given by:

$$dP(\vec{p_i}|m_{top}) = \frac{1}{\sigma(m_{top})} \int dz_a \int dz_b f_k(z_a) f_l(z_b) d\sigma_{kl}(\vec{p_i}|m_{top}, z_a\vec{P}, z_b\vec{\bar{P}}) \qquad (6\text{-}2)$$

or in short

$$dP(\vec{p_i}|m_{top}) = \pi_{part}(\vec{p_i}|m_{top}) \prod d^3\vec{p_i} \qquad (6\text{-}3)$$

Indices k, l cover the partons types in the proton and antiproton respectively. Summation over both indices is implied. The parton distribution functions (PDFs) are given by $f_k(z)$ and $\vec{P}$, $\vec{\bar{P}}$ designate the proton and antiproton momentum. Plugging in the differential cross-section formula

$$d\sigma_{kl}(\vec{p_i}|p_k, p_l) = \frac{|\mathcal{M}_{kl}|^2}{4E_k E_l |v_k - v_l|}(2\pi)^4 \delta^4(p_k + p_l - \Sigma p_i) \prod \frac{d^3\vec{p_i}}{(2\pi)^3 2E_i} \qquad (6\text{-}4)$$

one can obtain an explicit form for $\pi_{part}(\vec{p_i}|m_{top})$. The top mass ($m_{top}$) enters as a parameter.

We combine the probability densities (π) of all events in the sample into a joint likelihood which is a function of m_{top}:

$$L(m_{top}) = \pi_1 \pi_2 ... \pi_n \qquad (6\text{-}5)$$

We expect that maximizing this likelihood with respect to the parameter (m_{top}) yields its correct (input) value, as it should.

The algorithm presented above is only a first step, since it assumes we know the parton level momenta which is not true experimentally. But the treatment of more realistic situations in which we don't measure the final state completely or accurately enough follows the same line of thought, basically we compute the probability density of observing a lepton+jet event:

$$\pi_{obs}(\vec{j_1}, \vec{j_2}, \vec{j_3}, \vec{j_4}, \vec{p_l}|m_{top}) =$$

$$= \sum_{\rho} \int \pi_{part}(\vec{p}_{\rho(1)}, \vec{p}_{\rho(2)}, \vec{p}_{\rho(3)}, \vec{p}_{\rho(4)}, \vec{p_l}, \vec{p_\nu}|m_{top})d^3\vec{p_\nu} \prod_{i=1}^{4} T_i(\vec{j}_{\rho(i)}|\vec{p}_{\rho(i)})d^3\vec{p_i} \quad (6\text{-}6)$$

In this formula we assume that the first two arguments of the parton density (π_{part}) function represent the b-quark momenta, the jet 3-momenta are denoted by $\vec{j_i}$ and the parton 3-momenta by $\vec{p_i}$. $T_i(\vec{j}|\vec{p})$ is the probability density that a parton with 3-momenta $\vec{p}$ is measured as a jet with 3 momenta $\vec{j}$. These functions are called parton-to-jet transfer functions. We use different transfer functions for b quarks and lighter quarks, so we added an index to differentiate the two. With our conventions $T_1 = T_2 = T_b$ and $T_3 = T_4 = T_{light}$. In practice we approximate the parton direction with the jet direction, as mentioned earlier, which simplifies the calculations a bit.

Even with b-tagging information available, there is no unique assignment of jets to partons. This indistinguishability is addressed by summing over all *allowed* permutations using the $\rho \in S_4$ permutation variable. A permutation is allowed if it doesn't contradict available b-tagging information.

The procedure to extract the top mass is the same as in the idealized case of a perfect measurement of the final state discussed before, that is, combine all events in a joint likelihood and maximize it with respect to the parameter m_{top}.

Figure 6–1: Main leading order contribution to $t\bar{t}$ production in $p\bar{p}$ collisions at $\sqrt{s} = 1.96$ TeV

6.1.1   The Matrix Elements (ME)

The leading order matrix element for the process $q\bar{q} \to t\bar{t} \to W^+bW^-\bar{b} \to q\bar{q}bl\bar{\nu}\bar{b}$ (Fig. 6–1) is not easily calculable analytically without making any approximation. We found it useful to compute the ME directly using explicit spinors and Dirac matrices because this allows us to compute new, non-Standard Model matrix elements very easily in case we wanted to incorporate them in the algorithm later on. Dedicated searches for specific models (spin 0 resonance, spin 1 resonance, color octet resonance) would be interesting as well, but we will not address them in this dissertation.

Ignoring numerical factors the quark annihilation diagram amplitude is given by

$$
\begin{aligned}
\mathcal{M}_{q\bar{q}} \approx\; & \bar{v}(p_{\bar{q}})\gamma^\mu u(p_q) \cdot \bar{u}(p_u)\gamma^\beta(1-\gamma^5)v(p_{\bar{d}}) \cdot \bar{u}(p_l)\gamma^\sigma(1-\gamma^5)v(p_{\bar{\nu}}) \cdot \\
& \bar{u}(p_b)\gamma^\alpha(1-\gamma^5)\frac{\not{p}_t + m_t}{p_t^2 - m_t^2 + im_t\Gamma_t}\gamma^\nu \frac{\not{p}_{\bar{t}} + m_t}{p_{\bar{t}}^2 - m_t^2 + im_t\Gamma_t}\gamma^\rho(1-\gamma^5)v(p_{\bar{b}}) \cdot \\
& \frac{g_{\mu\nu}}{(p_q+p_{\bar{q}})^2} \cdot \frac{g_{\alpha\beta} - P_\alpha^{W^+}P_\beta^{W^+}/m_W^2}{P_{W^+}^2 - m_W^2 + im_W\Gamma_W} \cdot \frac{g_{\rho\sigma} - P_\rho^{W^-}P_\sigma^{W^-}/m_W^2}{P_{W^-}^2 - m_W^2 + im_W\Gamma_W} \qquad (6\text{-}7)
\end{aligned}
$$

If we consider the masses of the light quarks and leptons negligible we can simplify the expression of the W propagators so the ME reads

$$\mathcal{M}_{q\bar{q}} \approx \frac{\bar{v}(p_{\bar{q}})\gamma^\mu u(p_q)}{(p_q + p_{\bar{q}})^2} \cdot \frac{\bar{u}(p_u)\gamma^\alpha(1-\gamma^5)v(p_{\bar{d}})}{P_{W^+}^2 - m_W^2 + im_W\Gamma_W} \cdot \frac{\bar{u}(p_l)\gamma^\sigma(1-\gamma^5)v(p_{\bar{\nu}})}{P_{W^-}^2 - m_W^2 + im_W\Gamma_W} \cdot$$
$$\bar{u}(p_b)\gamma_\alpha(1-\gamma^5)\frac{\slashed{p}_t + m_t}{p_t^2 - m_t^2 + im_t\Gamma_t}\gamma_\mu\frac{\slashed{p}_{\bar{t}} + m_t}{p_{\bar{t}}^2 - m_t^2 + im_t\Gamma_t}\gamma_\sigma(1-\gamma^5)v(p_{\bar{b}}) \quad (6\text{-}8)$$

We tested our numerical calculation using explicit Dirac matrices and spinors with the analytical calculation for the squared amplitude by Barger [22] and we found the two calculations in good agreement. That calculation uses the narrow width approximation (NWA) in treating the top quark propagators and therefore the two methods are not equivalent when one or both of the top masses are off-shell.

We also tested our implementation on simpler QED matrix element calculations and it produced results identical with their exact analytical expressions.
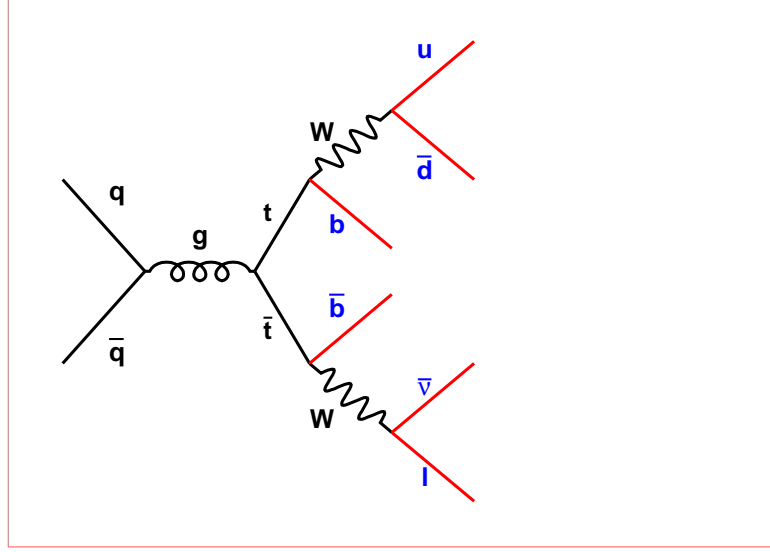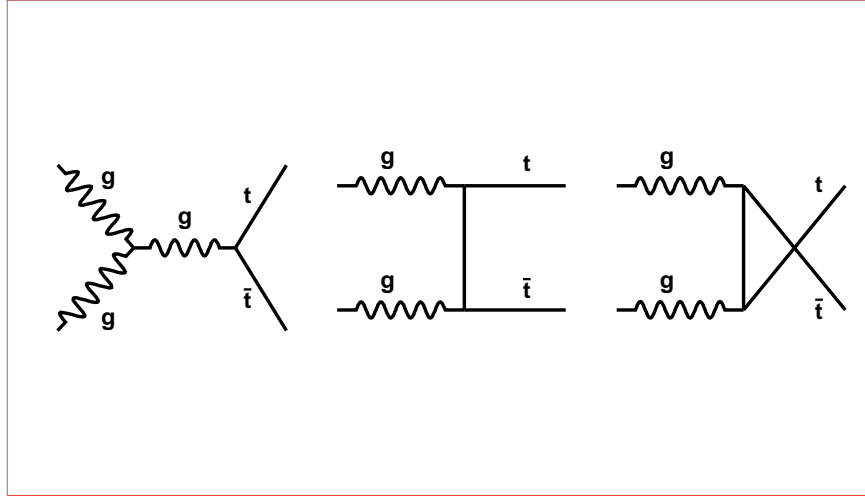

Figure 6–2: Gluon-gluon leading order contribution to $t\bar{t}$ production in $p\bar{p}$ collisions at $\sqrt{s} = 1.96$ TeV

The gluon-gluon production mechanism is described by three diagrams in Fig. 6–2, in which the top decays have not been depicted explicitly.

The matrix element needed in the cross-section formula for the gluon-gluon production mechanism has the structure:

$$|\mathcal{M}_{gg}|^2 = \frac{1}{64} \sum_{color} |\mathcal{A}_1 + \mathcal{A}_2 + \mathcal{A}_3|^2 \tag{6-9}$$

where $\mathcal{A}_i$ are the amplitudes corresponding to the three diagrams. The color sum covers all possible color configurations for the gluons and quarks. This expression is not optimal with regard to CPU time if we were to do these sums as they stand. We can rewrite it as

$$|\mathcal{M}_{gg}|^2 = \frac{1}{64} \sum_{color} (|\mathcal{A}_1|^2 + |\mathcal{A}_2|^2 + |\mathcal{A}_3|^2 + 2 \cdot Re\{\mathcal{A}_1\mathcal{A}_2^*\} + 2 \cdot Re\{\mathcal{A}_1\mathcal{A}_3^*\} + 2 \cdot Re\{\mathcal{A}_2\mathcal{A}_3^*\}) \tag{6-10}$$

This form is very convenient, the color sums can be evaluated for each individual term regardless of the kinematics because the amplitudes are factorized as $\mathcal{A} = \mathcal{A}^{kin} \cdot \mathcal{A}^{color}$

We can write again

$$|\mathcal{M}_{gg}|^2 = f_1 \cdot |\mathcal{A}_1^{kin}|^2 + f_2 \cdot |\mathcal{A}_2^{kin}|^2 + f_3 \cdot |\mathcal{A}_3^{kin}|^2 +$$
$$Re\{f_{12} \cdot \mathcal{A}_1^{kin}\mathcal{A}_2^{kin*} + f_{13} \cdot \mathcal{A}_1^{kin}\mathcal{A}_3^{kin*} + f_{23} \cdot \mathcal{A}_2^{kin}\mathcal{A}_3^{kin*}\} \tag{6-11}$$

All the color summing is encoded in the six constants f_i, f_{ij}. We found these to be 3/16, 1/12, 1/12, -3i/16, 3i/16 and -1/48 respectively. We cross-checked against the analytical formula available for the $2 \to 2$ process described in the diagrams above (ignoring the top decays) and found them in perfect agreement.

The procedure just presented works as well for the $2 \to 6$ process and this is how we compute it.

6.1.2   Approximations: Change of Integration Variables

The method as presented involves seven integrals (three over neutrino 3-momentum and four over quark momenta) and summing over combinatorics. If for instance we choose to set the $t\bar{t}$ transverse momentum to zero that would

amount to two constraints reducing the number of integrals by two. Or we could choose to set the W or top on shell, depending on the level of precision and speed desired. Even from a purely numerical point of view, it would be easier to integrate only around the top and W mass poles rather than over the large range of the original variables mentioned before.

For all these reasons a change of variable was performed. The new variables are the $t\bar{t}$ transverse momentum and the intermediate particle masses m_{W1}, m_{W2}, m_{T1}, m_{T2}. This is a set of only six new variables, which means we need to keep one of the initial variables unchanged (one of the light quarks' energy).

The change of variable and the associated Jacobian calculations are detailed in the Appendix. Since the calculations are a bit lengthy we wanted to make sure no mistake was made so we used simulated events where all variables are available and any change of variables can be readily checked. We found that the change of variable implementation works very well.

In the implementation of the algorithm we always use these variables, both for these preliminary top mass tests and for the $M_{t\bar{t}}$ reconstruction.

6.2   Monte Carlo Generators

For some of the top mass tests we used CompHep 4.4 [23], which is a matrix element based event generator. One can select explicitly which diagrams to use for event generation. CompHep preserves all spin correlations and off-shell contributions since it doesn't attempt to simplify the diagrams in any way. CompHep generates events separately for each diagram $u\bar{u} \rightarrow t\bar{t}$, $d\bar{d} \rightarrow t\bar{t}$ and $gg \rightarrow t\bar{t}$.

We also used Pythia [24] and Herwig [25] official CDF samples ("Gen5") but the first tests for top mass were done with parton level CompHep events and then with Gaussian smeared partons. The Gaussian smearing of parton energies is meant to simulate the relationship between the jet and parton energies.

6.3   Basic Checks at Parton Level
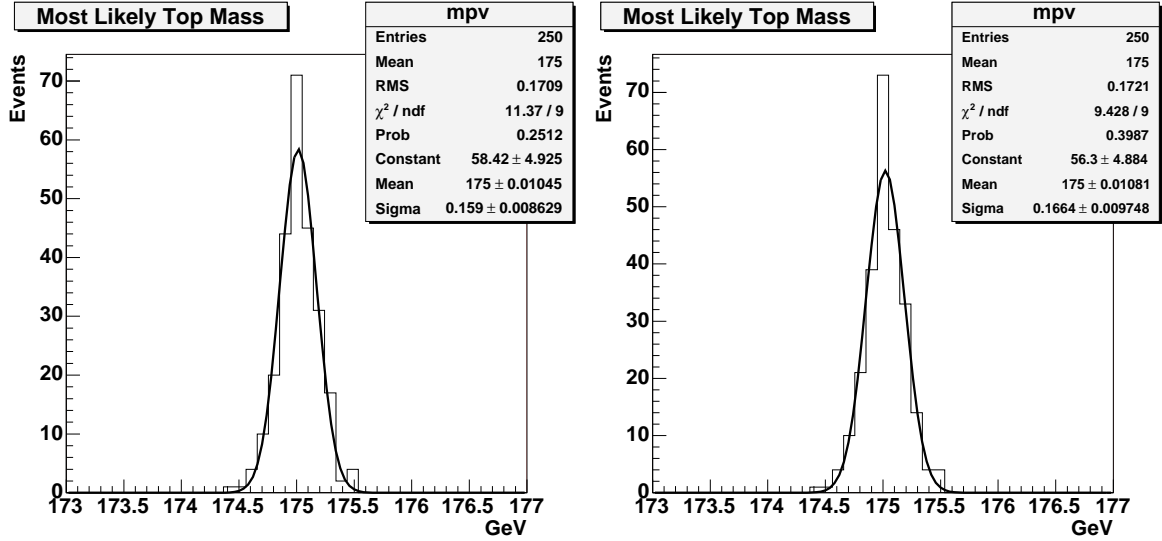
Figure 6–3: Reconstructed top mass from 250 pseudoexperiments of 20 events at parton level with m_t=175 GeV/c^2. The left plot is derived using only the correct combination, while the right plot uses all combinations

Finding the top mass when the final state is known or measured perfectly is straightforward so we expect our method to produce the correct answer without any bias. Using $u\bar{u} \rightarrow t\bar{t}$ CompHep events, we performed 250 pseudoexperiments of 20 events each. Which means that we extracted the top mass from a joint likelihood of 20 events each time. We repeated this exercise for various generator level top masses to make sure there is no mass dependent bias.

First, we used only the correct combination in the likelihood, that is, we not only assumed to have measured the parton 3-momenta ideally, but also identified the quark flavors.

For $m_t = 175$ GeV the reconstructed mass is shown in the right plot of Figure 6–3. As it can be seen, we get back the exact input mass. Similarly good results were obtained for other masses.

Next we let all 24 combinations contribute to the event likelihood by summing over all permutations and repeated the same exercise. The reconstructed top mass

is barely modified by the inclusion of all combinations, as shown in the second plot of Figure 6–3. Again, tests on other samples with different top masses didn't produce any surprise. These results are summarized in Figure 6–4 showing the output (reconstructed) mass *vs* input mass when using all combinations. The slope is consistent with 1.0 and the intercept is consistent with 0, which proves that there are no mass dependent effects, at least not in the mass range of interest. Perhaps it would be useful to remind the reader that the purpose of these studies is to establish the validity of the matrix element calculations and overall correctness of implementation of a non-trivial algorithm. Otherwise they are quite simple.

We also looked at the *rms* of the pull distributions for each mass and it was found to be 1.0 within errors, which is a more compelling indication that we are modeling these events very well with our likelihood.
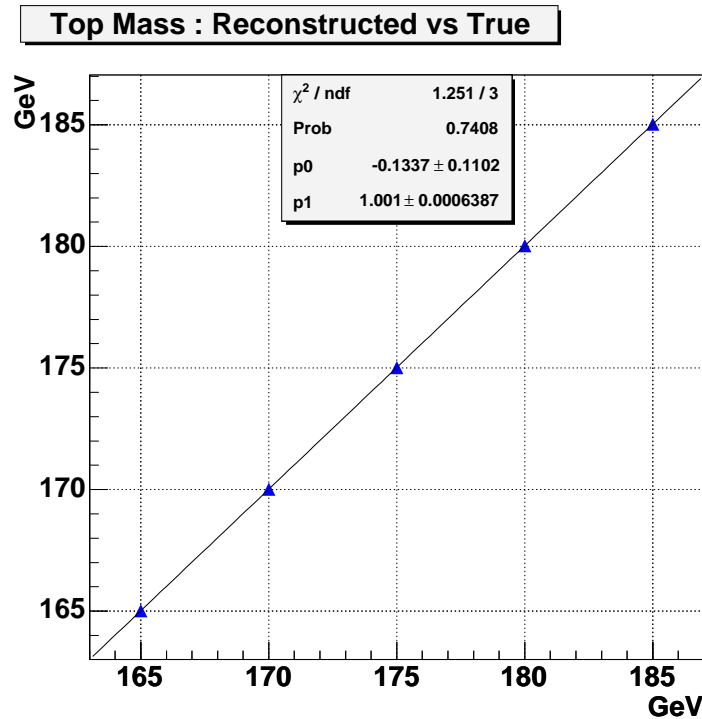
Figure 6–4: Reconstructed top mass vs. true top mass from pseudoexperiments of 20 events using all 24 combinations, at parton level

6.4   Tests on Smeared Partons

A more realistic test involves a rudimentary simulation of the calorimeter response obtained by smearing the parton energies (the four final state quarks' energies). Also, the neutrino 3-momentum information is ignored in reconstruction. We used 20% Gaussian smearing, which is quite realistic when compared to parton-to-jet transfer functions' rms. The $t\bar{t}$ transverse momentum was taken to be zero and also the top quark was forced on shell, thus the number of integrals was reduced to just three.

We used the same $u\bar{u} \to t\bar{t}$ CompHep events for these tests but later we did check with Herwig events and the results were similar.

The same pseudoexperiments of 20 events were performed and in Figure 6–5 we show the reconstructed mass vs the true mass for the right combination and for all 24 combinations.
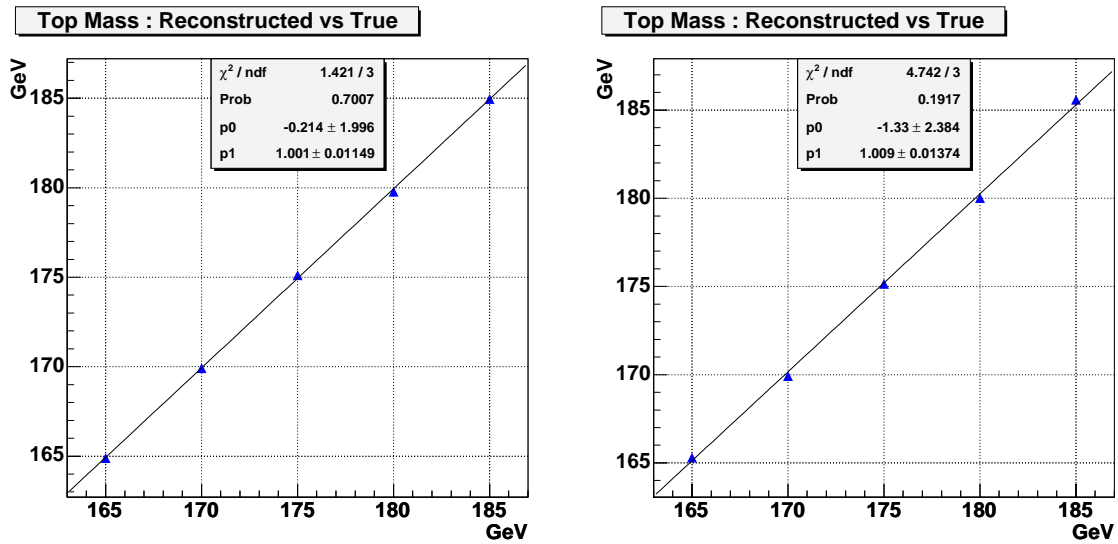
Figure 6–5: Reconstructed top mass vs. true top mass from pseudoexperiments of 20 events with smearing. The left plot is derived using only the correct combination, while the right plot uses all combinations

We fit the pulls from pseudoexperiments with a Gaussian and the returned width was 1.09 ± 0.07 for the 175 GeV sample, again consistent with 1. We observed similar pulls for other masses as well.

The purpose of this set of tests was to validate the new additions to the algorithm implementation: transfer functions, transformation of variables and integration over unmeasured quantities. The success of this tests gives us confidence that the more realistic version of the algorithm is well designed and well implemented.

6.5   Tests on Simulated Events with Realistic Transfer Functions

6.5.1   Samples and Event Selection

We used CDF official $t\bar{t}$ samples generated with Pythia and Herwig event generators. We apply the event reconstruction and event selection described in the previous chapters requiring for each event to contain one and only one reconstructed charged lepton, at least four tight jets and missing $E_T > 20\ GeV$.

6.5.2   Transfer Functions

Transfer functions are necessary when we run over simulated events or data in order to describe the relationship between final state quark momenta and jet momenta. In this case we are interested in the probability distribution of the jet energy given the parton energy. This distribution varies with the energy and pseudorapidity of the parton, so we bin it with respect to these variables.

Since the detector is forward-backward symmetric we only need to bin in absolute pseudorapidity. We have only three bins in absolute pseudorapidity, with the boundaries at 0 , 0.7, 1.3 and 2.

The parton energy bins are determined based on the statistics available, requiring minimum 3000 parton-jet pairs per energy bin. This allows for a rather smooth function which can be fit well. For example the central region b-quark energy bin boundaries are chosen to be 10 GeV, 37 GeV, 47 GeV, 57 GeV, 67

GeV, 77 GeV, 87 GeV, 97 GeV, 107 GeV, 117 GeV, 128 GeV, 145 GeV, and 182 GeV. Anything above 182 GeV is considered part of one more bin. We should perhaps emphasize that these are *parton* energy bins.

In order to derive the transfer functions we need to match jets to partons first. For matching purposes we require that all four final state quarks are matched uniquely to jets in a cone of 0.4, that is, the ΔR distance between the parton direction and jet direction is less than 0.4. If this requirement is not met, we do not use the event for deriving transfer functions.

The direction smearing is considered a second order effect and ignored, which amounts to identifying the quark direction with the jet direction. This approximation can be corrected to some degree by using "effective widths" for W and top instead of theoretical values. In other words the smearing in direction leads to a smearing of the mass peak even when there is no energy smearing. The effect can be quantified based on simulation and a corresponding larger width can be employed in the analysis. In fact we do use such a larger width (4 GeV) for the hadronic W mass in our resonance search analysis. Our studies showed that it narrows the resonance peak a bit, but no such tests were performed for top mass.

Figure 6–6: Light quarks transfer functions ($x = 1 - \frac{E_{jet}}{E_{parton}}$), binned in three absolute pseudorapidity regions [0, 0.7], [0.7, 1.3] and [1.3, 2.0]

In Figures 6–6 and 6–7 we show examples of transfer functions for both light quarks and b-quarks, respectively. We fit the shape with a sum of three Gaussians, which works fine. The variable plotted is $1 - E_{jet}/E_{parton}$, since it varies less with
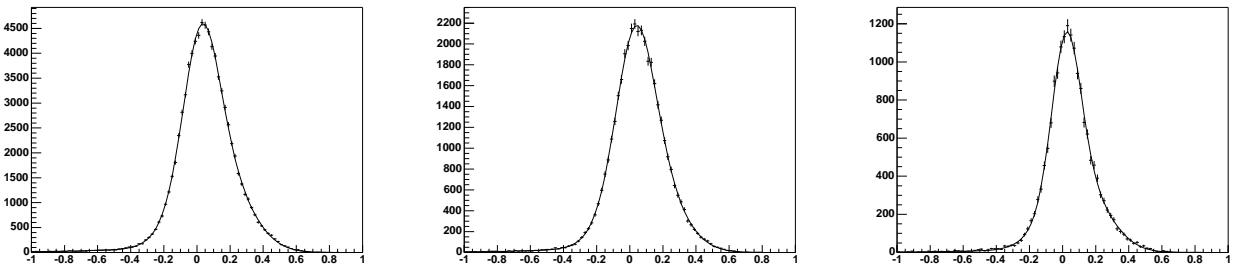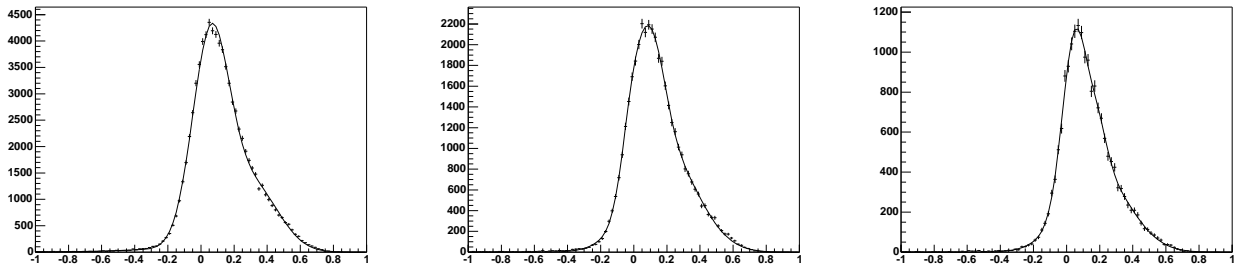
Figure 6–7: b-quarks transfer functions ($x = 1 - \frac{E_{jet}}{E_{parton}}$), binned in three absolute pseudorapidity regions [0, 0.7], [0.7, 1.3] and [1.3, 2.0]

the parton energy. It is related to the distribution we introduced as "transfer function" via a simple change of variable.

Our transfer functions are between parton energy and *corrected* jet energy, as explained in chapter 4.

With these tools in place we ran similar pseudoexperiments on the Herwig sample. The returned m_{top} value was 178.1 ± 0.4 GeV/c^2 and the pulls' width was 1.05 ± 0.09. The correct (generated) mass for this sample is 178 GeV/c^2.

We did not run any other tests because the only change we made in the algorithm at this stage was to plug in realistic transfer functions and run it over fully simulated events. As such, the only new thing that needed testing was the derivation of the realistic transfer functions based on Monte Carlo simulation. This is by far a simpler business than the implementation of matrix elements calculations and change of variables together with the rest of the machinery. Based on the results presented above we concluded that our transfer functions' implementation is fine and the algorithm as a whole works very well, is properly constructed and implemented. Also, our top mass results on Monte Carlo were very similar to those of analyses doing the top mass measurement using matrix elements.

In the next chapter we will show how the top mass matrix element algorithm can be extended to compute the $t\bar{t}$ invariant mass, $M_{t\bar{t}}$.

CHAPTER 7

$M_{t\bar{t}}$ RECONSTRUCTION

7.1   Standard Model $t\bar{t}$ Reconstruction

All the tools developed for the top mass can be turned around to reconstruct any kinematical variable of interest, in particular $M_{t\bar{t}}$. Let's assume for simplicity of presentation that we know which is the right combination, that is, we know how to match jets to partons. In that case

$$P(\{p\}, \{j\}) = \pi_{part}(\{p\}) \cdot T(\{j\}|\{p\}) \tag{7-1}$$

defines the probability that an event has the parton momenta $\{p\}$ and is observed with the jet momenta $\{j\}$. In our notation $\{p\}$ and $\{j\}$ refer to the set of all parton and jet 3-momenta. Integrating on the parton variables, given the observed jets, we obtain the probability used for the top mass measurement. However, the expression provides a weight for any parton configuration once the jets are measured. Any quantity that is a function of parton momenta can be assigned a probability distribution based on the "master" distribution above, $M_{t\bar{t}}$ included, and this is our approach.

Technically this amounts to the following integration:

$$\rho(x|\{j\}) = \int \pi_{part}(\{p\}) \cdot T(\{j\}|\{p\}) \cdot \delta(x - M_{t\bar{t}}(\{p\}))\{dp\} \tag{7-2}$$

with $\rho(x|\{j\})$ being the $M_{t\bar{t}}$ probability distribution given the observed jet momenta. It should be noted that if we remove the delta function we retrieve the event probability formula used for the top mass measurement method presented before, and therefore all the validation tests presented before are as relevant for $M_{t\bar{t}}$ reconstruction. In terms of the modifications in the algorithm these are also

minimal, there is nothing much to be added except histogramming $M_{t\bar{t}}$ during integration. In other words we obtain an invariant mass distribution *per event*. We will use the mean of this $M_{t\bar{t}}$ distribution as our *event* $M_{t\bar{t}}$ value.

Before running on all events in our various samples and producing templates we want to make sure the $M_{t\bar{t}}$ reconstruction algorithm works well. We selected events in which we could match uniquely partons to jets and which contained only four tight jets. These are the circumstances that allow full consistency between the reconstruction algorithm and the events reconstructed and that is a self-consistent test of the method, which is what we intend to show here.
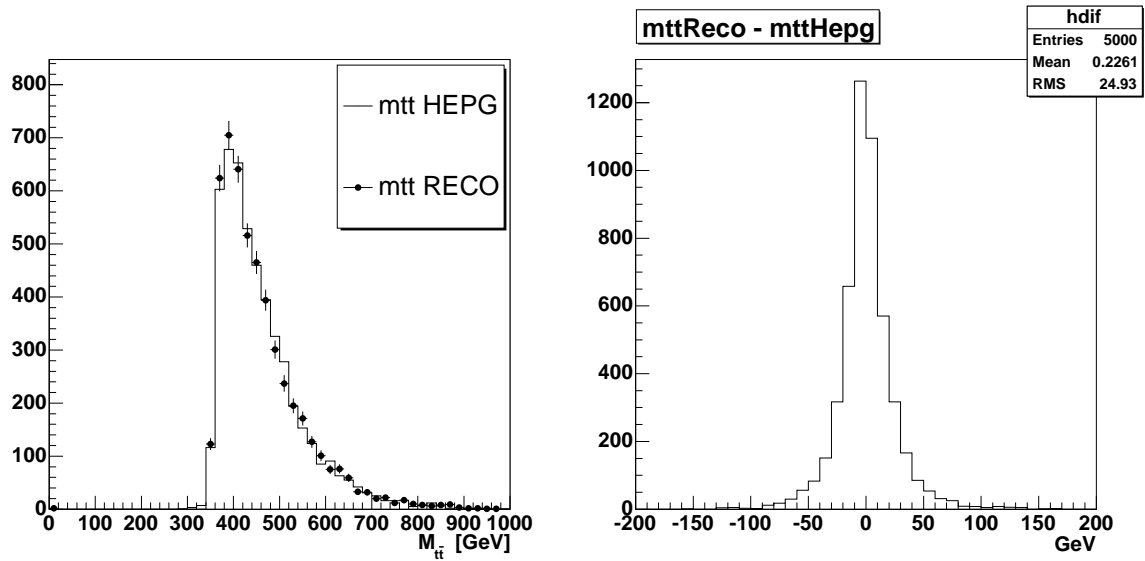
Figure 7–1: $M_{t\bar{t}}$ reconstruction for the correct combination and for events with exactly four matched tight jets.

We ran the algorithm on these selected events and we were able to reconstruct $M_{t\bar{t}}$ back to the parton level as it can be seen in the left plot of Figure 7–1. Both plots are produced after running on events selected from the CDF official Pythia sample.

Since we use the Standard Model $t\bar{t}$ matrix element we do expect to reconstruct these events very well and that seems to be the case indeed, as it is shown also in the right plot of Figure 7–1. There the difference between the

reconstructed value and the true value is histogrammed in order to see the intrinsic resolution and check for any bias. The results are very good and we consider the testing and validation part of the analysis ended.
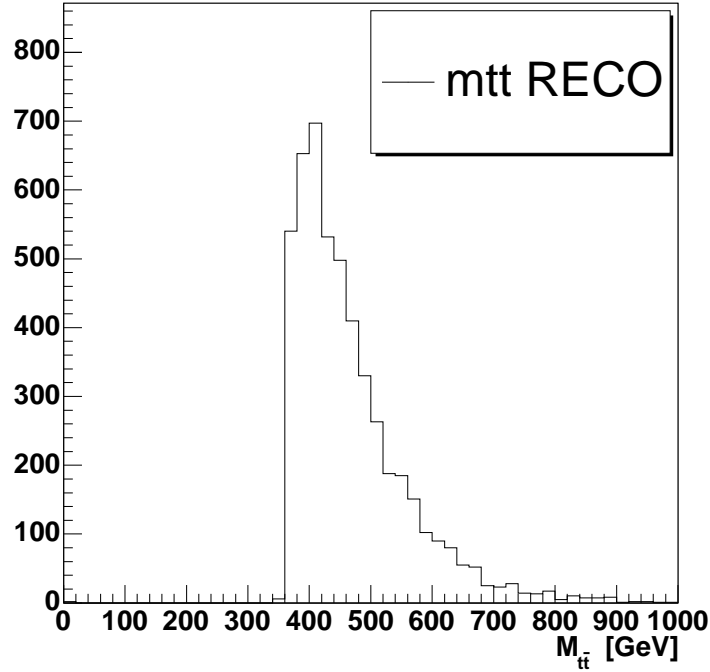
Figure 7–2: $M_{t\bar{t}}$ reconstruction including all events

Since in reality we don't know which is the correct combination we adopt the top mass method approach and sum over all allowed combinations in the formula 7-2. We expect the right combination to contribute more than the others as it happens for the top mass analysis.

The $M_{t\bar{t}}$ as reconstructed for all events, without any of the requirements mentioned above, is shown in Figure 7–2. This is what we expect to be the Standard Model contribution to the $M_{t\bar{t}}$ spectrum in the data.

Some examples of event by event reconstruction are shown in Figure 7–3. The 4th event is a dilepton event and the 8th is a tau+jets event. Interestingly
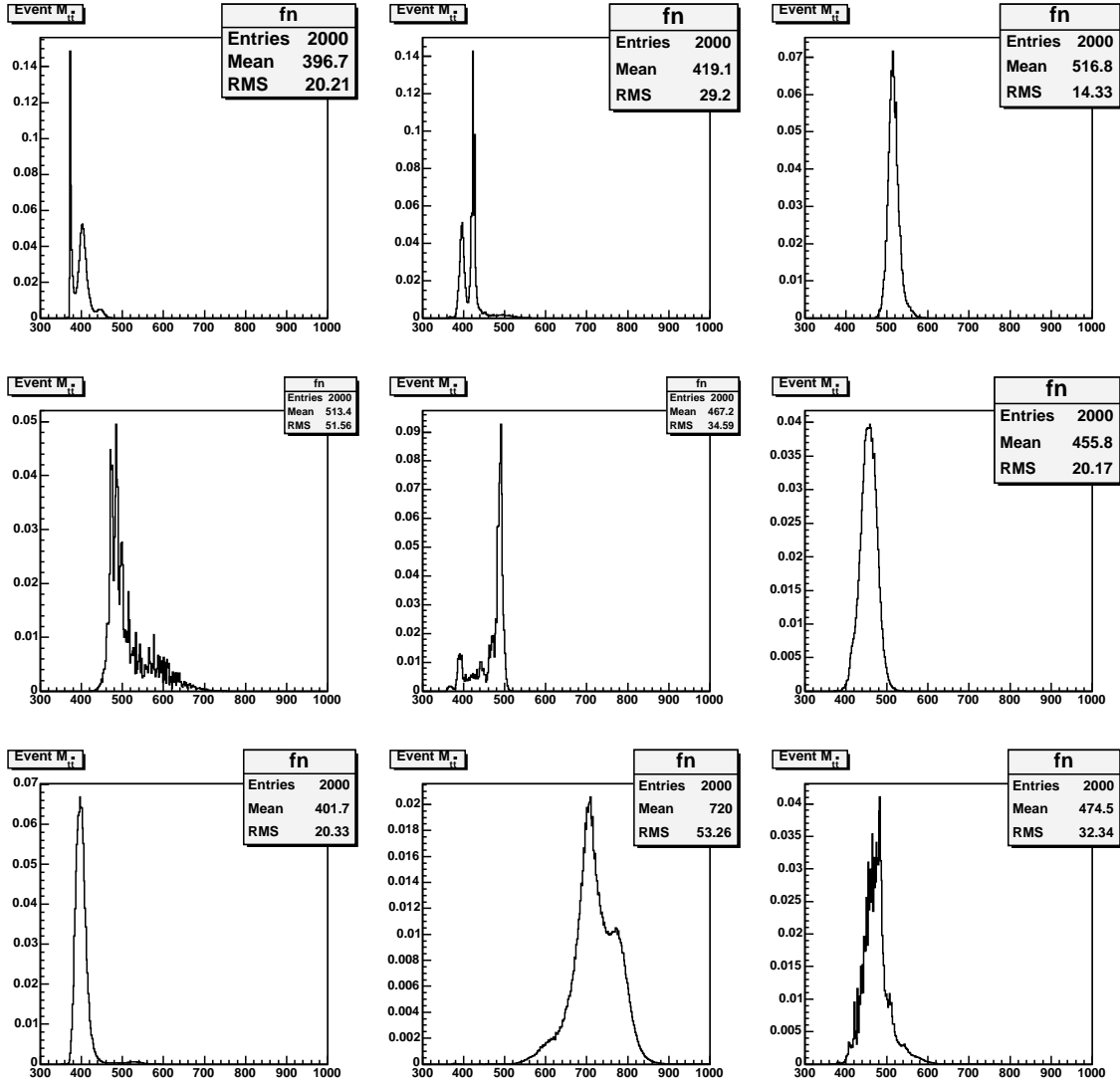
Figure 7–3:   Examples of $M_{t\bar{t}}$ reconstruction, event by event.

they have larger widths than the others which are all lepton+jets events. Adding

combinations together can lead to double or multiple peaks.

The top mass used on data is $m_{top} = 175$ GeV. Therefore this is the value used

in our algorithm when producing $M_{t\bar{t}}$ templates corresponding to various processes.

Figure 7–4 shows the actual template used for fitting the data, derived by fitting

5000 reconstructed events.

Certain approximations were made, since we cannot perform all integrals

which appear in the formal presentation because the CPU time involved would be
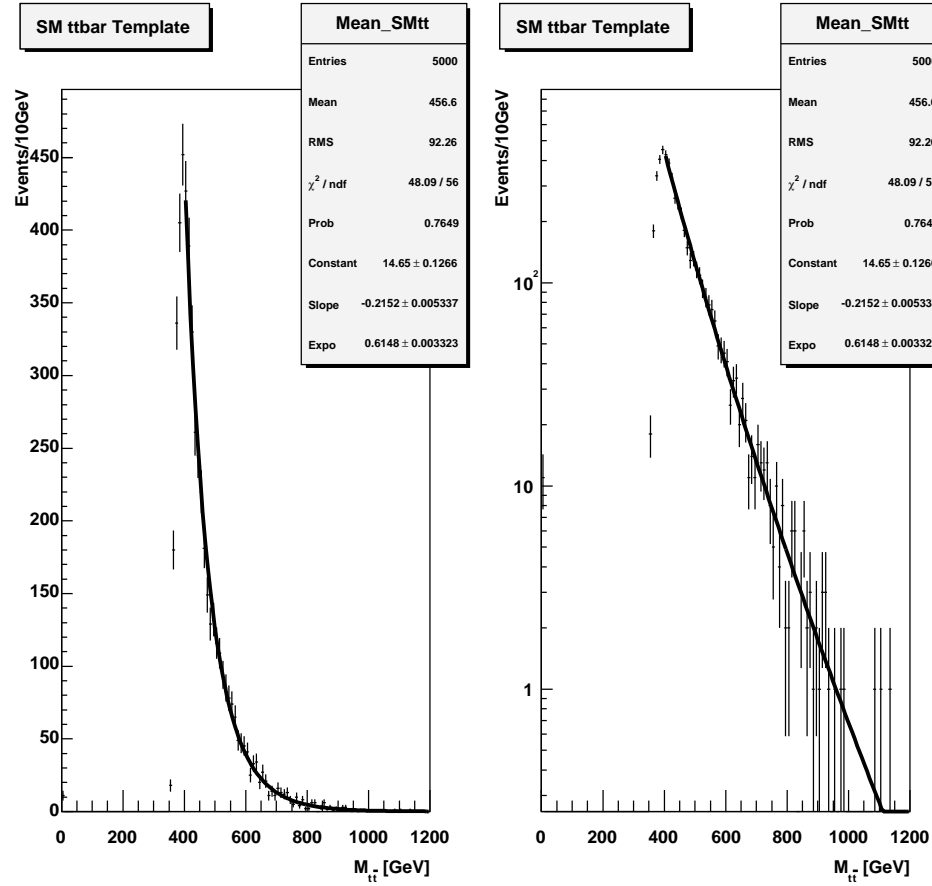
Figure 7–4: $M_{t\bar{t}}$ template for Standard Model $t\bar{t}$ events.

astronomical, even using the computing farms commonly available to CDF users. This is so because we need to model the $M_{t\bar{t}}$ spectrum for 10 signal samples and a couple of backgrounds, and then perform the systematics studies which require recomputing the templates each time.

As it was mentioned in the previous chapter, the implementation uses a different set of variables for integration, namely the masses of the two W bosons, the masses of the two top quarks, the total transverse momentum of the $t\bar{t}$ system and one "W" quark energy. Studies showed that the best approach, given the CPU time limitations, is to set the two top quarks' masses on shell and also set on shell the mass of the W which decays leptonically, leaving us with four integrals to

perform. Even so, for systematics studies we needed about 100,000 CPU hours and we used extensively the CDF computing farms.

7.2 Signal and other SM Backgrounds

The Monte Carlo samples for signal and all other Standard Model backgrounds (besides $t\bar{t}$) are run through the same algorithm, thus producing new distributions corresponding to signal and backgrounds respectively. Even though the signal is not 100% correctly modeled by the Standard Model $t\bar{t}$ matrix element, we expect the reconstruction to work quite well since a significant part of the matrix element is concerned with the top and W decays and that won't depend on the specific $t\bar{t}$ production mechanism. Especially in the case of a spin 1 resonance the differences between the correct resonance matrix element and the Standard Model matrix element are minimal, since the gluon is a spin 1 particle after all. Even tough the methods presented in this dissertation can be applied to more general cases, the actual limits we are deriving at the end are valid for *vector* resonances because the Monte Carlo signal samples were generated with a vector resonance model. We want to remind the reader that it was our initial decision to do a model independent search anyway. The results are not completely model independent only because of the Monte Carlo generators used to produce signal samples.

Applying the reconstruction to non-$t\bar{t}$ events doesn't produce any particularly meaningful distributions, but they are backgrounds needed to model the data.

In what follows we briefly describe the results obtained when running this reconstruction method on the various backgrounds needed in our analysis and presented in a previous chapter.

- **Signal samples**

  We generated signal samples with resonance masses from 450 GeV/c^2 up to 900 GeV/c^2, every 50 GeV/c^2, using Pythia [24]. The reconstructed $M_{t\bar{t}}$ for all is shown in Figure 7–16. The peaks match very well the true value of
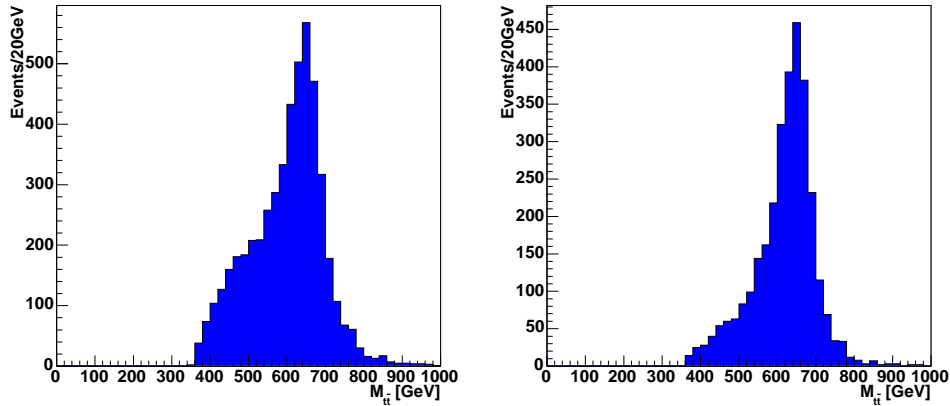
Figure 7–5: Reconstructed invariant mass for a resonance with $M_{X^0} = 650$ GeV. The left plot shows all events passing event selection, while the right plot shows only matched events

the resonance mass. In order to better understand the low mass shoulder we split these events in three orthogonal subsamples: events with all four jets matched to partons, mismatched events and fake lepton+jets events (dilepton or hadronic events passing the lepton+jets event selection). The method is expected to work well on matched events and indeed this is what we see in Figures 7–5 and 7–6. The shoulder is given by the superposition of mismatched events and fake lepton+jets events on top of the nice peak from matched events.

The generated width for the resonance was 1.2% of the resonance mass. As it can be seen the reconstructed resonance mass is much wider, due to the relatively large uncertainties in jet measurements and non measuring the neutrino z component at all. However the peak remains prominent enough to be easily distinguished from the exponentially dropping Standard Model processes.

- **W+jet samples**

We use the CDF official W + 4 partons ALPGEN [26] samples which are then run through Herwig for parton showering. We looked at W + 2b + 2
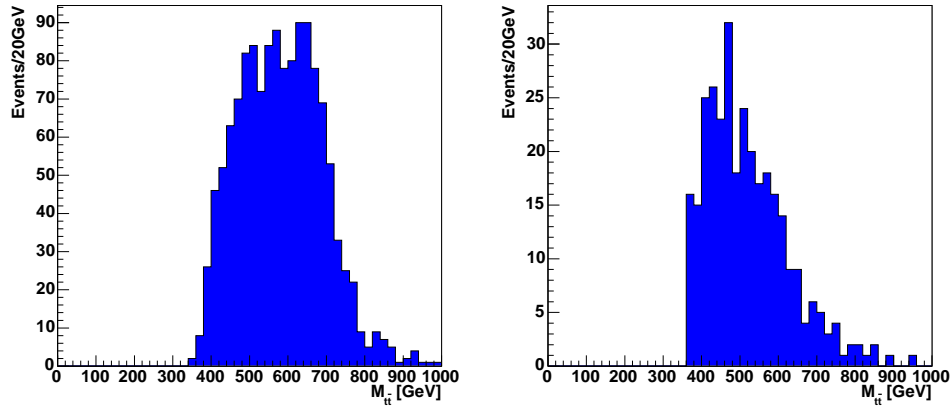
Figure 7–6: Reconstructed invariant mass for a resonance with $M_{X^0} = 650$ GeV. The left plot shows mismatched lepton+jets events and the right plot shows non-lepton+jets events

partons also but decided not to include it explicitly since the shape is very, very similar and the expected contribution at the level of 1-2% compared to 60% or more for the W + 4 partons. These can be seen in Figures 7–7, 7–11, 7–12 and a direct comparison of fit templates is shown in 7–15. So all W+jets events are modeled by the W + 4 partons sample.

- **QCD**

  For QCD we used the data to extract the shape. Multijet data is scanned for jets with high electromagnetic fraction which are reinterpreted as electrons based on the assumption that the jets that do fake an electron are very similar to the ones just mentioned. With that said, the usual event selection is applied and the events are reconstructed just like the others. This process produces the template shown in Figure 7–9. The shape is not much different from W + 4 partons, in fact they are quite close as assumed in the CDF Run 1 analysis when the QCD template was ignored altogether.

- **Dibosons - WW, WZ and ZZ**

  The cross-sections for the WW, WZ and ZZ processes are 12.4 pb, 3.7 pb and 1.4 pb. The acceptances follow the same trend with 0.14%, 0.08% and

0.02% respectively. Moreover, the WZ and ZZ official samples have fewer events left after event selection and the fits have larger errors. Given that WW dominates anyway we decided to use only that template but increase the acceptance such that the expected number of events will cover the small WZ and ZZ contributions. Since overall the whole diboson part is almost negligible this procedure isn't expected to have any impact other than simplifying the analysis. It can be added that the WW template which is shown in Figure 7–10 is also very similar to the Standard Model $t\bar{t}$, W + jets and QCD templates. We put all of them on top of each other for easy comparison in Figure 7–14.

All these templates are used to fit the data and extract limits. The procedure is explained in the next chapter.
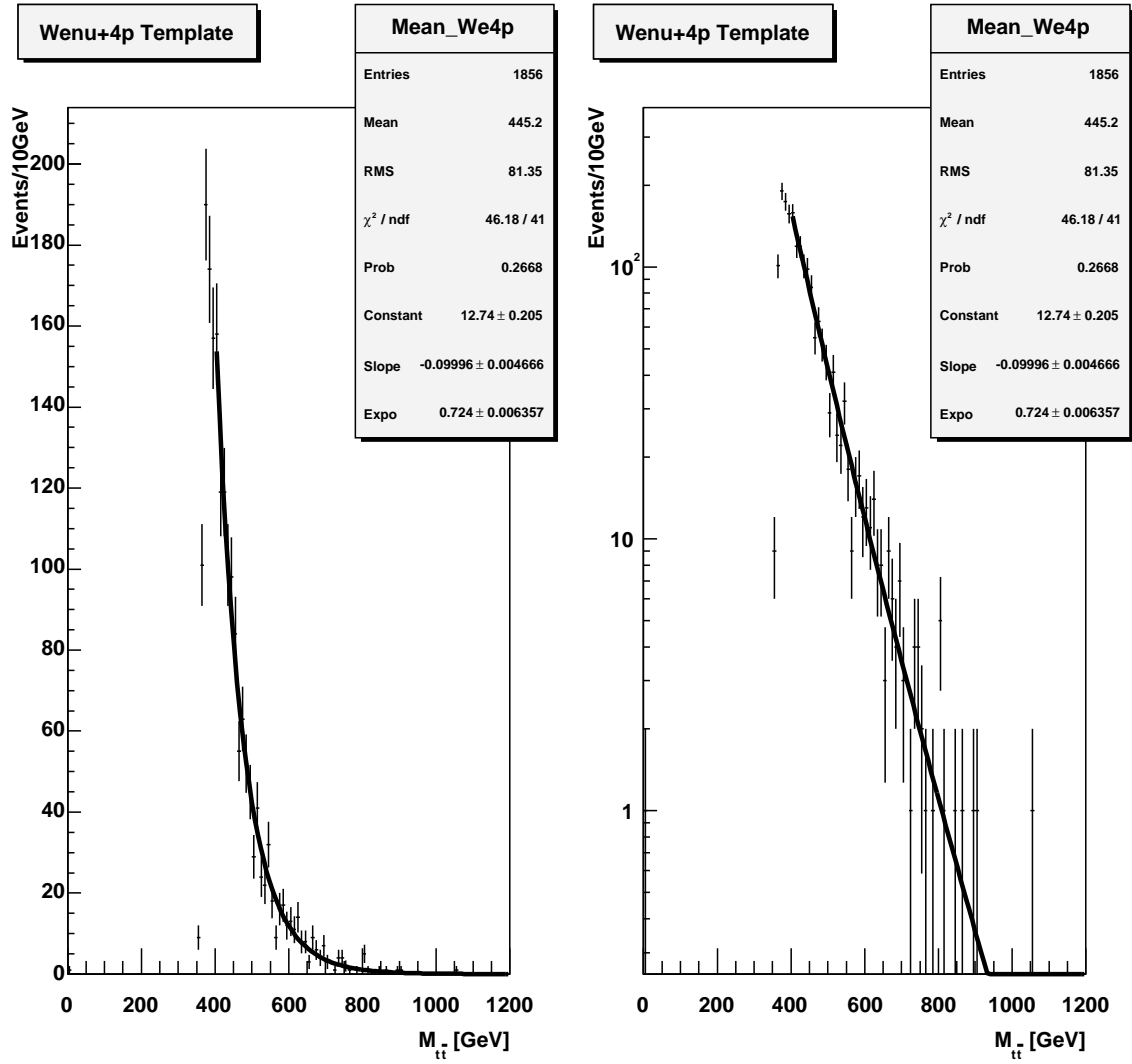
Figure 7–7:   W+4p template (electron sample)
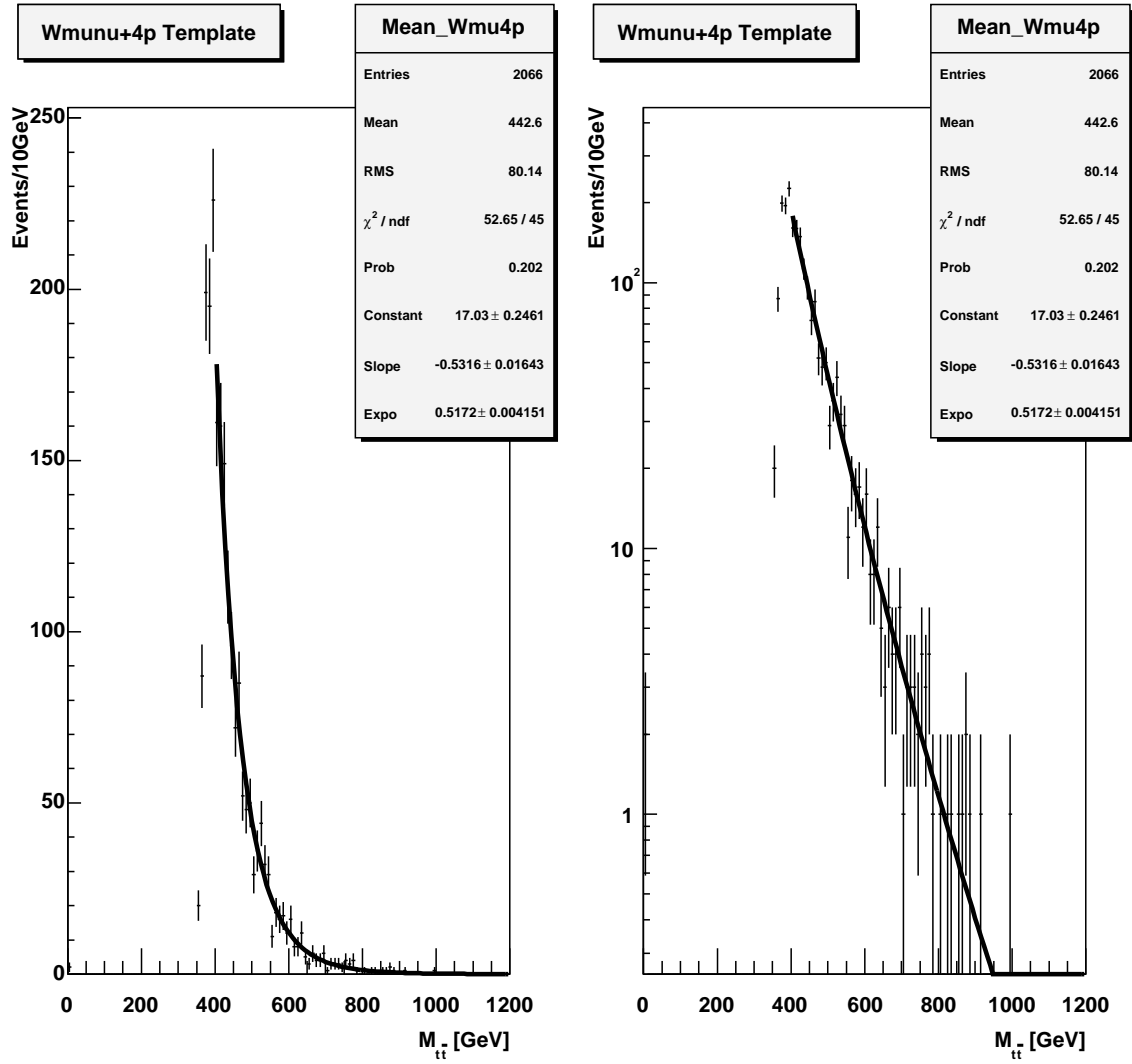
Figure 7–8:   W+4p template (muon sample)
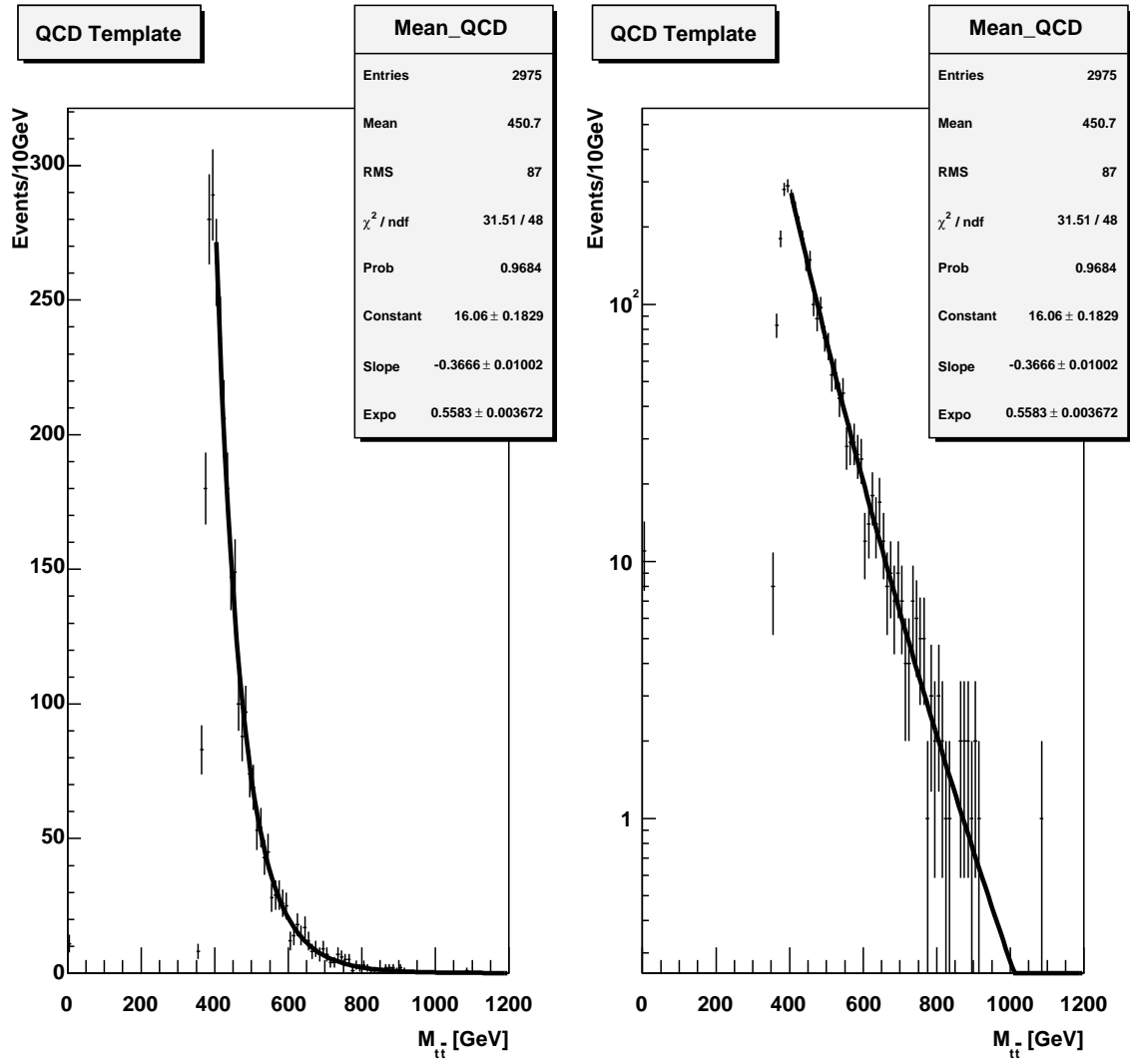
Figure 7–9:   QCD template
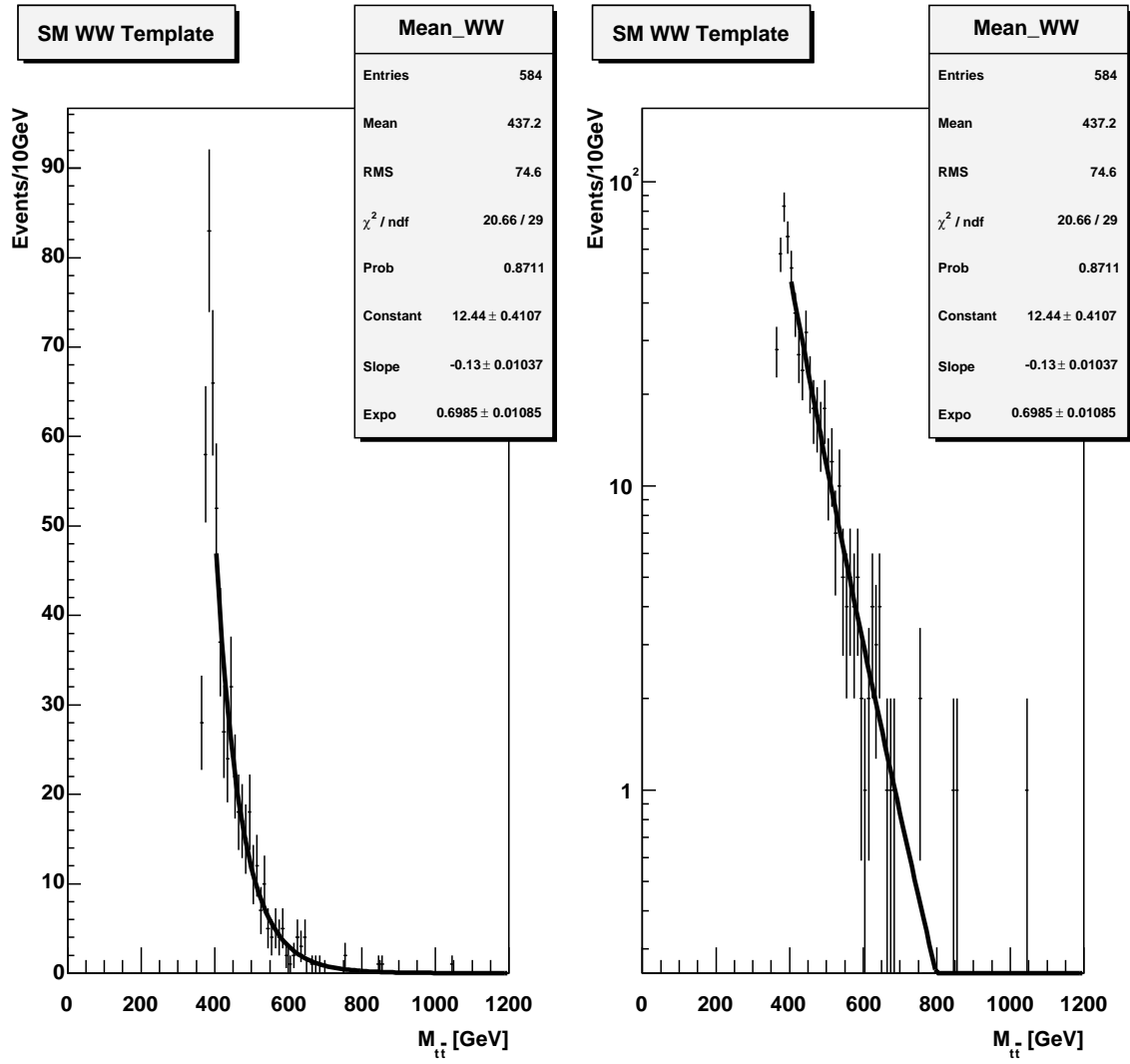
Figure 7–10:   WW template
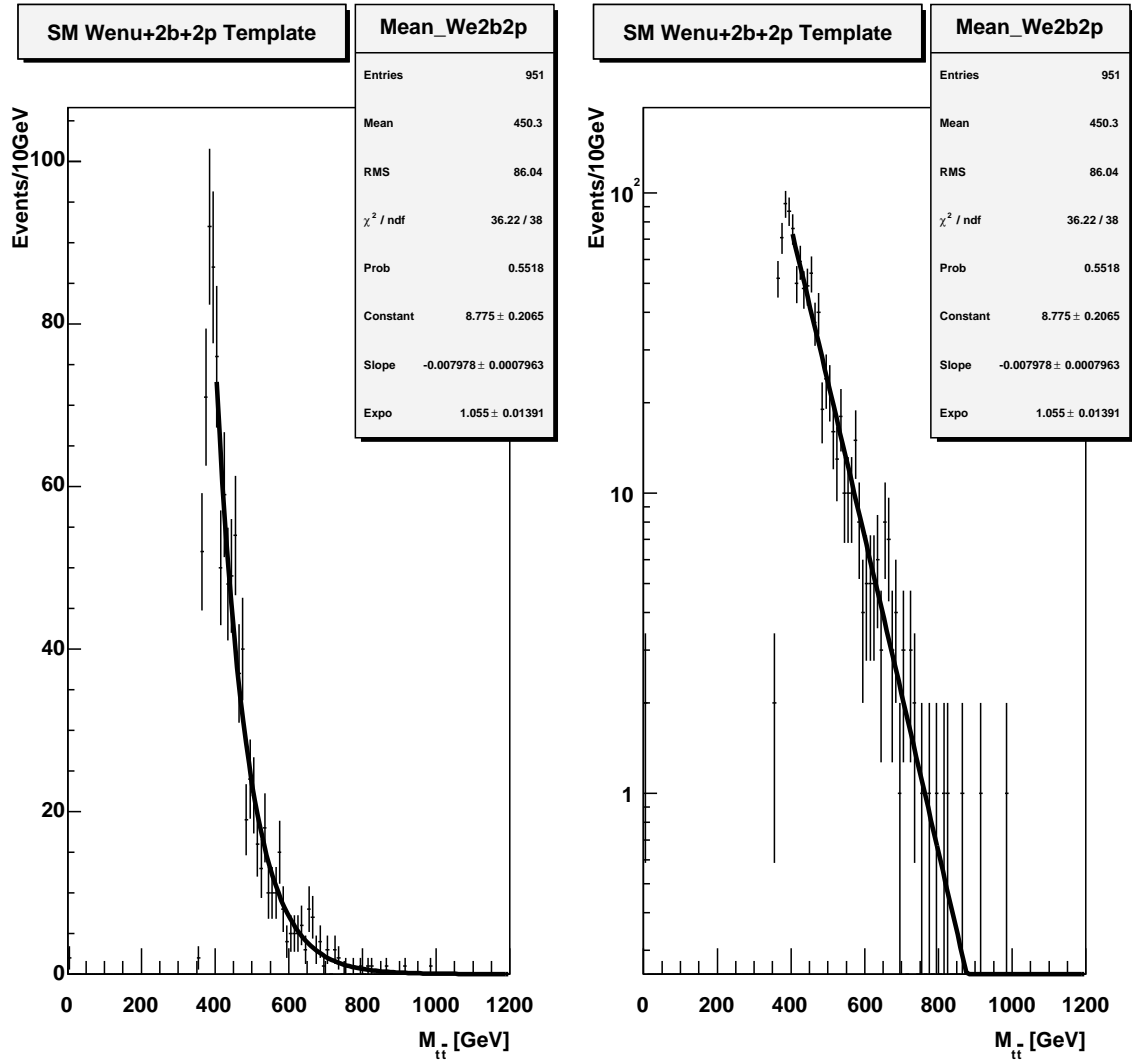
Figure 7–11:   W+2b+2p template (electron sample)
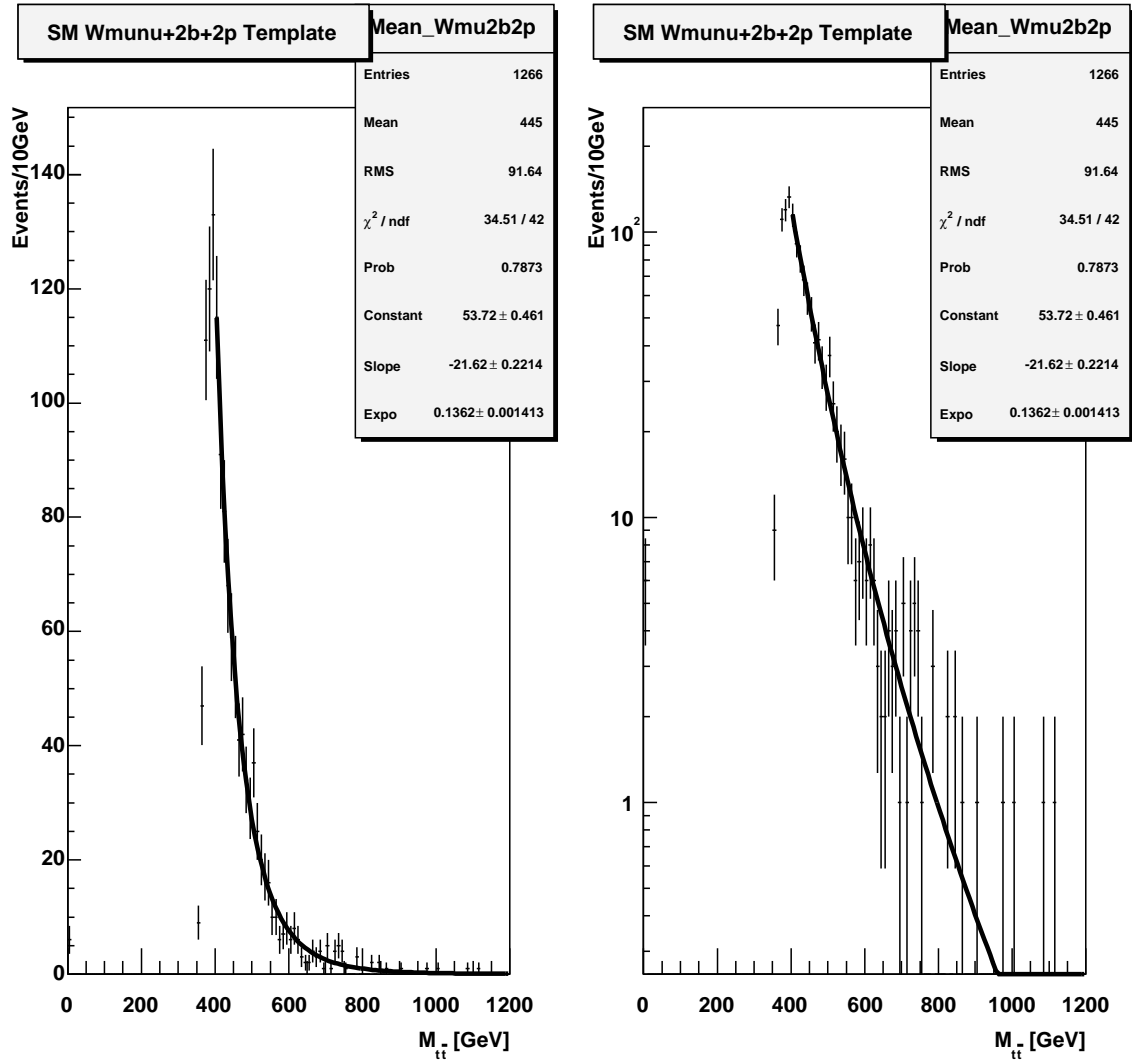
Figure 7–12:   W+2b+2p template (moun sample)

73
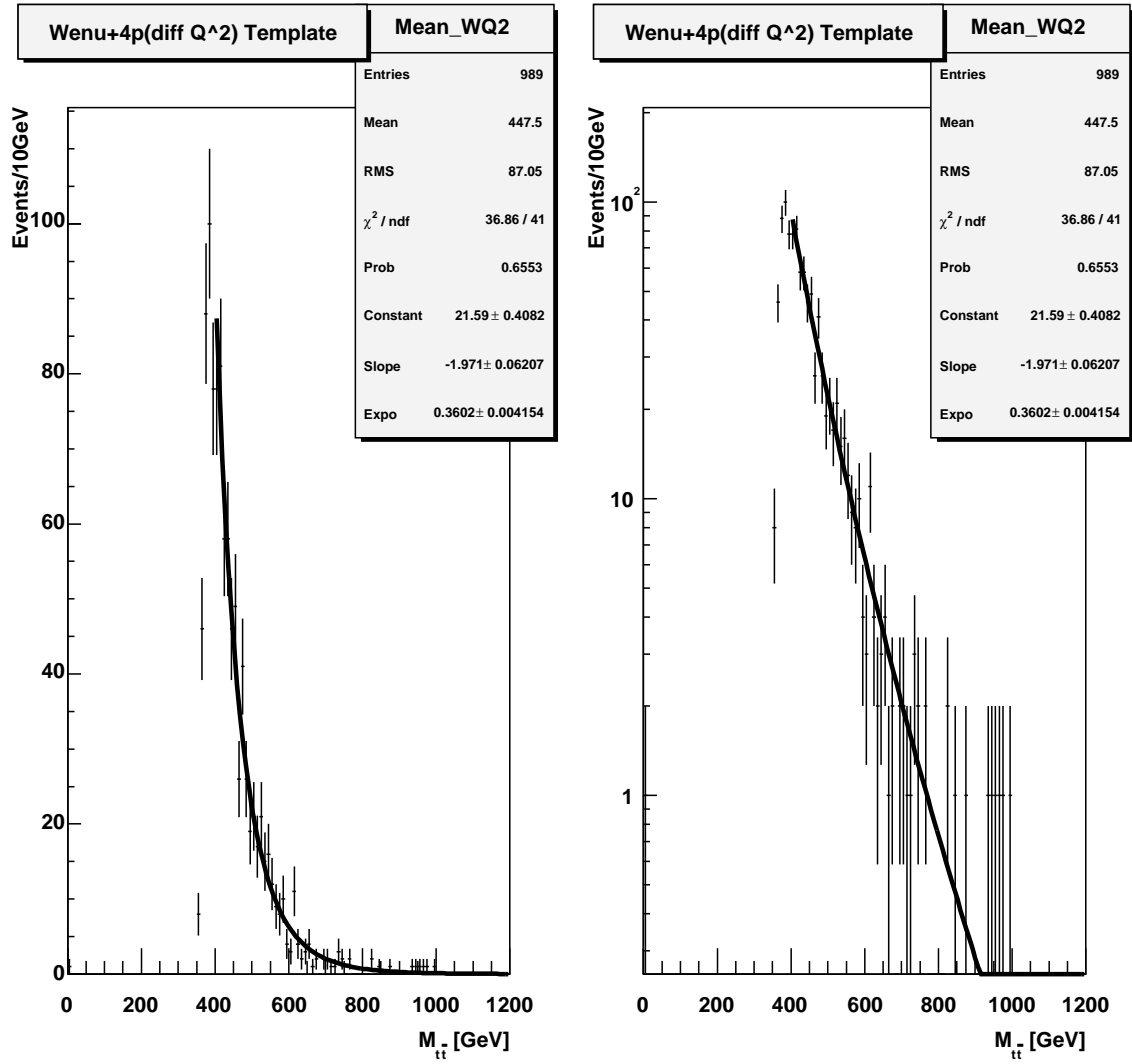
Figure 7–13: W+4p template with alternative Q^2 scale (electron sample)
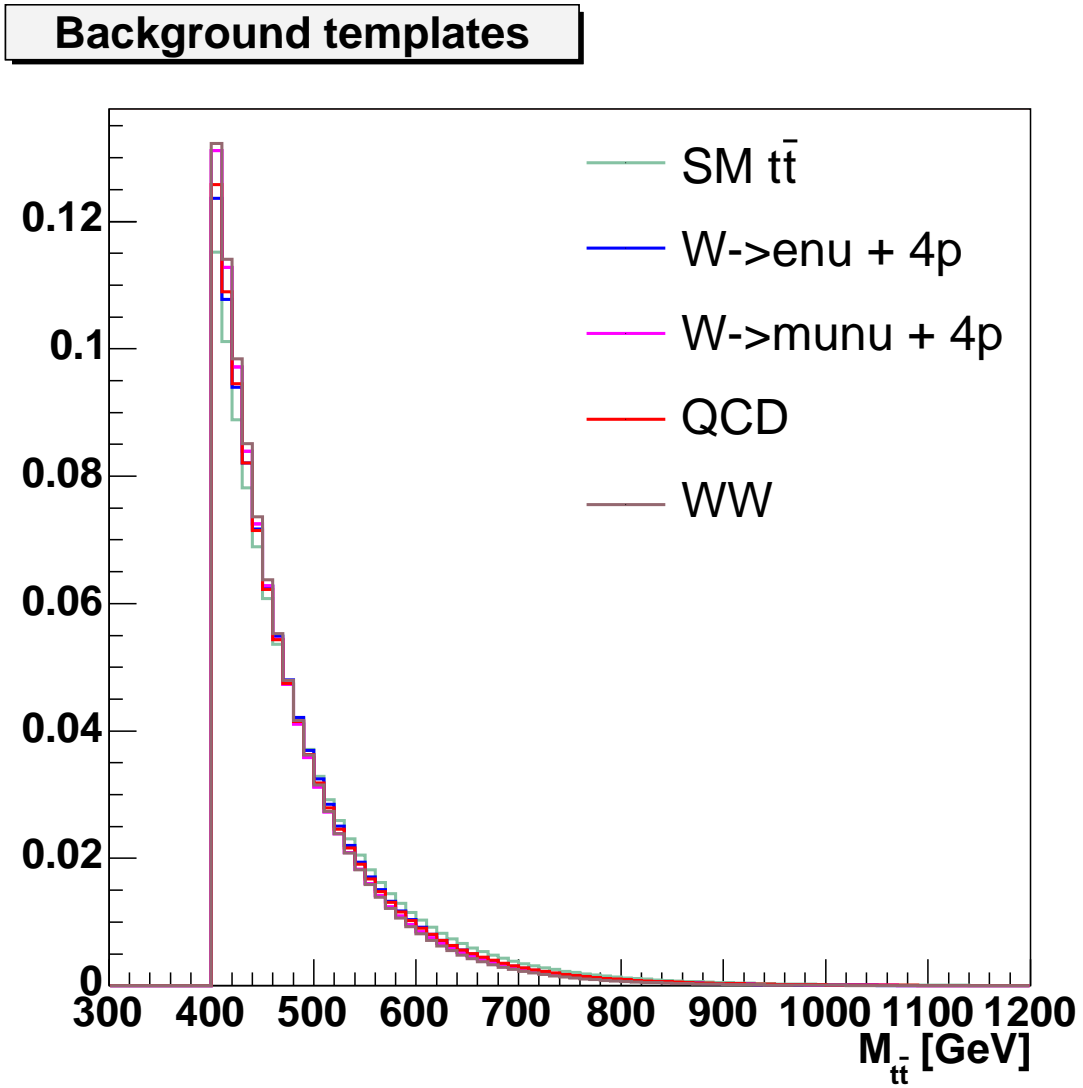
Figure 7–14:   All Standard Model background templates used in the analysis
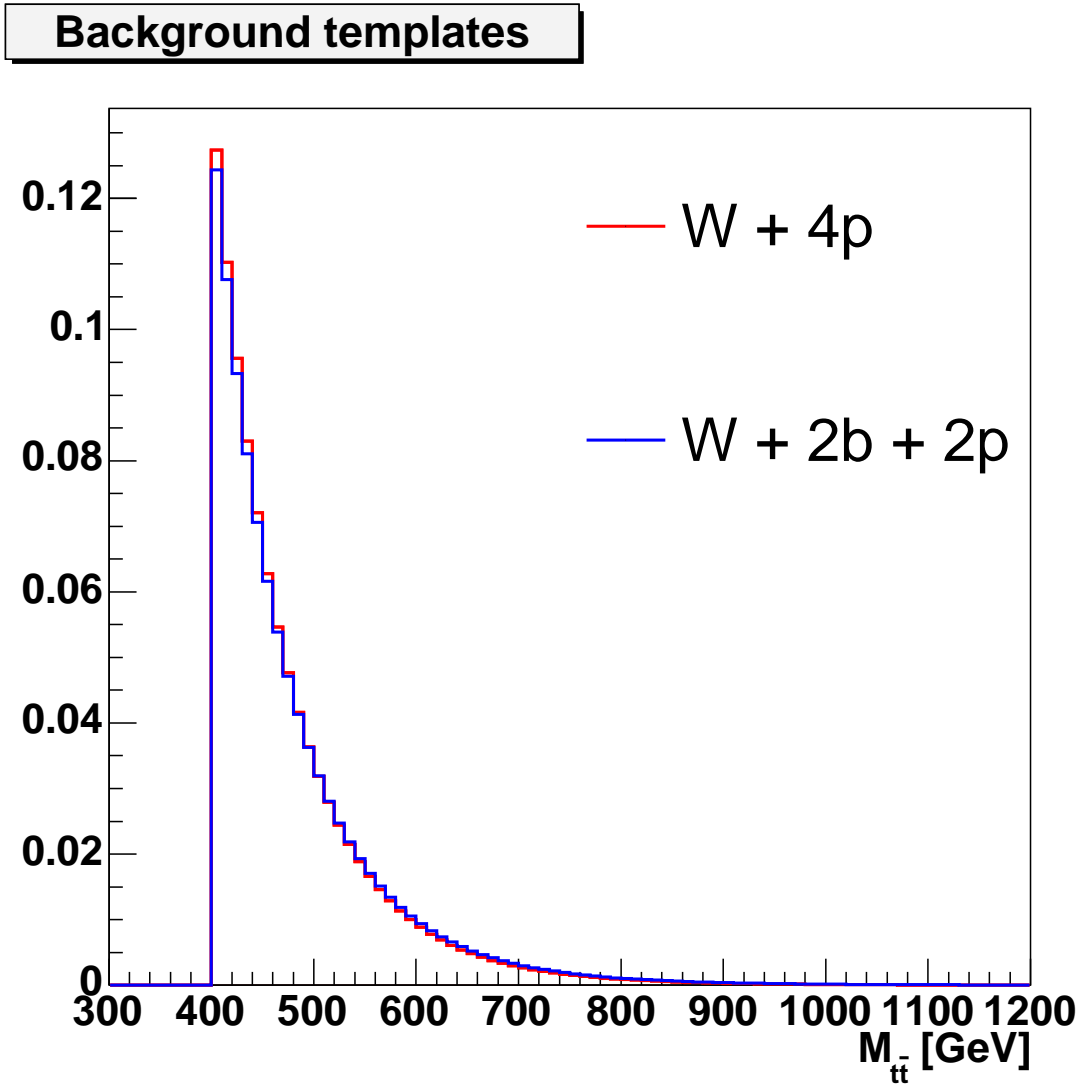
Figure 7–15:   W+2b+2p template vs W+4p template. W+2b+2p was ignored since the expected contribution is at the level of 1-2% and the template is very similar to the W+4p template
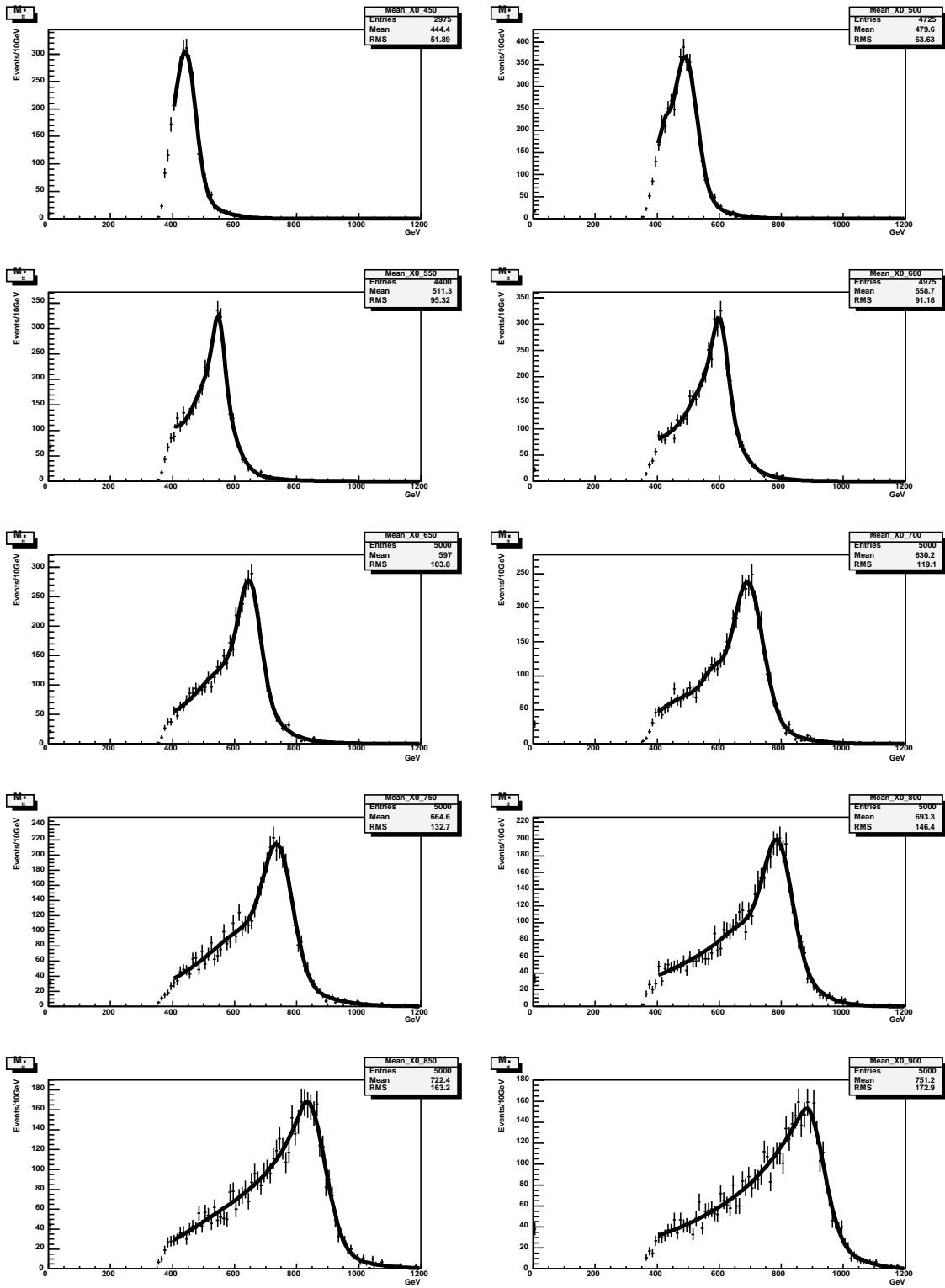
Figure 7–16:   Signal templates

CHAPTER 8
SENSITIVITY STUDIES

In this chapter we will present the algorithm used for establishing lower and upper limits for signal cross-section times branching ratio at any desired confidence level (CL).

We used a Bayesian approach which was shared with other CDF analyses. The main idea and suggestions for the implementation can be found in [27, 28].

8.1   General Presentation of the Limit Setting Methodology

For generality we will assume that the observed data quantities are contained in a vector $\boldsymbol{n} = (n_1, n_2, \ldots, n_{nbins})$, which in our case would correspond to the bin content of the $M_{t\bar{t}}$ histogram. The modeling of the data contains one unknown parameter and we want to be able to make a probabilistic statement about that parameter once we look at the data. In other words we would like to obtain a *posterior* probability distribution for the parameter. We will call this parameter σ, because in our particular case it corresponds to the signal cross-section times branching ratio.

It is often the case that other parameters are involved, and their values are known with some uncertainty. We will assume their values are normally distributed with the uncertainty being the standard deviation. We will denote these parameters $\boldsymbol{\nu} = (\nu_1, \nu_2, \ldots)$ and call them *nuisance parameters*.

We will formalize our prior knowledge of the nuisance parameters and σ by introducing the prior probability density $\pi(\sigma, \boldsymbol{\nu})$. In our case this can be factorized as a product of Gaussians for the nuisance parameters and a flat distribution for σ.

The Bayes theorem connects the likelihood of the measurement (prior probability) to the posterior density of σ and $\boldsymbol{\nu}$ *after* the measurement:

$$p(\sigma, \boldsymbol{\nu}|\boldsymbol{n}) = \mathcal{L}(\boldsymbol{n}|\sigma, \boldsymbol{\nu})\pi(\sigma, \boldsymbol{\nu})/p(\boldsymbol{n}) \qquad (8\text{-}1)$$

where $p(\boldsymbol{n})$ is the marginal probability density of the data

$$p(\boldsymbol{n}) = \int d\boldsymbol{\nu} \int d\sigma \mathcal{L}(\boldsymbol{n}|\sigma, \boldsymbol{\nu})\pi(\sigma, \boldsymbol{\nu}) \qquad (8\text{-}2)$$

In these equations $p(\sigma, \boldsymbol{\nu}|\boldsymbol{n})$ stands for the posterior density and $\mathcal{L}(\boldsymbol{n}|\sigma, \boldsymbol{\nu})$ stands for the prior density.

We are not interested in the nuisance parameters so we integrate over them

$$p(\sigma|\boldsymbol{n}) = \int d\boldsymbol{\nu} \, p(\sigma, \boldsymbol{\nu}|\boldsymbol{n}) \qquad (8\text{-}3)$$

to obtain the sought posterior probability density for the parameter of interest σ.

From this posterior $p(\sigma|\boldsymbol{n})$ we can extract the information we need, like the most probable value, upper and lower limits at any confidence level, etc.

8.2 Application to This Analysis

In our analysis the data $\boldsymbol{n}$ we observe is the binned $M_{t\bar{t}}$ spectrum, the parameter of interest σ is the resonant $t\bar{t}$ production cross section times branching ratio, $\sigma_{X^0} \cdot BR(X^0 \rightarrow t\bar{t})$, and the nuisance parameters are: the integrated luminosity, acceptances, and cross-sections.

In order to build the likelihood (prior density) we need normalized $M_{t\bar{t}}$ templates for each process.

We will use the notation T_j with $j \in \{s, \boldsymbol{b}\}$ for the binned signal and background templates, and T_{ji} for the ith bin of the jth template.

Given the above definitions we can write the *expected* number of events in the ith bin of the spectrum as

$$\mu_i = \int L dt \cdot \sum_{j \in \{s, \boldsymbol{b}\}} \sigma_j \epsilon_j T_{ji} = \sigma_s A_s T_{si} + \sum_{j \in \{\boldsymbol{b}\}} N_j T_{ji} \tag{8-4}$$

where we separated the signal contribution from the backgrounds and we defined the auxiliary variables $A_s = \int L dt \cdot \epsilon_s$ (also called *effective acceptance*) and $N_j = \int L dt \cdot \sigma_j \epsilon_j$ with $j \in \{\boldsymbol{b}\}$, the total expected number of events for each background, after event selection.

The prior likelihood can be written:

$$\mathcal{L}(\boldsymbol{n}|\sigma, \boldsymbol{\nu}) = \prod_{i \in \{nbins\}} \mathcal{P}(n_i|\mu_i) = \prod_{i \in \{nbins\}} \frac{(\sigma_s A_s T_{si} + \sum N b_j T_{ji})^{n_i}}{n_i!} e^{-\sigma_s A_s T_{si} - \sum N b_j T_{ji}}$$

$$\tag{8-5}$$

As we already pointed out, we may not know exactly A_s and the expected number of events from background. It is customary to take as priors for these parameters a truncated (to positive values) Gaussian to represent our prior knowledge[1] . For the signal cross section σ_s we use a flat prior.

8.2.1 Templates

As pointed out in Eq. 8-5, in order to build the likelihood function we need to know the template distributions for the signal and for the backgrounds.

Given the limited statistics available for the samples we decided to fit them and use the smoothed fit distributions as templates; this procedure removes unphysical empty bins or bumps.

As already mention in Chapter 5, we consider as possible background contributions the following processes:

---

[1] Given that the total efficiency is often the product of several efficiencies, the log-normal prior is often used too.

- Standard Model $t\bar{t}$

- $W \rightarrow e\bar{\nu} + 4$ partons

- $W \rightarrow \mu\bar{\nu} + 4$ partons

- $W \rightarrow e\bar{\nu} + 2$ partons $+ 2\ b$

- $W \rightarrow \mu\bar{\nu} + 2$ partons $+ 2\ b$

- Dibosons - WW, WZ, ZZ

- QCD (from data)

Mean X0_600	
χ^2 / ndf	45.17 / 43
Prob	0.3815
Constant1	137.7 ± 20.5
Mean1	603.9 ± 2.4
Sigma1	22.85 ± 2.97
Constant2	132.4 ± 19.5
Mean2	577.9 ± 5.6
Sigma2	57.79 ± 6.44
Constant3	86.6 ± 11.0
Mean3	465.7 ± 32.9
Sigma3	143.4 ± 15.4

Mean SMtt	
χ^2 / ndf	48.09 / 56
Prob	0.7649
Constant	14.65 ± 0.13
Slope	-0.2152 ± 0.0053
Expo	0.6148 ± 0.0033
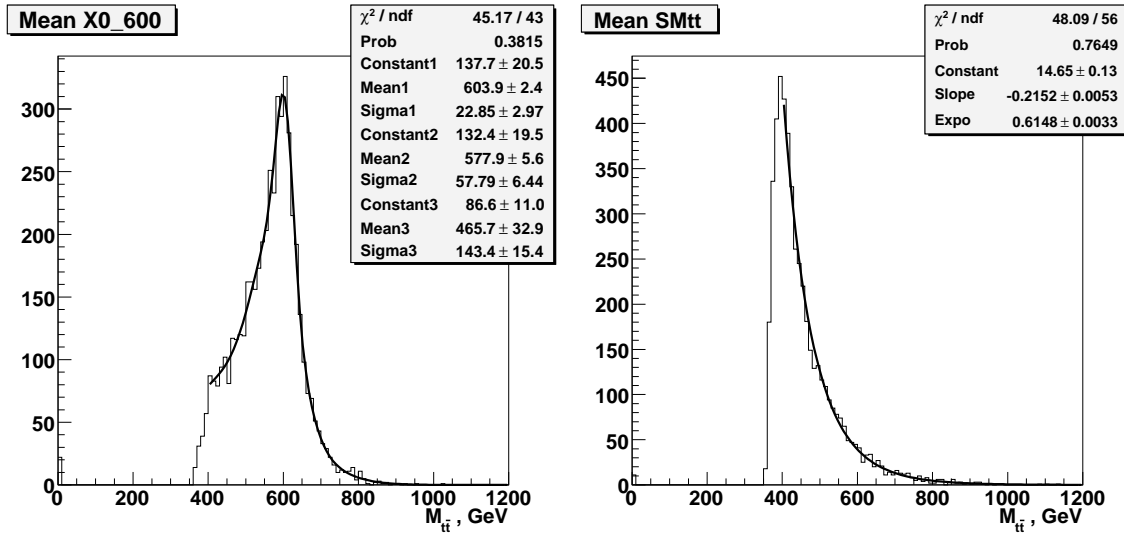
Figure 8–1: Signal and background examples. The signal spectrum on the left ($M_{X_0} = 600\ GeV/c^2$) has been fit with a triple Gaussian. The background spectrum from Standard Model $t\bar{t}$ has been fit with the exponential-like function. Fit range starts at $400 GeV/c^2$.

The $M_{t\bar{t}}$ histograms are fit with an exponential-like function $f(x) = \alpha \cdot e^{\beta \cdot x^\gamma}$ in the region above $400\ GeV/c^2$. The signal histogram is fit with a double or triple Gaussian, or a truncated double Gaussian and a truncated exponential distribution[2] . An example is shown in Fig 8–1. All templates can be found at the end of the previous chapter.

---

[2] This set of the fitting functions guarantees a fit with good χ^2 probability.

We discussed the backgrounds in Chapter 5, and we will remind the reader that we decided it is safe to absorb the small $W + 2$ partons $+ 2\ b$ contributions into the $W + 4$ partons templates. Similarly, the WZ and ZZ contributions are absorbed in the ZZ template by increasing by 20% the nominal WW cross section.

8.2.2   Template Weighting

Equation 8-4 shows that in order to build the likelihood we need to know the number of background events N_j for each background type.

Table 8–1: Acceptances for background samples.

Sample	Event Selection	Reconstruction and $400 GeV/c^2$ cut	Total acceptance
SM $t\bar{t}$	0.045	0.72	0.032
WW	0.0014	0.60	0.0008
W($e\nu$)	0.0076	0.66	0.0050
W($e\mu$)	0.0072	0.65	0.0047
QCD	0.0070	0.71	0.0050

In general we estimate the cross-section, acceptance and integrated luminosity in order to get this number, but since the cross sections for the processes $p\bar{p} \rightarrow W + nj$ and multijets (QCD) are not known with good precision we decided to estimate the number of events from these backgrounds based on the total number of events seen in the data:

$$N_{CDF}^{TOT} = \int \mathcal{L}dt \cdot (\sigma_s A_s + \sigma_{t\bar{t}} A_{t\bar{t}} + \sigma_{WW} A_{WW}) + N_{We4p} + N_{W\mu 4p} + N_{QCD} \quad (8\text{-}6)$$

with the constraints

$$N_{We4p}/A_{We4p} = N_{W\mu 4p}/A_{W\mu 4p}, \quad N_{Wl4p} = 10 \cdot N_{QCD} \quad (8\text{-}7)$$

The relative weights for $We4p$, $W\mu 4p$ backgrounds have been set such that they have the same number of events before the event selection and reconstruction because the (unknown) cross sections are considered to be the same.

The relative weight between QCD and $W+4p$ has been set to 10% as discussed in Chapter 5 and established in this analysis [29].

Acceptances used in calculations are listed in Tables 8–1 and 8–2. Cross-sections are listed in section 5.4, Table 5–3.

Table 8–2:   Acceptances for resonance samples.

M_{X^0} (GeV/c^2)	Event Selection	Reconstruction and 400 GeV/c^2 cut	Total
450	0.047	0.86	0.040
500	0.051	0.93	0.048
550	0.055	0.94	0.051
600	0.057	0.97	0.055
650	0.059	0.97	0.057
700	0.062	0.97	0.060
750	0.062	0.98	0.060
800	0.063	0.98	0.061
850	0.063	0.97	0.061
900	0.061	0.98	0.059

8.2.3   Implementation

After building the likelihood for a given observation $\boldsymbol{n}$ according to Eq. 8-5 we need to calculate the posterior density for σ_s according to Equations 8-1, 8-2 and 8-3. In practice we do not divide by $p(\boldsymbol{n})$ in Eq. 8-1 since that is only a global normalization factor we can apply at the end. In this way we do not need Eq. 8-2 any more and we can rewrite Eq. 8-1 in a simplified and more explicit form:

$$p(\sigma_s; A_s, N_{\boldsymbol{b}} | \boldsymbol{n}) = \mathcal{L}(\boldsymbol{n} | \sigma_s; A_s, N_{\boldsymbol{b}}) \, \pi(\sigma_s; A_s, N_{\boldsymbol{b}}) \tag{8-8}$$

To obtain the posterior probability density for σ_s only we carry out the integration on the nuisance parameters A_s and $N_{\boldsymbol{b}}$ using a Monte Carlo method.

Following the suggestions in [28] on page 20, we implement the "Sample & Scan" method. We repeatedly (1000 times) sample the priors $\pi(A_s)$ and $\pi_j(N_j)$, which are truncated Gaussians with respective widths of δA_s and δN_j. Then we scan (400 bins) the σ_s up to some value where the posterior is negligible. At each

scan point we add to the corresponding bin in a histogram of σ_s a weight equal to $\mathcal{L}(\boldsymbol{n}|\sigma_s, A_s, N_b) \cdot \pi(\sigma_s, A_s, N_b)$. This yields the posterior density for σ_s.

8.2.4   Cross Section Measurement and Limits Calculation

Having calculated the signal cross section posterior density we can extract limits and "measure" the cross section. We define as our estimator for the cross section and therefore as our measurement the most probable value of the distribution. This choice is supported by many linearity tests we run both with fake signal templates (simple Gaussians) and with real X_0 templates.
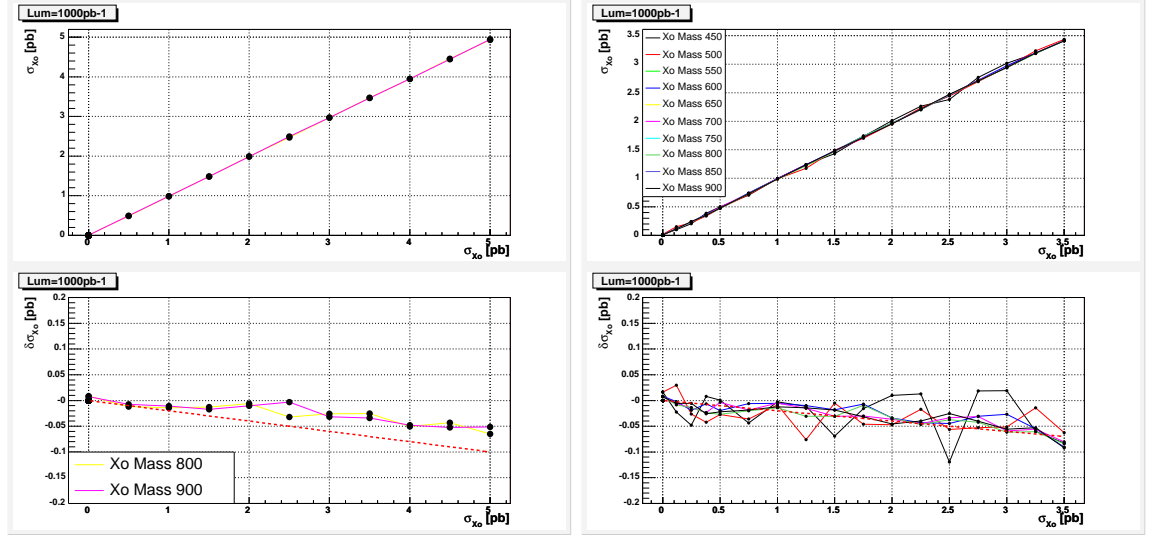
Figure 8–2: Linearity tests on fake (left) and real (right) templates. As test fake signal templates we used Gaussians with 60 GeV/c^2 widths and means of 800 and 900 GeV/c^2. We used also real templates with masses from 450 to 900 GeV/c^2. The top plots show the input versus the reconstructed cross section after 1000 pseudoexperiments at integrated luminosity $\int \mathcal{L} = 1000\, pb^{-1}$. Bottom plots show the deviation from linearity in expanded scale, with red-dotted lines representing a 2% deviation

Figure 8–2 shows the results of the tests with fake Gaussian signal templates of 800 and 900 GeV/c^2 masses and 60 GeV/c^2 width and with real $M_{t\bar{t}}$ templates for X_0 masses from 450 to 900 GeV/c^2 at an integrated luminosity equal to

$\int \mathcal{L} = 1000pb^{-1}$. The reconstructed cross section agrees very well with the input value, showing only a small relative shift of about 2%.

However our measurement is meaningless as long as it is consistent with the null hypothesis, being only a statistical fluctuation. Therefore the key quantities to extract are the upper and lower limits (UL, LL) on the cross-section at a given confidence level. This is done by finding an interval defined by limits LL and UL, which satisfy:

$$\frac{\int_{LL}^{UL} p(\sigma|\boldsymbol{n})}{\int_0^\infty p(\sigma|\boldsymbol{n})} = \alpha \tag{8-9}$$

and

$$p(LL|\boldsymbol{n}) = p(UL|\boldsymbol{n}) \tag{8-10}$$

with α the desired confidence level, for example 0.95 for 95%.
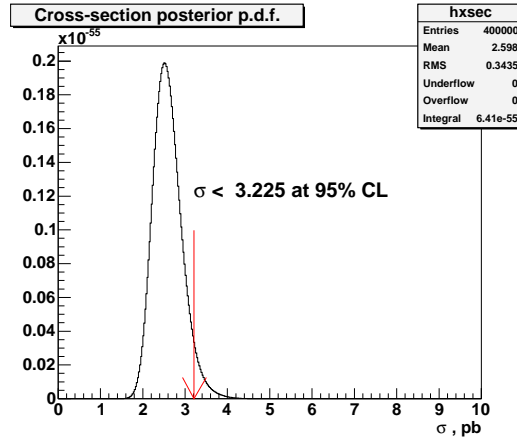
Figure 8–3: Example posterior probability function for the signal cross section for a pseudoexperiment with input signal of 2 pb and resonance mass of 900 GeV/c^2. The most probable value estimates the cross section, and 95% confidence level (CL) upper and lower limits are extracted. The red arrow and the quoted value correspond to the 95% CL upper limit

In this way we can extract LL and UL for each pseudoexperiment or for data. Figure 8–3 shows an example of posterior for a pseudoexperiment with input signal of $2\,pb$, $M_{X^0} = 900\,GeV/c^2$ and total integrated luminosity $\int \mathcal{L} = 1000\,pb^{-1}$.

Before looking at the data we need to know what are the expected limits without any signal present and what are their fluctuations for certain integrated luminosities.

For these purposes we ran many (1000) pseudoexperiments for each M_{X^0} and integrated luminosity and we filled histograms with the most likely value, LL and UL from each pseudoexperiment.

The median of the UL histogram is considered the expected upper limit in the absence of any signal. We also define 68% and 95% CL intervals around the central value in order to get a feeling of the expected fluctuations in the upper limits.

We also ran similar series of pseudoexperiments *with* signal in order to see what are our chances of observing a non-zero LL in a given scenario. More specifically, we computed the probability of observing a non-zero LL for a given resonance mass, integrated luminosity and signal cross-section. This quantity is very useful in assessing the power of the algorithm and what signal cross-sections are realistically possible to observe at any integrated luminosity.

8.2.5   Expected Sensitivity and Discovery Potential

Figure 8–4 shows the distribution of the expected upper limit (UL) at 95% CL for various masses and two integrated luminosity scenarios, $\int \mathcal{L} = 319, 1000 \, pb^{-1}$.

Figure 8–5 shows the power of the algorithm in distinguishing signal from background. On the x axis we have input signal cross-section and on the y axis the fraction is the probability of observing a non-zero LL at 95% CL for $\int \mathcal{L} = 1000 \, pb^{-1}$.

This plots do not include shape systematics, or systematic effects that lead to change in the shape of the templates. We will explore the treatment of shape systematics in the next chapter.
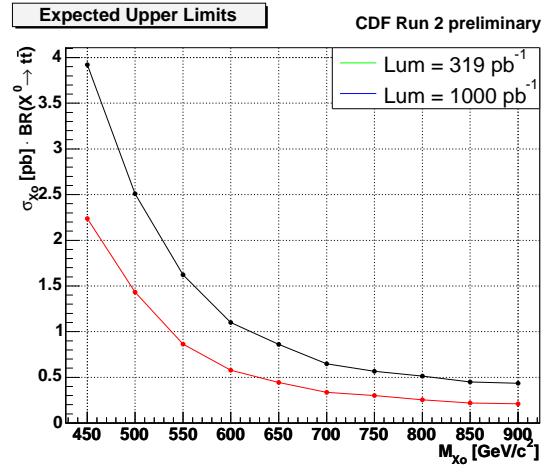
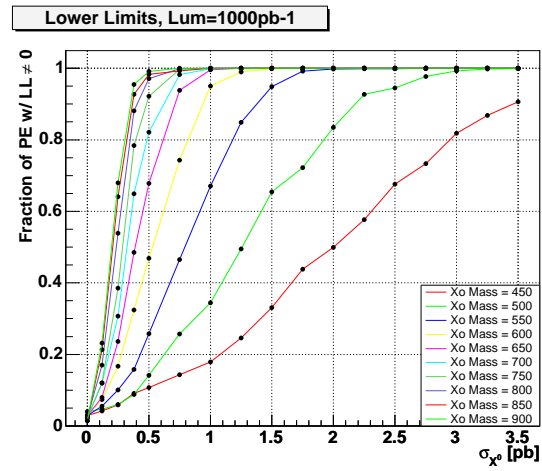Figure 8–4: Upper limits at 95% CL. Only acceptance systematics are considered in this plot.

Figure 8–5: Probability of observing a non-zero lower limit versus input signal cross section at $\int \mathcal{L} = 1000 \, pb^{-1}$. Only acceptance systematics are included in this plot

CHAPTER 9
SYSTEMATICS

We distinguish between two kinds of systematic uncertainties, acceptance and cross-section systematics, and shape systematics. The first one does not affect the shape of the templates and it is implicitly accounted for by the uncertainties in the nuisance parameters.

Shape systematic uncertainties not only affect the acceptances but also the template shapes, therefore they must be handled in a different way.

9.1   Shape Systematics

A change on Jet Energy Scale, initial and final state radiation, parton distribution function, etc., modifies the signal and backgrounds acceptances as well as their templates. To incorporate these systematics uncertainties we adopt the same approach described in [30].

9.1.1   Jet Energy Scale

After applying the energy correction algorithm to jets we are left with some residual uncertainty to the Jet Energy Scale (JES). The effect on the measured X^0 cross section is evaluated by applying a $\pm 1\sigma$ shift on the JES and then running the full reconstruction on signal and background samples; the resulting change in the reconstructed, or measured, cross section as a function of the cross section itself is then interpreted as the uncertainty on the X^0 cross section.

The procedure consists in generating pseudoexperiments with "shifted" templates and acceptances and analyzing them with correct templates and

acceptances[1] . The procedure is applied for two integrated luminosity scenarios $\int \mathcal{L} = 319, 1000\,pb^{-1}$, for 17 signal cross sections $\sigma_{X_0} = 0.125, 0.25, 0.375, 0.50, 0.75\ldots 3.75\,pb^{-1}$ and five input signal masses $M_{X_0} = 450, 500\ldots 900\,GeV/c^2$. The functional dependence of the shift versus cross section is fit with a linear function $\delta\sigma_{X_0} = \alpha_0 + \alpha_1 \cdot \sigma_{X_0}$ for each mass and for both positive and negative JES shifts. Results of the fits for $\int \mathcal{L} = 1000\,pb^{-1}$ are reported in Table 9–1.
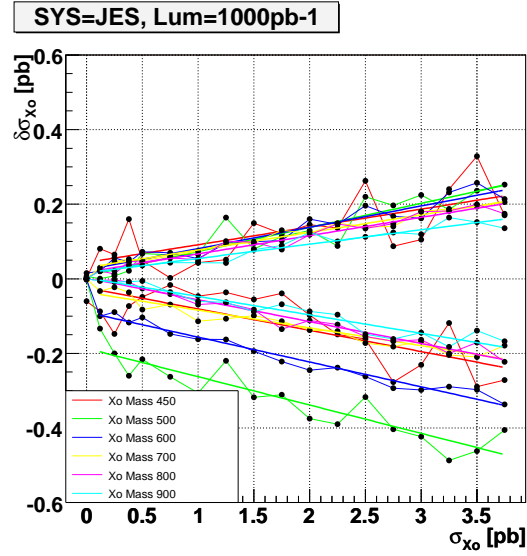
Figure 9–1: Cross section shift due to JES uncertainty for $\int \mathcal{L} = 1000\,pb^{-1}$. The shift represents the uncertainty on the cross section due to JES, as a function of cross-section

9.1.2   Initial and Final State Radiation

To investigate the systematic effect of the initial and final state radiation (ISR and FSR) uncertainties on the template shape we followed a similar method to the one described in the previous section. We applied the $M_{t\bar{t}}$ reconstruction algorithm to official CDF samples with less or more radiation, corresponding to a $+\sigma$ or $-\sigma$ change. Then we generated pseudoexperiments with shifted (new)

---

[1] This to mimic the approach to analysis of the *real* data.

Table 9–1: Linear fit parameters describing the uncertainty due to JES systematic; JES- and JES+ labels designate a $+\sigma$ or $-\sigma$ variation in energy scale. The uncertainty on cross-section is parametrized with $\delta\sigma_{X_0} = \alpha_0 + \alpha_1 \cdot \sigma_{X_0}$.

M_{X_0}	α_0^{JES-}	α_1^{JES-}	α_0^{JES+}	α_1^{JES+}
450	0.044	0.048	-0.024	-0.057
500	0.009	0.065	-0.187	-0.076
600	0.024	0.057	-0.090	-0.067
700	0.030	0.047	-0.036	-0.048
800	0.018	0.049	0.002	-0.058
900	0.016	0.038	0.002	-0.050

templates and acceptances and just like before analyzed them using the unshifted (original) templates and acceptances. The parametrizations of these uncertainties are presented in Tables 9–2 and 9–3.

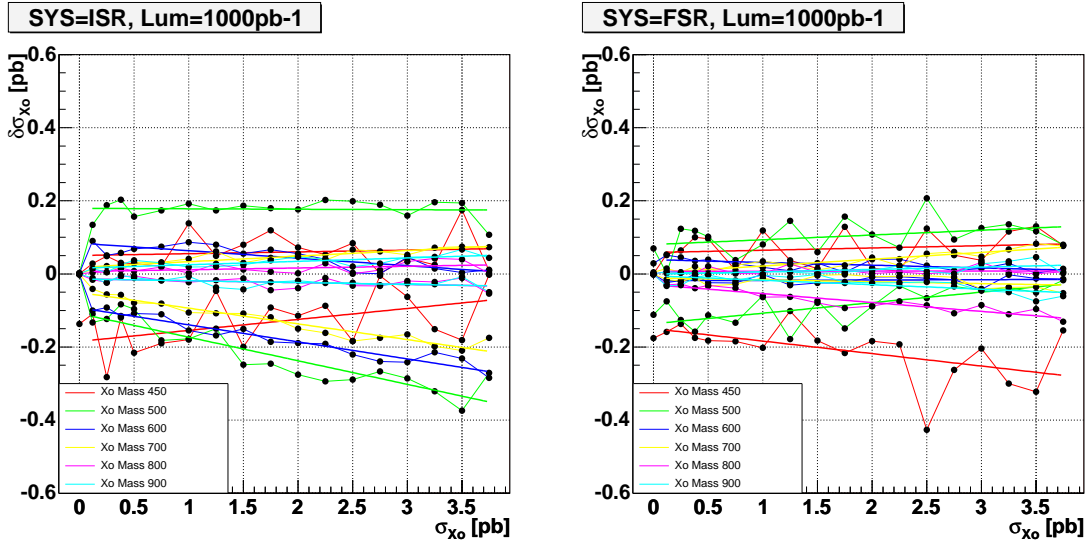
Figure 9–2: Cross section shift due to ISR (left) and FSR (right) uncertainties for $\int \mathcal{L} = 1000\, pb^{-1}$.

9.1.3   W-Q^2 Scale

To account for the uncertainty on the correct Q^2 scale for the W+jets production we calculate the shift in the reconstructed cross section for a different

Table 9–2: Linear fit parameters describing the uncertainty due to ISR modeling. The uncertainty in cross section is parametrized with $\delta\sigma_{X_0} = \alpha_0 + \alpha_1 \cdot \sigma_{X_0}$.

M_{X_0}	α_0^{ISR-}	α_1^{ISR-}	α_0^{ISR+}	α_1^{ISR+}
450	0.05	0.00	-0.18	0.03
500	0.18	-0.00	-0.11	-0.06
600	0.08	-0.02	-0.09	-0.05
700	0.02	0.02	-0.05	-0.04
800	0.01	0.00	-0.01	-0.01
900	0.02	0.01	-0.01	-0.00

Table 9–3: Linear fit parameters describing the uncertainty due to FSR modeling. The uncertainty in cross section is parametrized with $\delta\sigma_{X_0} = \alpha_0 + \alpha_1 \cdot \sigma_{X_0}$.

M_{X_0}	α_0^{FSR-}	α_1^{FSR-}	α_0^{FSR+}	α_1^{FSR+}
450	0.06	0.01	-0.15	-0.03
500	0.08	0.01	-0.14	0.03
600	0.04	-0.01	-0.02	0.00
700	0.00	0.02	-0.01	-0.01
800	0.01	0.00	-0.03	-0.02
900	-0.00	0.01	-0.01	-0.01

choice of Q^2 scale using another CDF official systematic sample. The same technique is used.

The shifts are shown in Figure 9–3 and the corresponding parametrizations of these uncertainties are presented in Table 9–4.

Table 9–4: Linear fit parameters describing the uncertainty due to W-Q^2 scale, The uncertainty in cross section is parametrized with $\delta\sigma_{X_0} = \alpha_0 + \alpha_1 \cdot \sigma_{X_0}$.

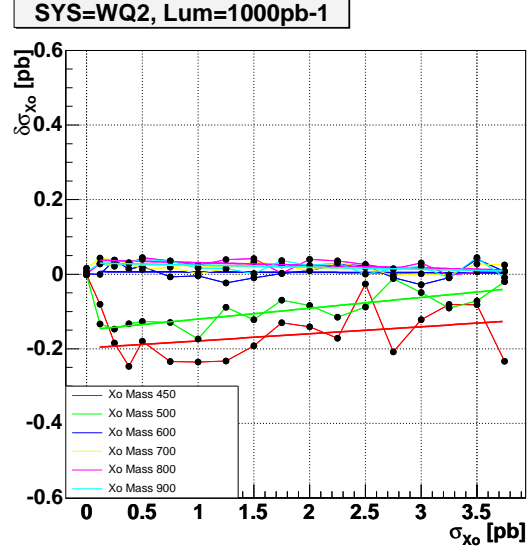| M_{X_0}	α_0^{WQ2}	α_1^{WQ2}
450	-0.20	0.02
500	-0.15	0.03
600	0.01	-0.00
700	0.03	-0.00
800	0.04	-0.01
900	0.03	-0.01

Figure 9–3: Cross section shift due to W-Q^2 scale uncertainty for $\int \mathcal{L} = 1000\, pb^{-1}$

9.1.4 Parton Distribution Functions Uncertainty

One way to estimate the effect of uncertainties in the parton distribution functions (PDF) is to reweight the events according to a new set of PDFs and investigate the effect.

In this case we changed each of the 20 PDF eigenvalues up and down by their errors and thus obtained 40 shifted templates for each unshifted template. The overall acceptance variation is of the order of 1%, which is clearly covered by the prior uncertainty on acceptance. The remaining effect if any is due to template shape changes. However, we weren't able to see any difference and a Kolmogorov-Smirnoff test applied between the central template and the shifted templates returned 1.0 in all cases, therefore we consider the PDF uncertainties to be negligible for our search.

9.1.5 Overall Shape Systematic Uncertainties

Since we consider each shape systematic uncertainty as independent and Gaussian-like, we can calculate the total shift due to all these effects by adding

in quadrature the various shifts($\delta\sigma_{X_0}$) for any given value of the assumed signal cross-section (on the x axis).

Figure 9–4 shows the total shifts for all the signal masses $M_{X_0} = 450 \ldots 900 \, GeV/c^2$ at an integrated luminosity of $\int \mathcal{L} = 1000 \, pb^{-1}$.
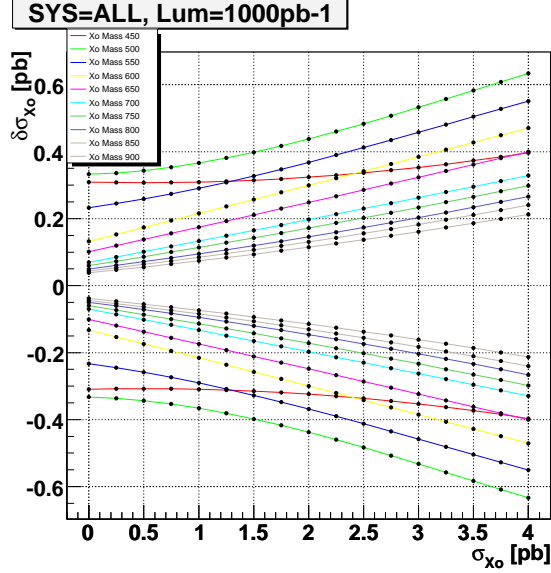

Figure 9–4: Total shape systematic uncertainty versus signal cross section.

9.2   Effect of Shape Systematics

To incorporate the shape systematics into the Bayesian machinery we considered the uncertainty on cross section $\delta\sigma_{X_0}(\sigma_{X_0})$ as a gaussian uncertainty on each point of the posterior probability density function.

More explicitly we convolute the posterior obtained in the previous chapter with this parametrization of the cross-section shifts due to shape systematics as a function of signal cross-section itself:

$$PROB_{SYS}(\sigma_{X^0}) = PROB \otimes \delta\sigma_{X^0} = \int_0^\infty G(\sigma_{X^0} - \sigma', \delta\sigma_{X^0}(\sigma')) \, PROB(\sigma') \cdot d\sigma' \quad (9\text{-}1)$$

In Eq. 9-1 $G(x_0, \ \sigma)$ stands for a *truncated* Gauss distribution of mean x_0 and standard deviation σ, because in performing the calculation we have to pay

attention to the finite lower bound (zero) in the integration, that is, the resulting convoluted function has to be zero for non-physical negative cross-sections. To obtain such a result the convoluting function has to be a normalized truncated Gaussian.

From a more intuitive point of view we can think that we apply this convolution on the posterior iteratively for each shape systematic effect, however the operation of convolution satisfies $(f \otimes g) \otimes h = f \otimes (g \otimes h)$ which means we can first combine all shape systematic effects in one function (which is done by adding in quadrature the shifts) and then convoluting that combined shift function with the posterior as obtained using the procedure described in the previous chapter.

Figure 9–5 shows the effect of smearing (convolution) on one posterior distribution function obtained from a pseudoexperiment. The most probable value moves a bit away from zero and the 95% CL on the cross section shifts to a higher value, as expected (the sensitivity should depreciate due to systematics, so we should see higher upper limits).
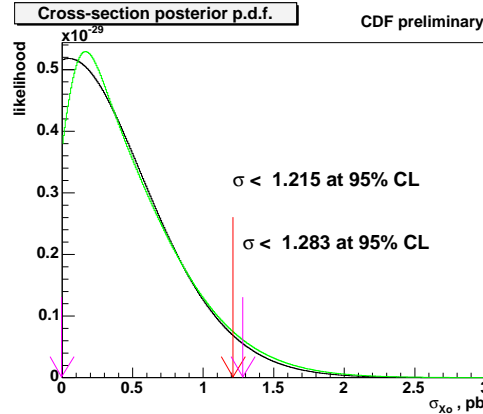

Figure 9–5: Posterior probability function for the signal cross section. The smeared (convoluted) probability in green, including shape systematics, shows a longer tail than the original (black) distribution. As a consequence the UL quoted on the plot is shifted to higher values with respect to the one calculated based on the original posterior

9.3   Expected Sensitivity with Shape Systematics

After applying the smearing procedure due to shape systematics we calculated the expected sensitivity (upper limits) for various resonance masses and two luminosity scenarios. These can be seen in Fig. 9–6 which shows the expected sensitivity for the two integrated luminosity scenarios $\int \mathcal{L} = 319,\ 1000\,pb^{-1}$.

Figure 9–7 shows the power of the algorithm, as defined in the previous chapter, after applying the shape systematics.
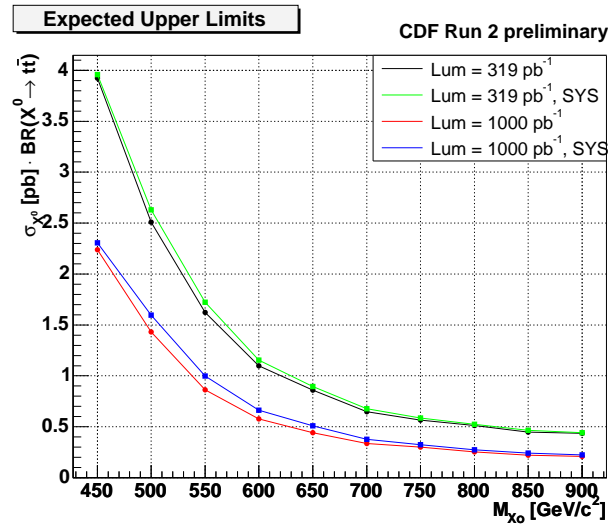

Figure 9–6: Upper limits at 95% CL. The plots show the results for two luminosity scenarios, including or excluding the contribution from shape systematic uncertainties
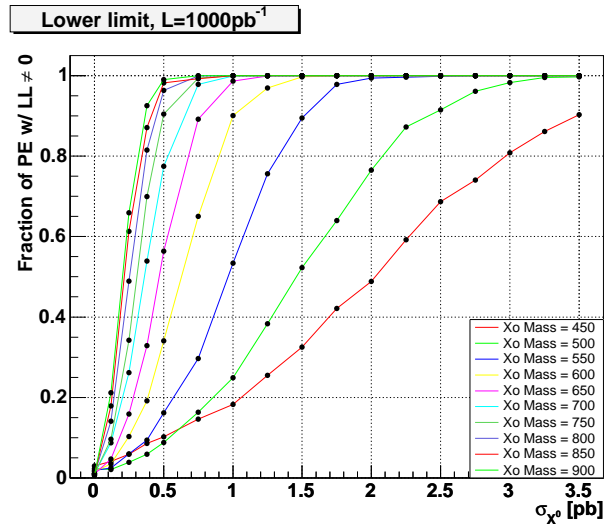
Figure 9–7: Probability of observing a non-zero lower limit (LL) versus input signal cross section for $\int \mathcal{L} = 1000 \, pb^{-1}$.

CHAPTER 10
RESULTS

Wwe first looked at the data in the summer of 2005 when CDF had available for analysis 320 pb^{-1} of data gathered since 2002. Just six months later another 360 pb^{-1} of data became available and it was added added to the analysis, providing better limits.

10.1 First Results
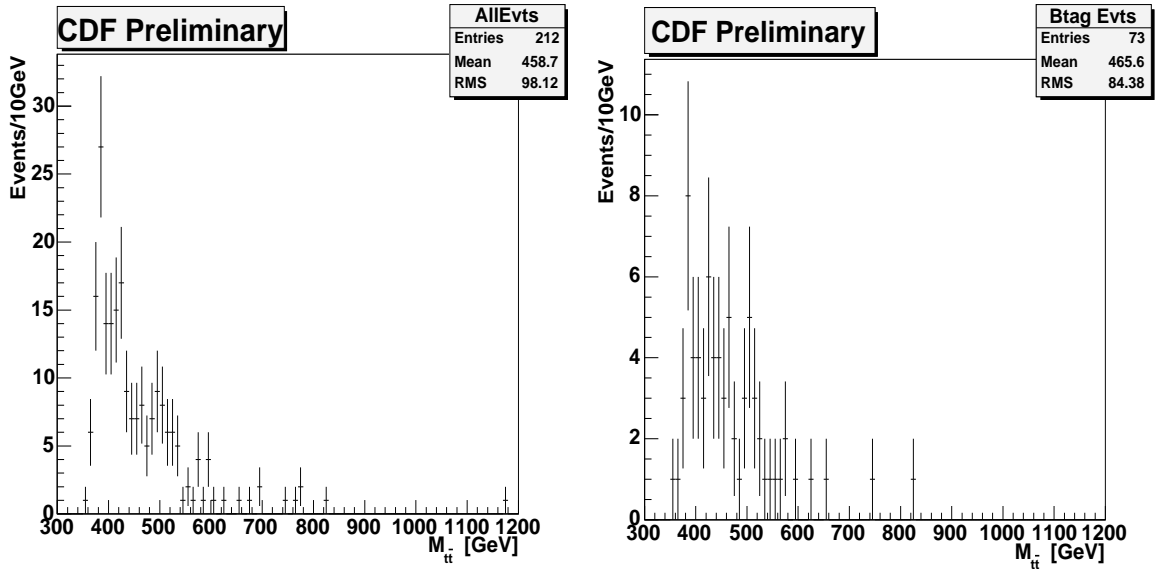
Figure 10–1: Reconstructed $M_{t\bar{t}}$ in 320 pb^{-1} of CDF Run 2 data. The plot on the right shows events with at least one SECVTX tag

In the first chunk of data we found 215 events passing our event selection. We ran the $M_{t\bar{t}}$ reconstruction algorithm and the resulting spectrum is shown in the left plot of Figure 10–1. Three events were not reconstructed, which means there were no available solutions satisfying the W and top mass constraints (the algorithm forces the two top quarks on shell, together with the W that decays leptonically).

Table 10–1: Expected number of events assuming no signal. WW and QCD numbers are derived based on the total number of events observed in the search region above $400 GeV/c^2$.

Sample	expected # of events for 320 pb^{-1}
SM $t\bar{t}$	65.9
WW	3.8
W($e\nu$)	36.9
W($e\mu$)	34.1
QCD	7.3

The right plot in Figure 10–1 shows events with at least one b-tagged jet; however we do not present results for this subsample. A more interesting plot (Figure 10–2) shows the 148 events found in the search region above the 400 GeV/c^2 cut, together with the Standard Model expectation. Even though we have
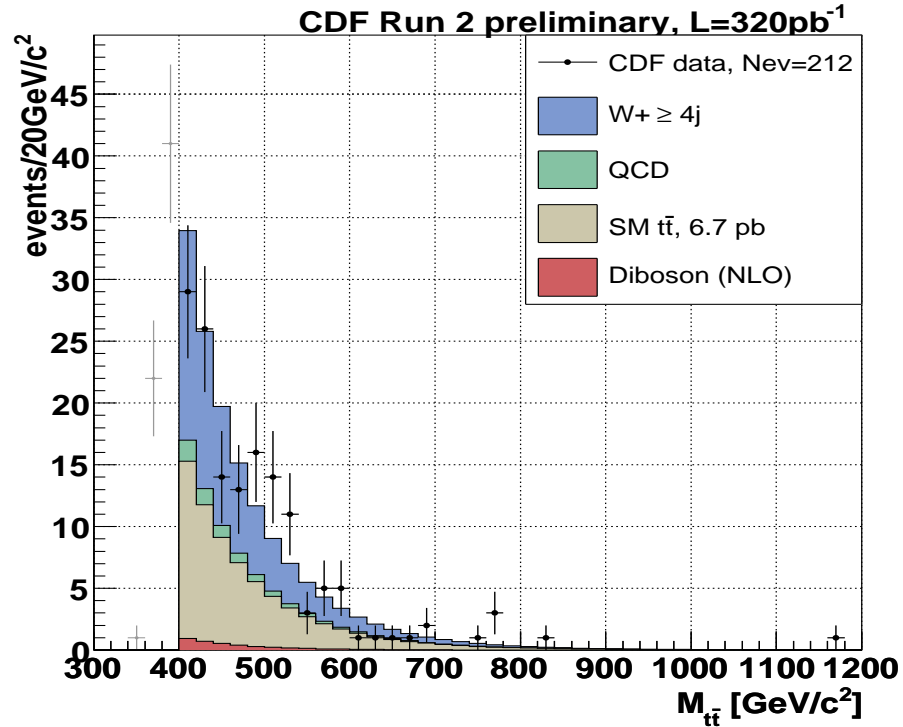

Figure 10–2: Reconstructed $M_{t\bar{t}}$ in 320 pb^{-1} of CDF Run 2 data, after the 400 GeV cut

quite a good agreement between data and the Standard Model, there seem to be few extra events in the 500 GeV/c^2 region. But before addressing that issue in

more detail we would like to present the "result" of our analysis which, together with one possible theoretical interpretation, is shown in Figure 10–3. The bands define 68% and 95% coverage intervals on the expected upper limit. In other words, due to limited statistics our derived upper limits from 1000 pseudoexperiments have non-negligible fluctuations. The central value is the median of the histogram of upper limits from the 1000 pseudoexperiments, as mentioned before, and the bands are defined by integrating half the interval on both sides - i.e. 34% of the area on each side of the median in the case of the 68% band. In the absence of any signal we expect the actual upper limits to be consistent with the expected upper limits. For a resonance mass of 500 GeV/c^2 the data doesn't fit very well, but the deviation is equivalent to a 2σ fluctuation which is not that unlikely. This is consistent with the qualitative statement we made before regarding the 500 GeV/c^2 region, based on the shape of the $M_{t\bar{t}}$ spectrum. The black line
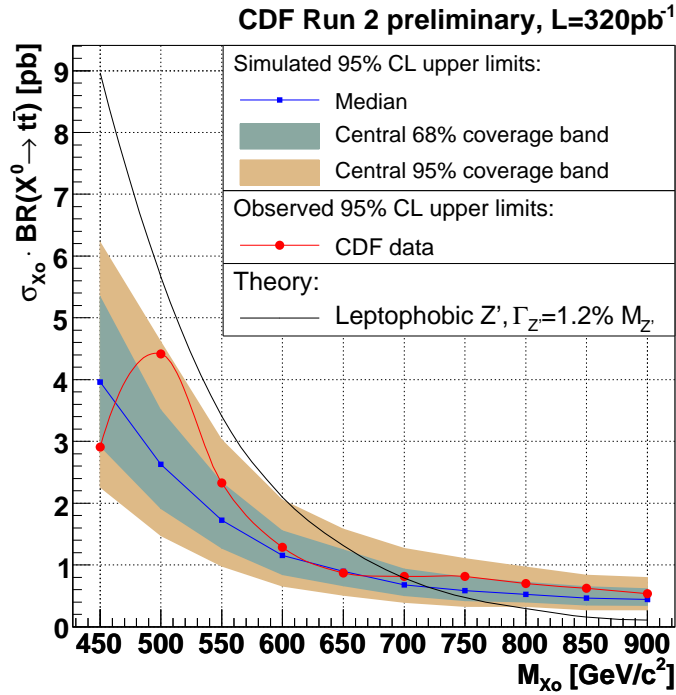

Figure 10–3: Resonant production upper limits from 320 pb^{-1} of CDF Run 2 data

on the same plot represents the predicted signal cross-section according to the

leptophobic topcolor-assisted technicolor theoretical model used in the Run 1 analysis. According to this model, we could exclude resonances with masses below 700 GeV/c^2 at 95% confidence level.

Following the hypothesis that a small resonance contribution is present in the data we performed an additional Kolmogorov-Smirnoff test on the $M_{t\bar{t}}$ distribution assuming first that there is no signal and then adding a 2 pb signal contribution coming from a 500 GeV/c^2 resonance. The particular signal cross-section was chosen based on the most likely cross-section returned by our sensitivity machinery. The results of the tests are shown in Figures 10–4 and 10–5. The data is consistent with the Standard Model-only hypothesis at the 15% level and with the Standard Model plus a 500 GeV/c^2 resonance at the 70% level. The expected $M_{t\bar{t}}$ shape with such a signal present is shown in Figure 10–6.

10.2   Final Results

After observing quite in interesting $M_{t\bar{t}}$ spectrum when the data was looked at for the first time we eagerly waited to add more data and see whether the peak around 500 GeV/c^2 remains, is enhanced or diminished.

In January 2006 we added another 360 pb^{-1} of data and produced similar plots: the $M_{t\bar{t}}$ spectrum vs the Standard Model expectation, shown in Figure 10–7, and the upper limits plot shown in Figure 10–8.

Table 10–2:   Expected number of events assuming no signal. WW and QCD numbers are derived based on the total number of events observed in the search region above the $400 GeV/c^2$.

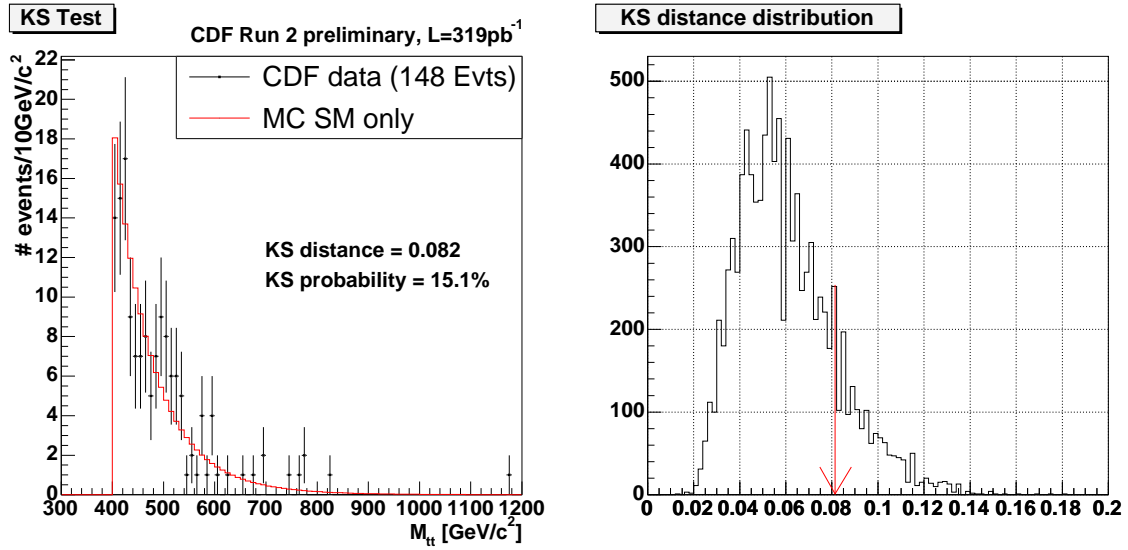| Sample	expected # of events for 680 pb^{-1}
SM $t\bar{t}$	147.7
WW	8.1
W($e\nu$)	69.0
W($e\mu$)	63.7
QCD	13.7

Figure 10–4: Kolmogorov-Smirnoff (KS) test assuming only the Standard Model. The KS distance distribution from pseudoexperiments is shown in the right plot; the arrow indicates the KS distance between data and the Standard Model template

Figure 10–5: Kolmogorov-Smirnoff (KS) test assuming signal with a mass of $500\ GeV/c^2$ and a cross-section equal to the most likely value from the posterior probability. The KS distribution from pseudoexperiments is shown in the right plot; the arrow indicates the KS distance between data and the Standard Model + signal template.
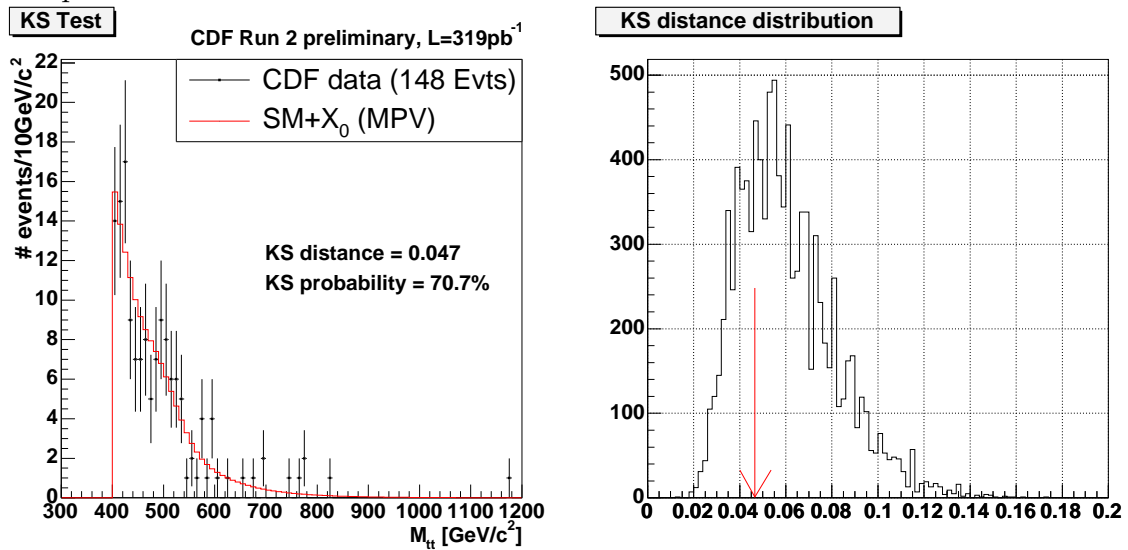
As it can be seen in these plots the agreement between the Standard Model and the data is again quite good, and the peak around $500\ GeV/c^2$ is diminished significantly. A new Kolmogorov-Smirnoff test performed between the data and
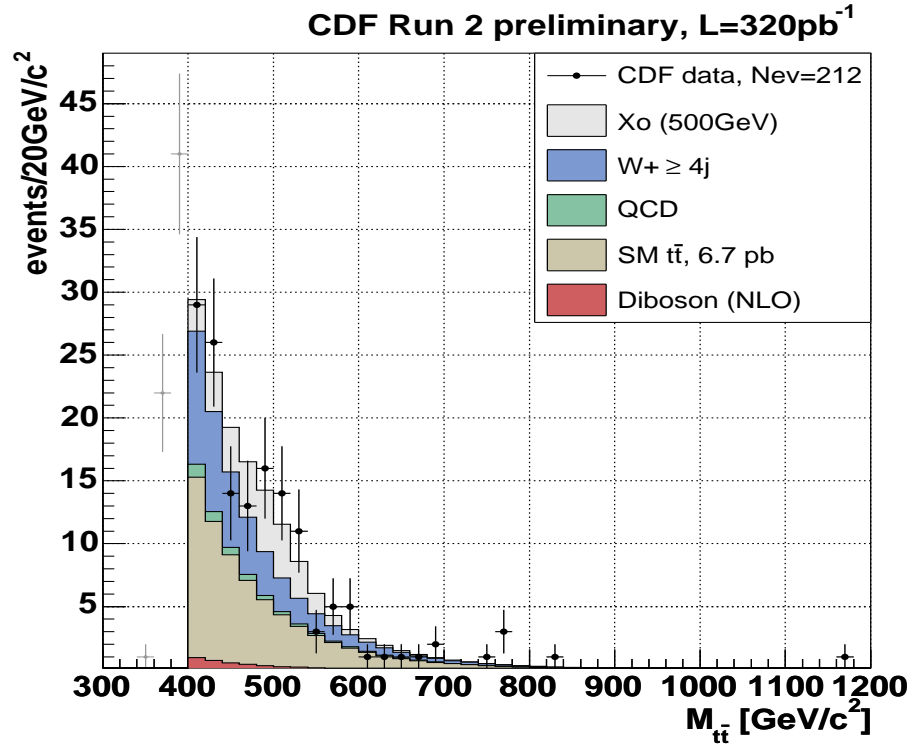
Figure 10–6: $M_{t\bar{t}}$ spectrum in data vs. Standard Model + 2 pb signal contribution from a resonance with a mass of 500 GeV/c^2

the expected Standard Model shape returned a less interesting probability of 56% (Figure 10–9).

The upper limits based on the full dataset available are listed in Table 10–3. For the same theoretical model mentioned before and according to Figure 10–8 we can exclude resonance masses below 725 GeV/c^2, thus considerably extending the Run 1 CDF and D0 limits of 480 GeV/c^2 and respectively 560 GeV/c^2.

10.3 Conclusions

We have searched for resonance production of $t\bar{t}$ pairs using a matrix element based method to reconstruct the invariant mass distribution of $t\bar{t}$ candidates.

The search was performed in a blind fashion; the data was looked at only when the reconstruction and search algorithms were established, the treatment
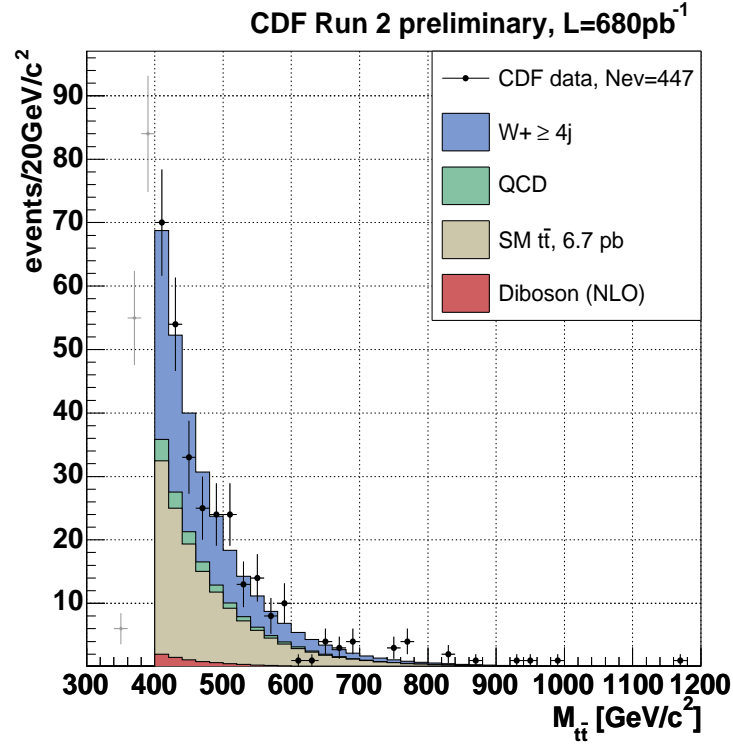
Figure 10–7: Reconstructed $M_{t\bar{t}}$ in CDF Run 2 data, 680 pb^{-1}
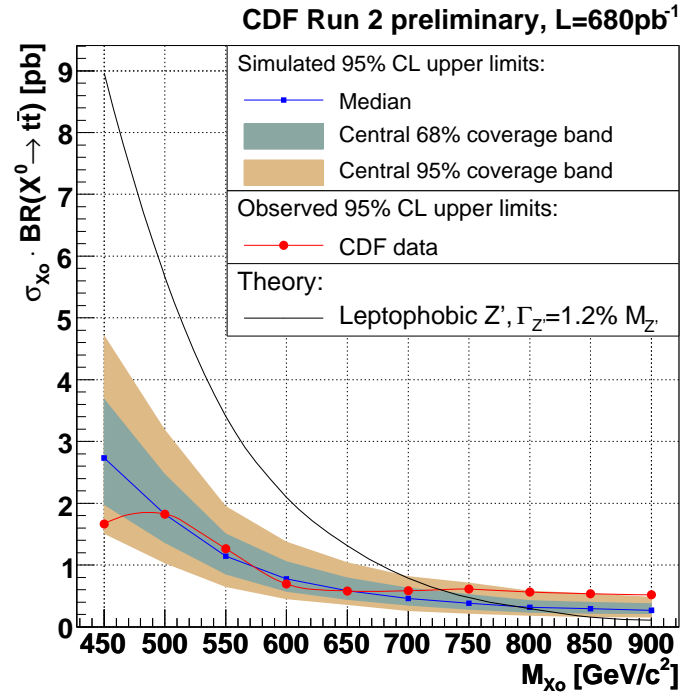
Figure 10–8: Resonant production upper limits in CDF Run 2 data, 680 pb^{-1}
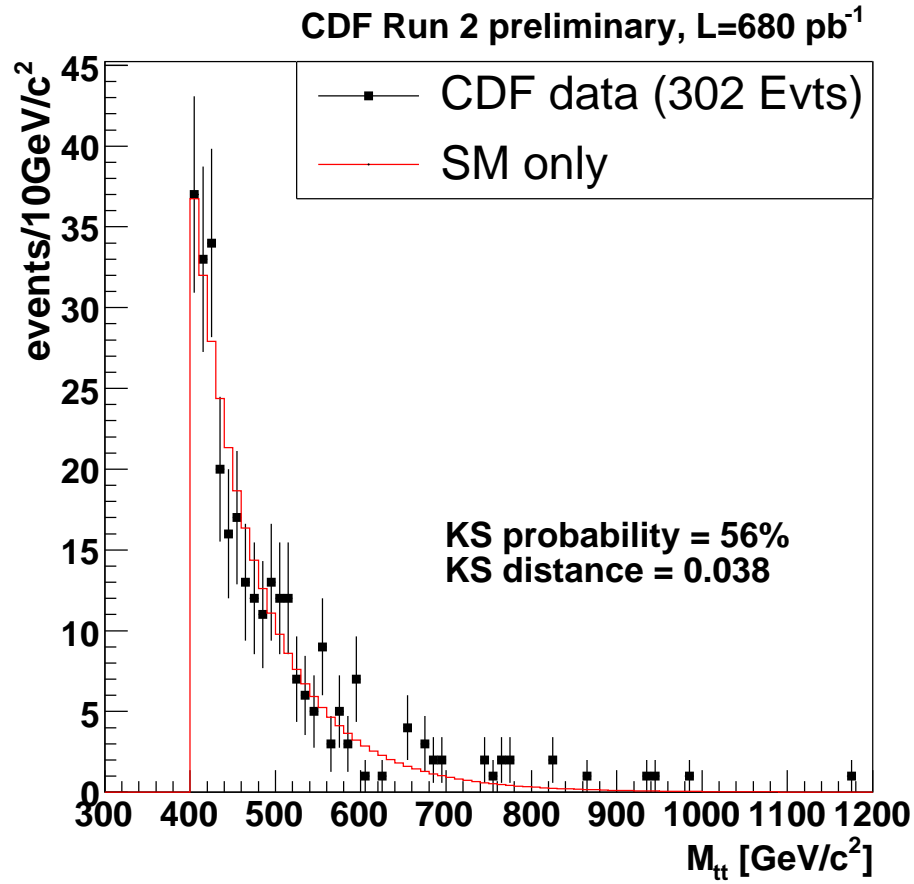
Figure 10–9: Kolmogorov-Smirnoff test results are shown together with the reconstructed $M_{t\bar{t}}$ using 680 pb^{-1} and the corresponding Standard Model expectation template

of systematics was understood and the expected limits for pure Standard Model computed.

No indication of resonant production was found, and we set new, better signal cross-section times branching ratio limits. Assuming resonance production according to a leptophobic topcolor-assisted technicolor model we exclude resonance masses below 725 GeV/c^2. This is the best current limit in such searches.

Table 10–3: Expected and observed upper limits on signal cross-section derived from a dataset with an integrated luminosity of 680 pb^{-1}.

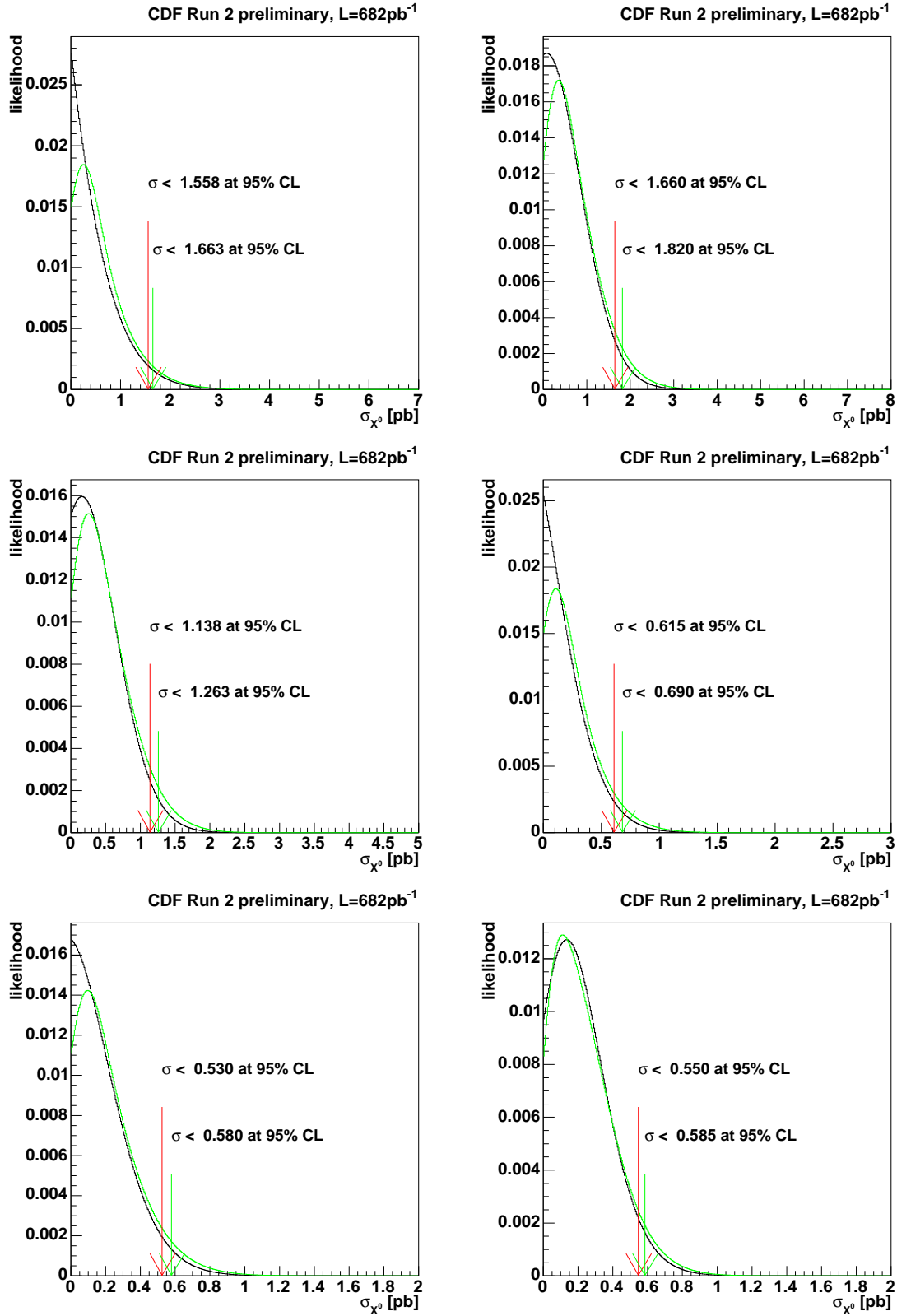| Mass (GeV/c^2)	Expected UL (pb)	Observed UL (pb)
450	2.7324	1.6652
500	1.8203	1.8236
550	1.1440	1.2640
600	0.7741	0.6913
650	0.5827	0.5801
700	0.4553	0.5851
750	0.3804	0.6099
800	0.3167	0.5602
850	0.2933	0.5357
900	0.2685	0.5171

Figure 10–10: Posterior probability distributions for CDF data and masses between 450 and 700 GeV.
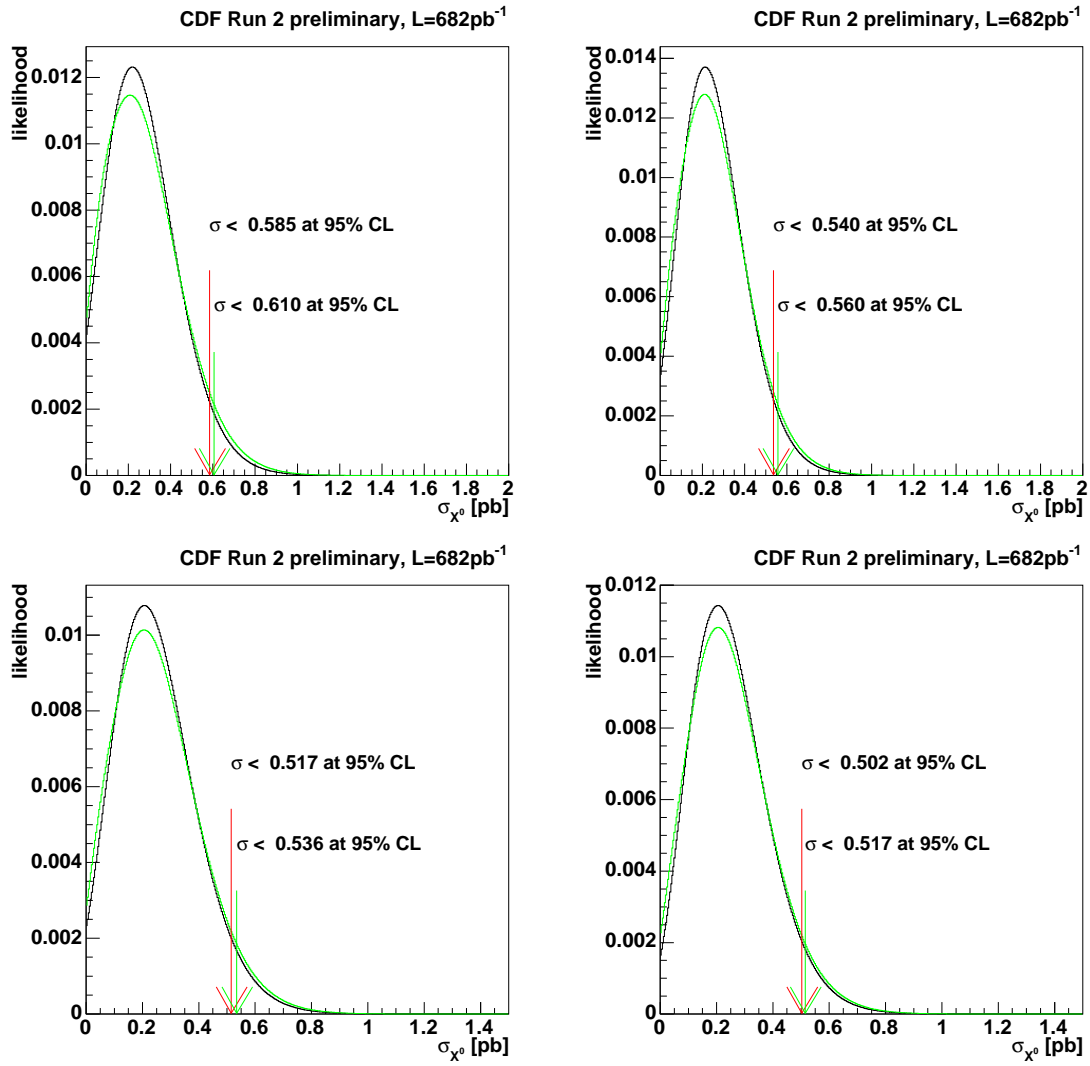
Figure 10–11:   Posterior probability distributions for CDF data and masses between 750 and 900 GeV.

APPENDIX
CHANGE OF VARIABLES AND JACOBIAN CALCULATION SKETCH

We will work in the massless limit approximation for the 6 final state particles.

Let us denote by p_1 and p_2 the momenta of the two W daughter quarks and by p_3 and p_4 the momenta of the two b quarks such that p_1, p_2 and p_3 are the decay products of one top quark. Then let p_l be the momentum of the (charged) lepton and p_ν the momentum of the neutrino. Similarly $\vec{n}_1$, $\vec{n}_2$, $\vec{n}_3$, $\vec{n}_4$, $\vec{n}_l$ are the corresponding unit vectors and we will also use p_ν^x, p_ν^y and p_ν^z for the components of the neutrino momentum.

The integration required is of the form $\int dp_1 dp_2 dp_3 dp_4 d^3 p_\nu$ but we would rather integrate over the new variables $M_{W_1}^2$, $M_{W_2}^2$, $M_{T_1}^2$, $M_{T_1}^2$ and $\vec{P}_6^T$ which are the squares of the W and top masses and the 6 body transverse momentum.

The initial set contains 7 real variables while the new set contains only 6 variables so in fact we have to keep one of the initial variables and that will be p_1.

The relation between the old and new variables is given below:

$$M_{W_1}^2 = 2p_1 p_2 (1 - \vec{n}_1 \cdot \vec{n}_2) \tag{1}$$

$$M_{W_2}^2 = 2(p_l p_\nu - \vec{p}_l \cdot \vec{p}_\nu) \tag{2}$$

$$M_{T_1}^2 = M_{W_1}^2 + 2p_3 p_1 (1 - \vec{n}_3 \cdot \vec{n}_1) + 2p_3 p_2 (1 - \vec{n}_3 \cdot \vec{n}_2) \tag{3}$$

$$M_{T_2}^2 = M_{W_2}^2 + 2p_4 p_l (1 - \vec{n}_4 \cdot \vec{n}_l) + 2p_4 (p_\nu - \vec{n}_4 \cdot \vec{p}_\nu) \tag{4}$$

$$\vec{P}_6^T = p_1\vec{n}_1^T + p_2\vec{n}_2^T + p_3\vec{n}_3^T + p_4\vec{n}_4^T + p_l\vec{n}_l^T + \vec{p}_\nu^T \tag{5}$$

We will compute the Jacobian of the transformation using the identity:

$$
\begin{aligned}
\int dp_1 dp_2 dp_3 dp_4 d^3 p_\nu &= \int \Big[\int \delta(M_{W_1}^2 - 2p_1 p_2(1 - \vec{n}_1 \cdot \vec{n}_2)) \cdot \delta(M_{W_2}^2 - 2(p_l p_\nu - \vec{p}_l \cdot \vec{p}_\nu)) \cdot \\
&\quad \delta(M_{T_1}^2 - M_{W_1}^2 - 2p_3 p_1(1 - \vec{n}_3 \cdot \vec{n}_1) - 2p_3 p_2(1 - \vec{n}_3 \cdot \vec{n}_2)) \cdot \\
&\quad \delta(M_{T_2}^2 - M_{W_2}^2 - 2p_4 p_l(1 - \vec{n}_4 \cdot \vec{n}_l) - 2p_4(p_\nu - \vec{n}_4 \cdot \vec{p}_\nu)) \cdot \\
&\quad \delta^2(\vec{P}_6^T - p_1\vec{n}_1^T - p_2\vec{n}_2^T - p_3\vec{n}_3^T - p_4\vec{n}_4^T - p_l\vec{n}_l^T - \vec{p}_\nu^T) \cdot \\
&\quad dM_{W_1}^2 dM_{W_2}^2 dM_{T_1}^2 dM_{T_2}^2 d^2 \vec{P}_6^T\Big] dp_1 dp_2 dp_3 dp_4 d^3 p_\nu
\end{aligned}
\tag{6}
$$

and switching the order of the integrals, that is integrate over the old variables first and use the property $\int \delta(f(x))dx = \sum_i \frac{1}{|f'(x_0^i)|}$ where x_0^i are all solutions for the equation $f(x) = 0$.

First we do the p_2 integral via the first delta function which yields a factor of

$$\frac{1}{2p_1(1 - \vec{n}_1 \cdot \vec{n}_2)} \tag{7}$$

and the solution

$$p_2 = \frac{M_{W_1}^2}{2p_1(1 - \vec{n}_1 \cdot \vec{n}_2)} \tag{8}$$

which is to be used in all subsequent calculations even though we won't do it explicitly here.

Next we do the p_3 integral via the third delta function which yields another factor of

$$\frac{1}{2p_1(1 - \vec{n}_3 \cdot \vec{n}_1) + 2p_2(1 - \vec{n}_3 \cdot \vec{n}_2))} \tag{9}$$

and the solution

$$p_3 = \frac{M_{T_1}^2 + M_{W_1}^2}{2p_1(1 - \vec{n}_3 \cdot \vec{n}_1) + 2p_2(1 - \vec{n}_3 \cdot \vec{n}_2))} \tag{10}$$

which again must be replaced in all subsequent calculations.

Next we do the $d\vec{p}_\nu^T$ integrals using the fifth delta function. The factor is 1 and the solution is

$$\vec{p}_\nu^T = \vec{P}_6^T - p_1\vec{n}_1^T - p_2\vec{n}_2^T - p_3\vec{n}_3^T - p_4\vec{n}_4^T - p_l\vec{n}_l^T \qquad (11)$$

which is less trivial than it looks since $\vec{p}_\nu^T$ depends on the yet to be integrated variable p_4 so it can't be treated as a constant when we will do the integration over p_4.

Now we do the p_ν^z integral using the second delta function in which $\vec{p}_\nu^T$ is replaced with the expression above. The resulting factor is

$$\frac{p_\nu}{2|p_l p_\nu^z - p_\nu p_l^z|} \qquad (12)$$

We have two solutions for the p_ν^z and these can be written in a compact form as

$$p_\nu^z = \frac{a n_l^z \pm \sqrt{a^2 - (\vec{n}_l^T)^2(\vec{p}_\nu^T)^2}}{(\vec{n}_l^T)^2} \qquad (13)$$

with

$$a = \frac{M_{W_2}^2}{2p_l} + \vec{n}_l^T \cdot \vec{p}_\nu^T \qquad (14)$$

Like for $\vec{p}_\nu^T$, p_ν^z also depends on p_4 and now we will turn to this last integral which is evaluated using the fourth delta function. But here we have to replace the explicit expressions for $\vec{p}_\nu$ as a function of p_4. We can simplify the expressions if we notice that from the leptonic W mass constraint we can express p_ν as

$$p_\nu = a + n_l^z p_\nu^z \qquad (15)$$

and the expression inside the delta function can be rewritten as

$$M_{T_2}^2 - M_{W_2}^2 - 2p_4(p_l + a - \vec{n}_4 \cdot \vec{p}_l - \vec{n}_4^T \cdot \vec{p}_\nu^T + (n_l^z - n_4^z)p_\nu^z) \qquad (16)$$

Then the derivative with respect to p_4 reads

$$-2(p_l + a - \vec{n}_4 \cdot \vec{p}_l - \vec{n}_4^T \cdot \vec{p}_\nu^T + (n_l^z - n_4^z)p_\nu^z) - 2p_4(-\vec{n}_l^T \cdot \vec{n}_4^T + (n_l^z - n_4^z)\frac{\partial p_\nu^z}{\partial p_4} + (\vec{n}_4^T)^2)(17)$$

where we used $\frac{\partial \vec{p}_\nu^T}{\partial p_4} = -\vec{n}_4^T$ which is used to evaluate $\frac{\partial a}{\partial p_4}$ as well. The last step is finding $\frac{\partial p_\nu^z}{\partial p_4}$. This follows from basic calculus since $p_\nu^z = p_\nu^z(a, \vec{p}_\nu^T)$, but the expressions become lengthy without adding anything new really so we will not list them here.

The explicit, numerical calculation of the factor requires finding the solutions for p_4 given that the expression inside the delta function cancels. This leads to a fourth order equation. Fourth order equations can be solved analytically. Once the solutions are found all the factors are known and their product is equal to the Jacobian.

In summary, we found the Jacobian for the change of variable defined above without explicitly computing it, that is without computing the determinant of the matrix of the first order derivatives of the old variables with respect to the new ones. A sum over all solutions is implied, that is for a given set of new variables, two or four sets of old variables exist, each with its own numerical value for the Jacobian.

REFERENCES

[1] J.F.Donoghue, E. Golowich, B.R. Holstein, "Dynamics of the Standard Model", Cambridge Monographs on Particle Physics, Nuclear Physics and Cosmology. CUP, 1996 (reprinted)

[2] G. Arnison *et al.* [UA1 Collaboration], *Phys. Lett.* **B122**, 103(1983).

[3] P. Bagnaia *et al.* [UA2 Collaboration], *Phys. Lett.* **B122**, 476 (1983).

[4] G. Arnison *et al.* [UA1 Collaboration],*Phys. Lett.* **B126**, 398 (1983).

[5] P. Bagnaia *et al.* [UA2 Collaboration], *Phys. Lett.* **B129**, 130 (1983).

[6] C.T. Hill, *Phys. Lett* **B345**, 483 (1995); C.T. Hill and S.J. Parke, *Phys. Rev.* **D49**, 4454 (1994)

[7] R.M. Harris, C.T. Hill, and S.J. Parke, Fermilab Report No. Fermilab-FN-687; hep-ph/9911288, 1999

[8] T. Appelquist, H.C. Cheng, and B.A. Dobrescu, *Phys. Rev.* **D64**, 035002 (2001)

[9] H.C. Cheng, K. T. Matchev, and M. Schmaltz, *Phys. Rev.* **D66**, 056006 (2002)

[10] G.Burdman, B.A. Dobrescu, E. Ponton, "Resonances from Two Universal Extra Dimensions", hep-ph/0601186

[11] T. Affolder *et al.* [CDF Collaboration], *Phys. Rev. Lett.* **85**, 2062 (2000)

[12] V.M. Abazov *et al.* [D0 Collaboration], *Phys. Rev. Lett.* **92**, 221801 (2004)

[13] F.Abe *et al.* [CDF Collaboration], *Nucl. Instrum. Methods Phys. Res.*, **271** 387 (1998)

[14] T.K. Nelson for the CDF Collaboration, "The CDF Layer 00 Detector", Fermilab preprint, FERMILAB-CONF-01-357-E (2001).

[15] F. Abe *et al.* [CDF Collaboration], *Phys. Rev.* **D45** 1448 (1992).

[16] A. Bhatti and Florencia Canelli, "Jet Energy Corrections at CDF", CDF Note 7543

[17] D. Acosta *et al.* [CDF Collab.], *Phys. Rev.* **D72**, 052003 (2005)

[18] J. Bellinger, Ken Bloom, W. David Dagenhart, Andreas Korn, Slava Krutelyov, Victoria Martin and Michael Schmitt, "A Guide to Muon Reconstruction for Run 2", CDF Note 5870

[19] R. Erbacher, Y. Ishizawa, B. Kilminster, K. Lannon, P. Lujan, T. Maki, B. Mohr, J. Nielsen, E. Palencia, S. Rappoccio *et al.*, "Event Selection and $t\bar{t}$ Signal Acceptance of the Winter 2005 Top Lepton + Jets Sample", CDF Note 7372

[20] E. Halkiadakis, C. Hays, M. Tecchio and W. Yao , "A Conversion Removal Algorithm for the 2003 Winter Conferences", CDF Note 6250.

[21] A. Taffard, "Run II Cosmic Ray Tagger", CDF Note 6100

[22] V.Barger, J. Ohnemus and R.J.N. Phillips, "Spin Correlation Effects in the Hadroproduction and Decay of Very Heavy Top Quark Pairs", Univ Wisconsin at Madison, MAD/PH/413

[23] E. Boos, V. Bunichev, M. Dubinin, L. Dudko, V. Ilyin, A. Kryukov, V. Edneral, V. Savrin, A. Semenov and A. Sherstnev, Nucl. Instrum. Meth. **A534** (2004) 250

[24] T. Sjostrand, P. Eden, C. Friberg, L. Lonnblad, G. Miu, S. Mrenna and E. Norrbin, *Computer Physics Commun.* **135** (2001) 238

[25] G. Corcella, I.G. Knowles, G. Marchesini, S. Moretti, K. Odagiri, P. Richardson, M.H. Seymour and B.R. Webber, JHEP 0101 (2001) 010

[26] M.L. Mangano, F. Piccinini, A. D. Polosa, M. Moretti and R. Pittau, JHEP **07**, 001 (2003)

[27] Luc Demortier, "A Fully Bayesian Computation of Upper Limits for Poisson Processes", CDF Note 5928

[28] Luc Demortier, "A Fully Bayesian Computation of Upper Limits for the CDF Higgs Search", Talk given at CDF Statistics Committee Meeting, July 23, 2004

[29] K. Lannon, Richard Hughes, Brian Winer, Evelyn Thomson, Robin Erbacher, Rob Roser, John Conway and Ben Kilminster "Measurement of the Cross-Section for top pair production using event kinematics", CDF Note 7753

[30] J. Conway, R. Erbacher, R. Hughes, A. Lath, R. Marginean, R. Roser, E. Thomson and B. Winer, "Search for $t' \rightarrow Wq$ Using Lepton Plus Jets Events", CDF Note 6888